THE EFFECTS OF RESIDUAL GASES ON THE FIELD EMISSION PROPERTIES OF ZnO, GaN, ZnS NANOSTRUCTURES, AND THE EFFECTS OF LIGHT ON THE RESISTIVITY OF GRAPHENE

Yudong Mo, M.S.

Dissertation Prepared for the Degree of

DOCTOR OF PHILOSOPHY

UNIVERSITY OF NORTH TEXAS

May 2014

APPROVED:

Jose Perez, Major Professor
Duncan Weathers, Committee Member
Yuri Rostovtsev, Committee Member
Chris Littler, Committee Member and Chair of the Department of Physics
Mark Wardell, Dean of the Toulouse Graduate School

Mo, Yudong. The Effects of Residual Gases on the Field Emission Properties of ZnO, GaN, ZnS Nanostructures, and the Effects of Light on the Resistivity of Graphene. Doctor of Philosophy (Physics), May 2014, 117 pp., 3 tables, 57 figures, chapter references.

In this dissertation, I present that at a vacuum of 3×10^{-7} Torr, residual O_2, CO_2, H_2 and Ar exposure do not significantly degrade the field emission (FE) properties of ZnO nanorods, but N_2 exposure significantly does. I propose that this could be due to the dissociation of N_2 into atomic nitrogen species and the reaction of such species with ZnO. I also present the effects of O_2, CO_2, H_2O, N_2, H_2, and Ar residual gas exposure on the FE properties of GaN and ZnS nanostructure. A brief review of growth of ZnO, GaN and ZnS is provided. In addition, Cs deposition on GaN nanostructures at ultra-high vacuum results in 30% decrease in turn-on voltage and 60% in work function. The improvement in FE properties could be due to a Cs-induced space-charge layer at the surface that reduces the barrier for FE and lowers the work function.

I describe a new phenomenon, in which the resistivity of CVD-grown graphene increases to a higher saturated value under light exposure, and depends on the wavelength of the light—the shorter the wavelength, the higher the resistivity. First-principle calculations and theoretical analysis based on density functional theory show that (1) a water molecule close to a graphene defect is easier to be split than that of the case of no defect existing and (2) there are a series of meta-stable partially disassociated states for an interfacial water molecule. Calculated disassociation energies are from 2.5 eV to 4.6 eV, that match the experimental observation range of light wavelength from visible to 254 nm UV light under which the resistivity of CVD-grown graphene is increased.

ACKNOWLEDGMENTS

First I would like to thank my major professor Dr. Jose Perez. Without his guidance, this work would not have been possible. I must acknowledge our group member: Jason Jones, Phillip Ecton and Rakesh Shah, who have always been helpful, sharing their ideas and lending a hand. I would also like to thank Dr. Arup Neogi, Dr. Jianyou Li and Ms. Jie Lin for help on ZnO nanorod research. Thanks to Dr. Quark Chen and Dr. Hye-won Seo for providing MBE GaN samples and sharing their experience. Thanks to Jeffrey Schwartz and Morgan Lynch for their effective work on ZnO, ZnS and GaN field emission studies; Thanks to Dr. Thomas Scharf and Dr. Nigel Shepherd for usage of their labs; Thanks to Dr. Dave Diercks and Nancy Bounce for the aid of CART equipments; Thanks to Dr. Mohamed El Bouanani for his help; and thanks to Dr. Joshua Wahrmund, Dr. Tong Cai, Dr. Chenglin Chi, Dr. Jun Zhou for their help and useful discussions.

Special thanks to Dr. Zhou Ye, Dr.Guanglin Zhao, Dr. Shzhong Yang and Mr. Zhao Lei; without their hard work and support, the studies of graphene in this dissertation would not have been interesting and gone so far. I would like to thank my other committee members Dr. Chris Littler, Dr. Duncan Weathers, Dr. Yuri Rostovtsev and former committee member Dr. Donald Kobe for serving and encouragements. I thank Dr. David Schultz for his encouragement, and the Department of Physics for its support.

Finally, special recognition and thanks go out to my family: to my wife Yunyan for her hard work of taking care of our kids, for her support, encouragement, tolerance and patience; to my son George for his support and help on my dissertation draft; to my daughter Angela for her lovely smile; to my brothers for taking care of my mother and letting me accomplish this long journey.

TABLE OF CONTENTS

LIST OF TABLES

Key: ***** Reproduced with kind permission of American Scientific Publishers.

LIST OF ILLUSTRATIONS

Key: ***** Reproduced with kind permission of American Scientific Publishers

† Reproduced with kind permission of Springer Science and Business Media

CHAPTER 1

INTRODUCTION

This dissertation addresses three topics: effects of residual gas exposure on the field emission (FE) properties of ZnO nanorods, ZnS nanostructures and GaN nanostructures; effects of cesium deposition on the field emission properties of GaN nanorods; and tuning graphene resistivity by exposure to light.

Chapter 2 introduces the main experimental instruments in our lab for the above studies, as well as gives an introduction of preparation of samples. Chapter 3 reviews the growth of ZnO, ZnS and GaN nanostructures and presents the results and discussion of the effects of residual gas exposure on the field emission (FE) properties of ZnO nanorods, ZnS nanostructures, and GaN nanostructures; and the effects of cesium deposition on the field emission properties of GaN nanorods. Chapter 4 investigates a phenomenon in which resistance of graphene grown by Chemical Vapor Deposition (CVD) changes by exposure to light. A model and computational simulation results are presented to match and explain the observations of this phenomenon. The CVD growth of graphene and fabrication of devices made of CVD-grown graphene and exfoliated graphene for I-V (current-voltage) measurement are also presented.

1.1 ZnO and GaN Nanorods as an Electron Source Compared to Molybdenum Microtips and Carbon Nanotubes

Electron sources are one of the most important building blocks of many vacuum electronic devices and are in high demand for modern technologies [1-3]. Displays used almost everywhere in everyday life are the largest application of electron sources [4-5]. There are two types of electron sources: hot electron sources and cold electron sources.

Hot electrons sources are based on thermionic emission in which the emitters are heated to a high temperature (about 2000°C), and as a result, electrons obtain enough energy from heating to go over the surface potential barrier and escape from the emitter surface to form electron emission [6]. Examples of hot electron sources are cathode ray tubes (CRT) and electron vacuum tubes; Cold electron sources are based on field emission in which an external electrical field is applied to reduce and thin the emitter's surface barrier so that electrons can tunnel out from the surface and form electron emissions at room temperature [7-8]. Due to the high temperature, the hot emitters usually have problems of oxidation by residual gas, heat dissipation, heating damage to surrounding devices, high energy consumption, shorter life time, etc.; cold emitters, by contrast, naturally eliminate these problems of thermionic emitters caused by heating to high temperature and have much less energy consumption and longer life time.

For the needs of electron sources and the advantages of field emission, looking for and making good field emitters have attracted for decades many researchers working on this area. A good field emission emitter should have low operation electrical voltage, high emission current, long life time, and controllable, stable performance. Generally, low operation voltage requires low work function of the emitter material, high emission current requires large amounts of unbounded (non-localized) electrons available, and long lifetime and stable performance require chemical and mechanical stability in the vacuum environment of use.

For the low operation voltage (applied external voltage for field emission), in addition to low work function, the high-aspect ratio of the emitter structure amplifies the local electrical field by factor of the aspect ratio. This means emitters with the structure of a high-aspect ratio can significantly lower the operating voltage. For this reason micro-

and nano-structure materials generate great interest for applications in field emission electron sources.

Metals, like molybdenum and tungsten micro tips of Spintd-type arrays, have been deeply studied and a huge amount of money has been invested for the commercial application of field emission of display (FED) [4, 5, 9, 10]. Due to their low work function, high mechanical stability, high aspect ratio and high conductivity, carbon nanotubes have also drawn tremendous study in field emission applications for the decades since they were discovered. Applications with materials mentioned above have reached many achievements, e.g., scanning tunneling microscopy, field emission microscopy, etc. However, for commercial application, the working environments are relatively tougher than in the examples mentioned here. It has been well studied that, in the vacuum range of 10^{-7} to 10^{-6} Torr, O_2 in residual gas oxidizes the metals and carbon nanotubes and significantly degrades their field emission properties [11-17].

ZnO, ZnS, and GaN nanostructures have drawn a great interest in field emission study due to their intrinsic properties: they are wide bandgap semiconductors with high melting temperatures and very excellent chemical and mechanical stabilities [18-22]; band bending of wide bandgap semiconductors under external applied electrical fields causes more electrons to go to the bottom of conduction band by lowering the surface barrier. This allows more electrons to be available for emission. Moreover, they can also exhibit negative electron affinity [23]. This means that it is easier for electrons to escape from the surface of the material and that low operation voltage can be sustained.

ZnO, ZnS and GaN have large varieties of nanostructures [24-26] and offer researchers great opportunities to increase their field emission properties by changing their structures through various methods of synthesis and growth. Most studies focus on

improving field emission properties of ZnO,ZnS and GaN nanostructures, i.e., lower turn-on voltage and increased emission current density, by growing their nanostructures with different methods, different growth parameters, or different substrates to obtain various shapes and densities with high aspect ratio. In this dissertation, our studies are focused on the effects of residual gas on the field emission properties of ZnO nanorods and how cesium deposition changes the field emission of GaN nanorods.

1.2 Effects of Residual Gas Exposure on the Field Emission Properties of ZnO Nanorods

ZnO nanostructures have great potential for application as field emission emitters due to their intrinsic properties: crystal structure of hexagonal wurtzite, wide bandgap (3.3 eV), low electron affinity (0.3-3.3 eV, even negative electron affinity), high melting temperature, and high chemical and mechanical stability. ZnO-coated field emission guns have been used in scanning electronic microscope (SEM), due to the excellent field emission properties of ZnO. In addition to the excellent field emission properties, low cost, long life time and compatibility with operating environment have to be considered for large scale commercial applications of everyday life, like FEDs. In a real FED's operating environment, even though vacuum is on the order of 10^{-7} Torr, the residual gas is unavoidable. The degradation of metal and carbon nanotubes is thought to be due to oxidation under high-electric-field conditions present during FE [11-17]. It is thought that ZnO and other oxide-based nanorods may not be as susceptible to degradation by O2 and oxygen-containing gases since they are oxides [27]. To our knowledge, a detailed study of the effects of residual gases in operating environments of 10^{-7} to 10^{-6} Torr on the field emission of ZnO nanorods is lacking [28,29]. N-type ZnO nanorods 100-200 nm in width and 300-600 nm in length were synthesized using the DC arc discharge method

with a Zn target, air pressure of 600 Torr and arc current of 30 A. See sample preparation in section 2.4. Compared to the samples of ZnO nanorods grown by chemical vapor deposition (CVD), this method has low cost. Under the working conditions (high electrical field) and the vacuum environment, the residual gases react with emitter material for a certain period of time; a significant change of field emission may be induced. In the real environment of FEDs, in addition to residual gases left by evacuation to a vacuum of 10^{-7} to 10^{-6} Torr, degassing under working conditions from surrounding devices, components and surfaces like phosphors, getter materials and from decomposition associated with high electrical field contribute to residual gases. Our studies of ZnO nanorods in our laboratory conditions are performed in a gas environment similar to that in a real field emission device. We evacuated vacuum to 10^{-9} Torr as base vacuum. With a precise leak valve, we allow gases to flow at the pressure of 3×10^{-7} Torr with only one gas at a time in the sequence of CO_2, H_2, Ar, O_2 and N_2 while measuring the field emission properties to study how each gas reacts with ZnO nanorods and changes their field emission properties. We compare the effects of O_2, CO_2, N_2, H_2, and Ar exposures on the FE properties of ZnO nanorods. In contrast to carbon nanotubes and metal microtips, we find that the FE properties of ZnO nanorods are not significantly degraded by O_2 and CO_2 exposures. However, the FE properties of ZnO nanorods are significantly degraded by N_2 exposure. We propose that this is due to the higher reactivity of nitrogen with ZnO. H_2 and Ar exposures are not observed to significantly degrade the FE properties.

1.3 Effects of Residual Gas Exposure on the Field Emission Properties of ZnS Nanostructures

Like ZnO and GaN, ZnS is a wide band gap semiconductor with good thermal stability that has attracted considerable interest for its luminescent and electrical properties with applications in light emitting diodes, flat panel displays, transparent conductive coatings, and buffer layers in solar cells [30-35]. Growth of ZnS is reviewed and the effects of residual gas exposure on the field emission properties of ZnS nanostructure grown by the solution method have been investigated.

1.4 Effects of Residual Gas Exposure on the Field Emission Properties of GaN Nanorods

With similar properties to ZnO, GaN has a hexagonal wurtzite crystal structure, wide bandgap (3.4 eV), low electron affinity (0.3-3.3 eV, even negative electron affinity), high melting temperature, and high chemical and mechanical stability. Thus, it has also attracted great interest as a promising candidate of field emission material. Moreover, compared to ZnO nanorods, GaN nanorods naturally have more varieties of nanostructures, which provide more possibilities for researchers to make a wide range of FE devices [30, 36, 37]. GaN has also been deeply and largely investigated, and its carrier type and concentration are much easier to control than those of ZnO. In FE studies of GaN nanorods, many studies are also focusing on controlling the size, density and aspect ratio of nanorods, or doping to improve FE properties of GaN nanorods. These studies are measuring FE properties and their potential applications in a vacuum environment. Because of its promise as a FE candidate for FEDs and other vacuum microelectronic devices, a study on the effects of residual gas exposure on the FE properties of GaN is needed. Similarly to our study of ZnO and with the same experimental set up, we

evacuated to a vacuum of 10^{-9} Torr as base vacuum. With a precise leak valve, we flowed gases at pressure of 3×10^{-7} Torr and one gas at a time in the a sequence of CO_2, H_2, Ar, O_2 and N_2 while measuring the field emission properties to study how each gas reacts with GaN nanorods and changes its field emission properties.

1.5 Effects of Cesium Deposition on the Field Emission of GaN nanorods

In addition to increasing nanostructure material's aspect ratio and adjusting proper density of nanostructures, one way to improve FE properties and lower the operating voltage is to modify the surface work function of the material by coating it with a low work function material [38-40]. Cesium is a metal of the lowest work function (1.9 eV). It is often used to lower work function and increase conductivity of metals and semiconductors such as Mo micro tips and carbon nanotubes, so that the operating voltage of FE can be reduced and the current can be increased. GaN nanorods grown by molecular beam epitaxy were used for studying the effects of cesium deposition on the FE properties of GaN in a vacuum of 10^{-10} Torr. A layer of cesium atoms deposited on the GaN nanorods combines with O_2 adsorbed on the GaN nanorods to form a space-charge layer on the very surface. The space-charge layer produces an electrical field inward to the GaN nanorods. This electrical field helps pull electrons from inside of GaN to the surface layer of cesium. Once the electrons reach cesium with the lowest work function, electrons can escape easily from the GaN and form FE. The turn-on voltage of FE of GaN nanorods has been reduced by 30%.

1.6 Tuning Graphene Conductivity by Exposure to Light

Graphene, a truly two dimensional material with a honeycomb planar structure of a single layer of sp2-bonded carbon atoms, has caused an explosion of interest all over the world since its first isolation in 2004 by Andre Geim and Konstantin Novoselov, who were awarded the Nobel Prize in Physics in 2010 [41-42]. Monolayer graphene has many miraculous properties such as the lightest weight, strongest mechanical strength, high thermal conductivity [43], and imperviousness to gas; and potential applications such as flexible transparent electronics and super powerful capacitors. Many of graphene's electrical properties are unique, for example, electrons can move 100 times faster in graphene than they can in silicon [41], The above unique properties ensure graphene a promising candidate to replace silicon for the next generation of faster and smaller electronic devices. Many novel applications are also as-yet-to-be explored. However, to be a semiconductor material, a proper bandgap, a controllable p-type and n-type carrier concentration and high quality with large area of uniform graphene are required. Graphene is intrinsically a semi-metal or zero-bandgap semiconductor and modification of its properties is usually required. Since graphene is a monolayer material, all atoms of graphene are surface atoms; therefore, its electrical properties are strongly affected by the ambient environment, such as the substrate and atmosphere of operating environment. Much research on changing the electrical properties of graphene address creation of a bandgap in graphene by modifying it with exposure to different gases under various conditions [44-51]. In this study, we report new observations in which the resistance of a CVD-grown graphene film, which is grown on copper foil and then transferred from etching solution and deionized (DI) water to a SiO_2 surface, can be tuned and controlled by exposure to light from the visible to ultraviolet (UV). Furthermore, we

performed first-principles calculations based on the density functional theory (DFT) method with a plane wave basis set to illustrate the process. Our simulation and analysis show that there is a series of possible sub-stable ionization states (ranging from 2.6 eV to 4.85 eV) of a water molecule in- between a graphene plane and a silicon dioxide surface. Input energy, such as light, can drive a sandwiched-like water molecule to different ionization states depending on the wavelength of incident light. The ionized hydrogen atom of a water molecule attaches to the graphene and functions as a scattering center, which results in the increase of resistance of the sample. This work provides a new and convenient method to tune the electronic properties of graphene, and a potential application of using CVD-grown graphene as a UV-sensor.

1.7 References

1. Yamamoto, S.: Fundamental physics of vacuum electron sources. Rep. Prog. Phys. 69 181-232 (2006)
2. Masood, K., Iqbal, M., Zakaullah, M.: Emission characteristics of the thermionic electron beam sources developed at EBSDL. Nuclear Instruments and Methods in Physics Research A 584 9–24 (2008)
3. Bogner, A., Jouneau, P.-H., Thollet, G., Basset, D., Gauthier, C.: A history of scanning electron microscopy developments:Towards “wet-STEM” imaging. Micron 38 390–401 (2007)
4. Talin, A.A, Dean, K.A., Jaskie, J.E.: Field emission displays: a critical review. Solid – State Electronics, Volume 45, Issue 6, p963-976, (2001)
5. Hart, J. A.: The History of Field Emission Displays. (1999) http://www.indiana.edu/~hightech/fpd/papers/FEDs.html

6. Nottingham,W. B.: Thermionic emission. Massachusetts Institute of Technology, Research Laboratory of Electronics, Technical Report 321, Handbuch der Physik, Volume XXI, December 10, (1956)

7. Marrese, C. M..: A review of field emission cathode technologies for electric propulsion systems and instruments. Aerospace conference proceedings, Vol.4, 85-98, IEEE, (2000)
8. Fursey, G.N.: Field emission in vacuum micro-electronics. Applied Surface Science 215 113–134 (2003)
9. Park, Y. J., Choi, J. H., Lee, H. W., Lee, N. S., Kim, J. W., Hong, S. S., Park, N. S., Jung, J. E., and Kim, J. M.: Fabrication of Spindt-type tungsten microtip field emitter arrays with optimized aluminum parting layers. J. Vac. Sci. Technol. B 18, 989 (2000)
10. Christophe Py and Robert Baptist.: Low-energy electron interference with Spindt-type microtips. J. Vac. Sci. Technol. B 13, 410 (1995)
11. Kim, S., Cho, E., Han, S., Cho, Y., Hee, S. Cho, Kim, C., and Ihm, J.: Microscopic origin of current degradation of fully-sealed carbon-nanotube field emission display. Solid State Commun. 149, 670 (2009)
12. Ribaya, B. P., Leung, J., Brown, P., Rahman, M., and Nguyen, C. V.: A study on the mechanical and electrical reliability of individual carbon nanotube field emission. Nanotechnology 19,185201 (2008)
13. Calderon-Colon, X., Geng, H., Gao, B., An, L., Cao, G., and Zhou, O.: A carbon nanotube field emission cathode with high current density and long term stability. Nanotechnology 20, 325707 (2009)

14. Wadhawan, A., Stallcup, R. E., Stephens, K. F., Perez, J. M., and Akwani, I. A.: Effects of O_2 , Ar, and H_2 gases on the field-emission properties of single-walled and multiwalled carbon nanotubes. Appl. Phys. Lett. 79, 1867 (2001)

15. Sheng. L. M., Liu. P., Liu, Y. M., Qian, L., Huang, Y. S., Liu, L., Fan, S.S.: Effects of carbon-containing gases on the field-emission current of multiwalled carbon-nanotube arrays. J. Vac. Sci. Technol. A 21, 1202 (2003)
16. Chalamala, B. R., Wallace, R. M., Gnade, B. E.: Surface conditioning of active molybdenum field emission cathode arrays. J. Vac. Sci.Technol. B. 16 2855 (1998)
17. Bonard, J-M, Klinke, C.. Degradation and failure of carbon nanotube field emitters. PHYSICAL REVIEW B 67, 115406 (2003)
18. Hahn, Y-B.: Zinc oxide nanostructures and their applications. J. Chem. Eng., 28(9), 1797-1813 (2011)
19. Wang, Z.L.: Zinc oxide nanostructures- growth, properties and applications. J. Phys. Condens. Matter 16 (2004) R829–R858
20. Ahmad, M., Zhu, J..: ZnO based advanced functional nanostructures-synthesis, properties and applications. The Royal Society of Chemistry 2010
21. Özgür, Ü.: ZnO Devices and Applications- A review of current status and future prospects. Proceedings of the IEEE | Vol. 98, No. 7, July 2010
22. Klingshirn, C..: ZnO: From basics towards applications. Phys. stat. sol. (b) 244, No. 9, 3027– 3073 (2007)
23. Wang, R. Z., Wang, B., Wang, H., Zhou, H., Huang, A. P., Zhu, M. K., Yan, H. and Yan, X.H.: Band bending mechanism for field emission in wide-band gap semiconductors. Appl. Phys. Lett., Vol. 81, No. 15 (2002)

24. Ü. Özgür, Ya. I. Alivov, C. Liu, A. Teke, M. A. Reshchikov, S. Doğan, V. Avrutin,S.-J. Cho, H. Morkoç.: A comprehensive review of ZnO materials and devices. JOURNAL OF APPLIED PHYSICS 98, 041301 (2005)
25. Li, J., Liu, J., Wang, L.-S., Robert, P., Chang, H..: Physical and Electrical Properties of Chemical vapor grown GaN nano/microstructures. Inorg.Chem.,47, 10325-10329 (2008)
26. Fang, X., Wu, L., Hu, L..: ZnS Nanostructure Arrays-A Developing Material Star. Advanced Materials, Volume 23,Issue 5, 585-598, (2011)
27. Yi, G. C., Wang, C., Park, W. I.: ZnO nanorods: synthesis, characterization and applications. Semicond. Sci. Technol. 20, 22 (2005)
28. Yeong, K. S., Maung, K. H., Thong, J. T. L..: The effects of gas exposure and UV illumination on field emission from individual ZnO nanowires Nanotechnology,18,185608 (2007)
29. Kim, D.-H., Jang, H.-S., Lee, S.-Y., and Lee, H.-R.: Effects of gas exposure on the field-emission properties of ZnO nanorods. Nanotechnology,15,1433 (2004)
30. Fang, X., Bando, Y., Gautam, U.K., C. Golberg, Ye, D.: Inorganic semiconductor nanostructures and their field-emission applications. J. Mater. Chem., 2008, 18, 509–522
31. Yamaga, S., Yoshikawa, A., Kasa, H..: Electrical and optical properties of donor doped ZnS films grown by low-pressure MOCVD.J. Cryst. Growth 86, 252-256 (1988).
32. Ye, C., Fang, X., Li, G., Zhang.L.: Origin of the green photoluminescence from zinc sulfide nanobelts. Appl. Phys. Lett. 85, 3035-3037 (2004).

33. Vacassy, R., Scholz, S.M., Dutta, J., Plummer, C.J.G..: Synthesis of Controlled Spherical Zinc Sulfide Particles by Precipitation from Homogeneous Solutions. J. Am. Ceram. Soc. 81, 2699-2705 (1998).
34. Liu, X., Caia, X., Maob, J., Jinc, C. .: ZnS/Ag/ZnS nano-multilayer films for transparent electrodes in flat display application. Appl. Surf. Sci. 183, 103-110 (2001).
35. Shao, L.X., Chang, K.H., Hwang, H.L.: Zinc sulfide thin films deposited by RF reactive sputtering for photovoltaic applications. Appl. Surf. Sci. 212–213, 305-310 (2003).
36. Ha, B., Seo, S.H., Cho, J.H., Yoon, C.S., Yoo, G-C.Y., Park, C.Y., Lee, C.J.: optical and field emission properties of thin single-crystalline GaN nanowires. J. Phys. Chem. B 109, 11095-11099 (2005)
37. Yilmazoglu, O., Pavlidis, D., Litvin, Yu.M., Hubbard, S., Tiginyanu, I.M., Mutamba K., Hartnagel, H.L., Litovchenko, V.G., . Evtukh,A.: Field emission from quantum size GaN structures. Applied Surface Science 220, 46–50 (2003).
38. Martinelli, R.U., Pankove, J.I.: Secondary electron emission from the GaN:Cs-O surface. Appl. Phys. Lett. 25, 549-551 (1974).
39. Monch, W., Kampen, T.U., Dimitrov, R., Ambacher, O., Stutzmann, M.: Negative electron affinity of cesiated p-GaN(0001) surfaces. J. Vac. Sci. Technol. B 16, 2224-2228 (1998).
40. Machuca, F., Zhi, L., Sun, Y., Pianetta, P., Spicer, W.E., Pease, R.F.W.: Oxygen species in Cs/O activated gallium nitride (GaN) negative electron affinity photocathodes. J. Vac. Sci. Technol. B 21, 1863-1869 (2003).
41. Novoselov, K. S., Geim, A. K., Morozov, S. V., Jiang, D., Zhang, Y., Dubonos, S. V., Grigorieva, I. V., Firsov, A. A.: Electric Field Effect in Atomically Thin Carbon Films. Science 306, 666(2004).

42. Novoselov, K. S., Geim, A. K., Morozov, S. V., Jiang, D., Katsnelson, M. L., Grigorieva, I. V., Dubonos, S.V. & Firsov, A.A.: Two-dimensional gas of massless Dirac fermions in graphene. Nature 438, 197(2005).
43. Balandin, A. A., Ghosh, S., Bao, W., Calizo, I.: Superior Thermal Conductivity of Single-Layer Graphene Nano Lett., 8, 902-907(2008)
44. Romero, H. E., Joshi, P., Gupta, A. K., Gutierrez, H. R., Cole, M. W., Tadigadapa, S. A., and Eklund, P. C.: Adsorption of ammonia on graphene. Nanotechnology 20, 245501(2009).
45. Lu, G., Ocola, L. E., and Chen, J..: Reduced graphene oxide for room-temperature gas sensors. Nanotechnology 20, 445502(2009).
46. Leenaerts,O., Partoens, B., and Peeters, F. M..: Adsorption of H2O, NH3, CO, NO2, and NO on graphene: A first-principles study. Phys. Rev. B 77, 125416(2008).
47. Ko, G., Kim, H. Y., Ahn, J., Park, Y. M., Lee, K. Y., and Kim, J.: Graphene-based nitrogen dioxide gas sensors. Current Appl. Phys. 10, 1002(2010).
48. Saffarzadeh, A.: Modeling of gas adsorption on graphene nanoribbons. J. of Appl. Phys. 107, 114309(2010).
49. Leenaerts, O., Partoens, B., and Peeters, F. M.: Water on graphene: Hydrophobicity and dipole moment using density functional theory. Phys. Rev. B 79, 235440(2009).
50. Wehling, T.O., Lichtenstein, A.I., and Katsnelson, M.I.: First-principles studies of water adsorption on graphene The role of the substrate. Appl. Phys. Lett. 93, 202110(2008).
51. Yavari, F., Kritzinger, C., Gaire, C., Song, L., Gulapalli, H., Tasciuc, T. B., Ajayan, P. M., and Koratkar, N.: Tunable Bandgap in Graphene by the Controlled Adsorption of Water Molecules. Small 6, 2535 (2010).

CHAPTER 2

EXPERIMENTAL EQUIPMENT AND SAMPLES

2.1 The Ultra High Vacuum (UHV) Preparation Chamber for Field Emission Study

The field emission study in this work needs to be conducted in a base vacuum of 10^{-9} Torr or below. An ultra-high vacuum (UHV) system was used in these field emission experiments. (See Figure 2.1). All devices and materials involved in the vacuum chamber, including sealing and wiring, are high vacuum compatible and will not re-contaminate the sample during out-gassing and heating processes. Thermal heating tapes are wrapped outside to heat the chamber for out- gassing. A mechanical pump, a turbo-molecular pump, and an ion pump are employed to obtain the desired vacuum. A thermo couple gauge is used to monitor the pressure between mechanical pump and turbo-molecular pump for a primary vacuum. An ion gauge is used to monitor the pressure of the chamber for base vacuum and gas leaking measurements. Two gate valves are used, between the chamber and the turbo-molecular pump and between the chamber and the ion pump, to allow continuous operation. An 8-inch flange on the top of the chamber is used to seal the chamber every time the sample is placed for a measurement. Once the sample is placed and sealed in the chamber the mechanical pump starts to pump. The mechanical pump can provide primary vacuum of up to 10^{-3} Torr. The turbo pump starts to pump the chamber after the mechanical pump is turned on and it should reach its half speed, 750 Hz (rotation per second) before the thermal couple gauge indicates the pressure is below 1 Torr, such that the oil molecules from mechanical pump are prevented from going into the chamber by the turbo. With the mechanical and the turbo pump, the pressure of the chamber can be brought down to 10^{-7} Torr. The ion pump is turned on after the pressure

reaches 10^{-7} Torr to lower pressure down to 10^{-9} Torr. The chamber and ion pump are wrapped with thermal tapes and aluminum foil for heating and out-gassing. When the chamber reaches the pressure of 10^{-7} Torr, a 72 hour proces of heating at 100°C process is follows. After cooling down from heating, the vacuum of chamber can reach 10^{-9} Torr or below. The studies of ZnO and GaN nanorod field emission properties were conducted in this chamber. A Varian leak valve was used between the chamber and gas distribution system for pressure control of various gases.

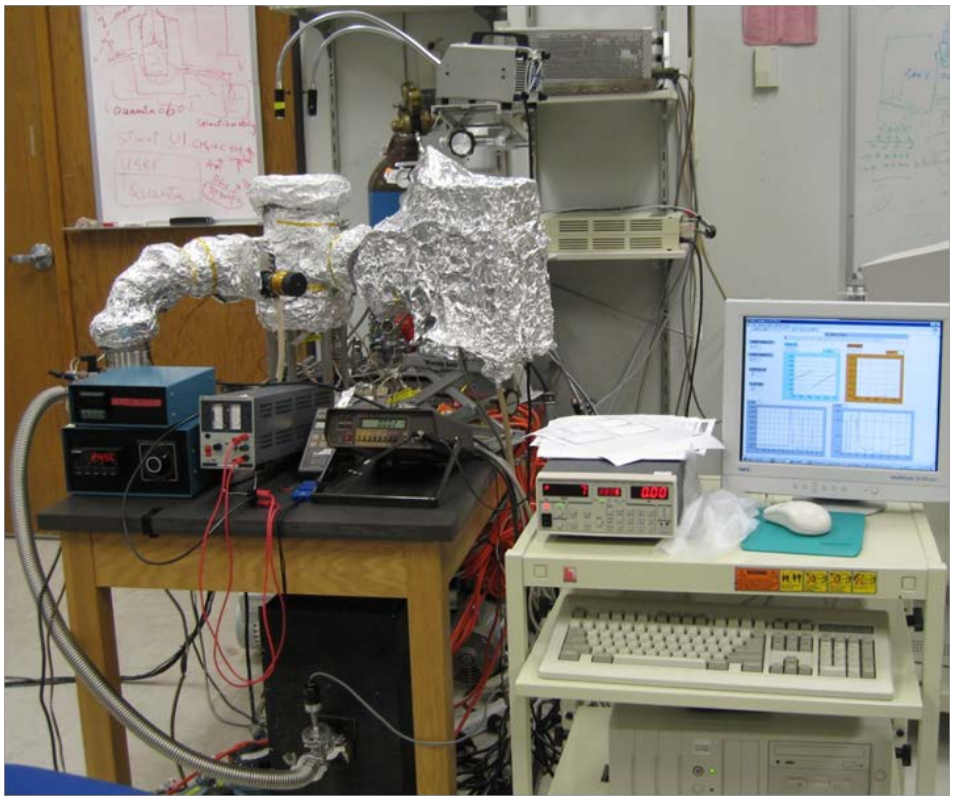

Figure 2.1. Field emission property measurement systems for ZnO, GaN and ZnS nano structures.

Figure 2.2 shows the chamber, the turbo-molecular pump, the ion pump, and connections to the mechanical pump as well as the gauges, and the feed-through for

measurement. I-V characteristics of the sample are measured using a Keithley 485 Auto ranging Picoameter and Keithley 487 Picoameter/Voltage Source programmed with Labview for data acquisition.

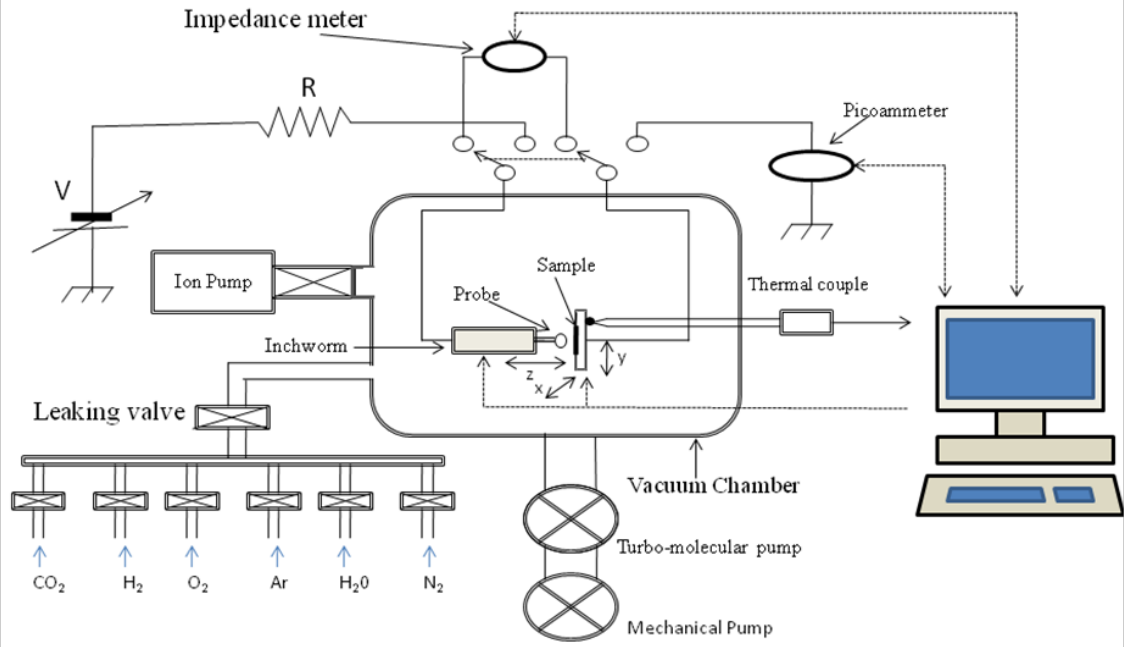

Figure 2.2. Schematic illustrations of the field emission measurement and data acquisition system.

2.2. The UHV System for Cs Deposition of GaN Nanostructures

The effect of Cs deposition on the field emission properties of GaN nanorods was studied in another UHV chamber. The Cs deposition experiment with GaN nanorods required measuring the field emission properties of a sample before and after Cs deposition for the comparison of field emission changes in a UHV environment without exposure to air. The sample needed to be transferred between where the field emission was measured and where the Cs deposition was conducted. The UHV STM Chamber customized by MCD Vacuum Products Corporation [1] was employed in this study. The

vacuum procedure is similar to that described in 2.1, but this chamber is equipped with a larger turbo-molecular pump and a larger ion pump, in addition to a titanium sublimation pump and a baking box for the whole system; with those, the vacuum of the chamber can reach to the 10^{-10} Torr level and UHV (as low as 10^{-11} Torr). Two linear translators are used to transport the sample from loading chamber to the position of measuring field emission and to the position of Cs deposition. A special sophisticated scanning tunneling microscope (STM) sample holder is used to place up to 3 samples at a time and manipulate samples between two translators for sample transportation in-situ in the UHV environment. A residual gas analyzer (SRS RGA 200) is attached to the chamber to monitor the residual gases and for leak checking. Figure 2.3 shows the UHV system used for GaN nano-structure Cs deposition field emission measurement equipped with residual gas analysis.

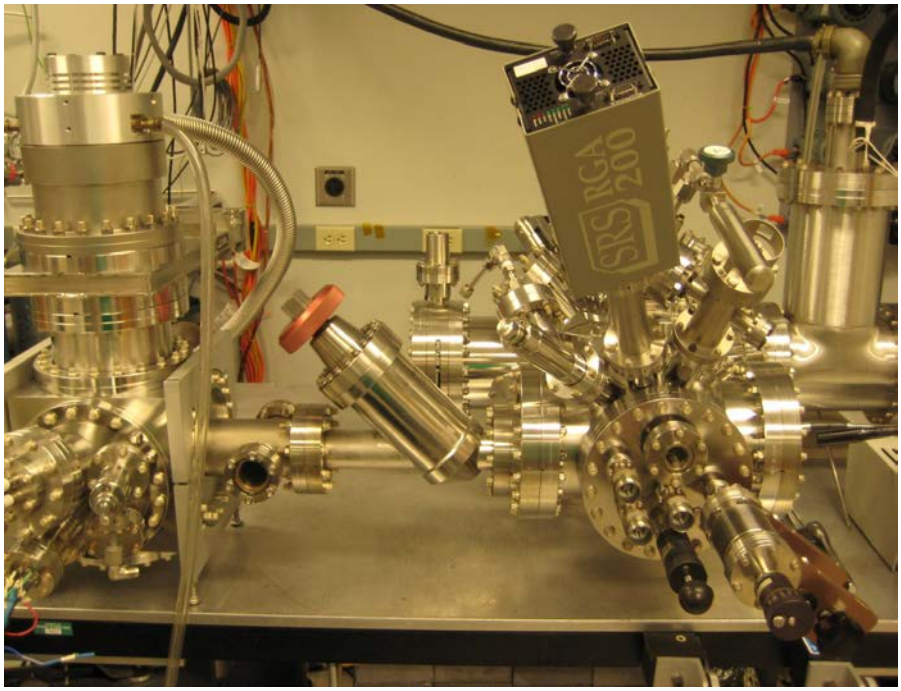

Figure 2.3. UHV system for GaN nano-structure Cs deposition field emission measurement.

Figures 2.4 and 2.5 show the schematic top and side views of the UHV chamber and STM system. Figure 2.6 shows the residual gas analysis at a vacuum of 5×10^{-9} Torr by the RGA.

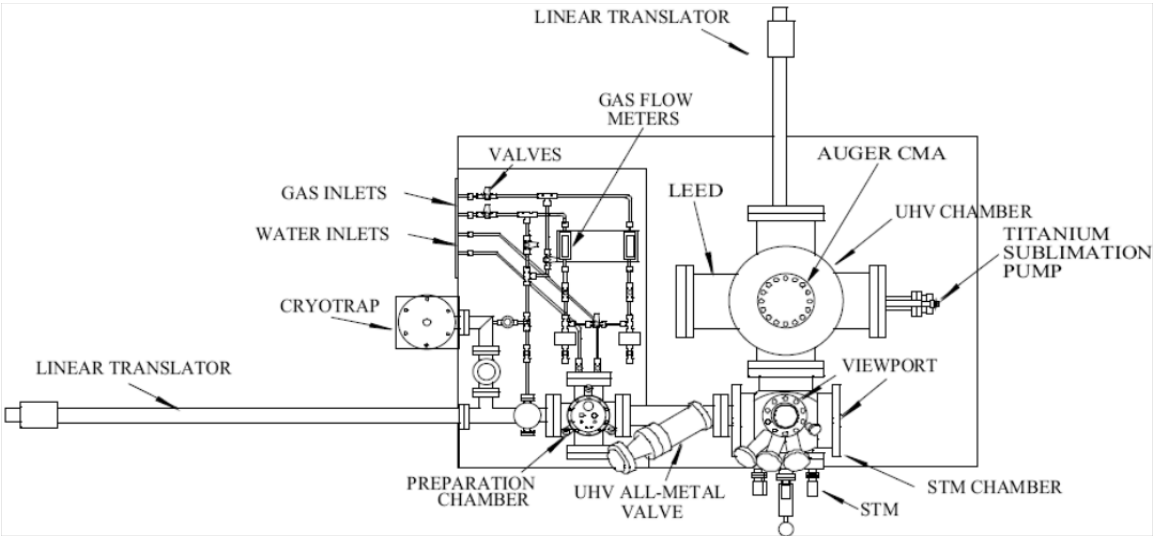

Figure 2.4. Schematic top view of the UHV chamber and STM system.

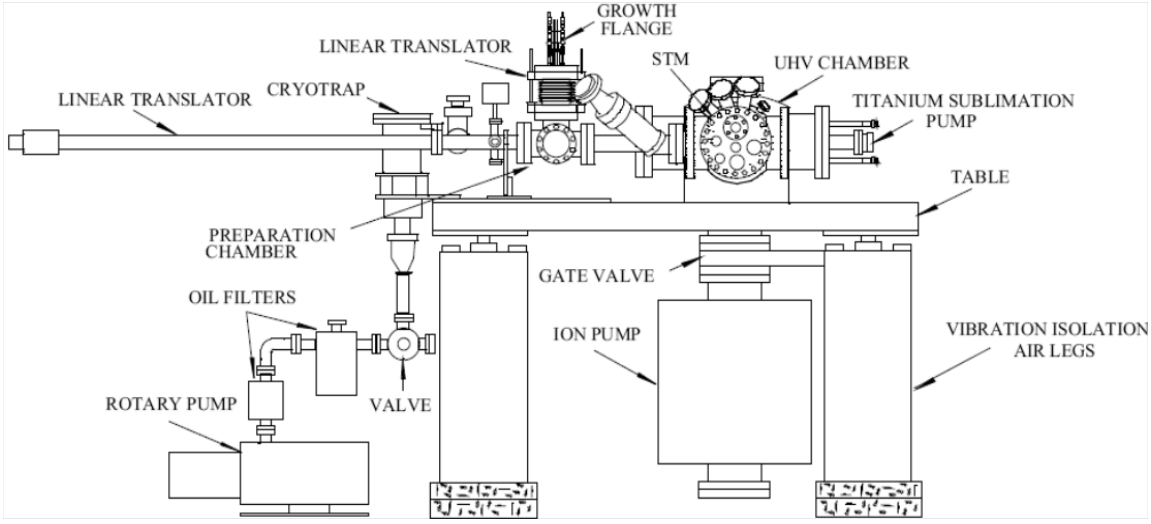

Figure 2.5. Schematic side view of the UHV chamber and STM system.

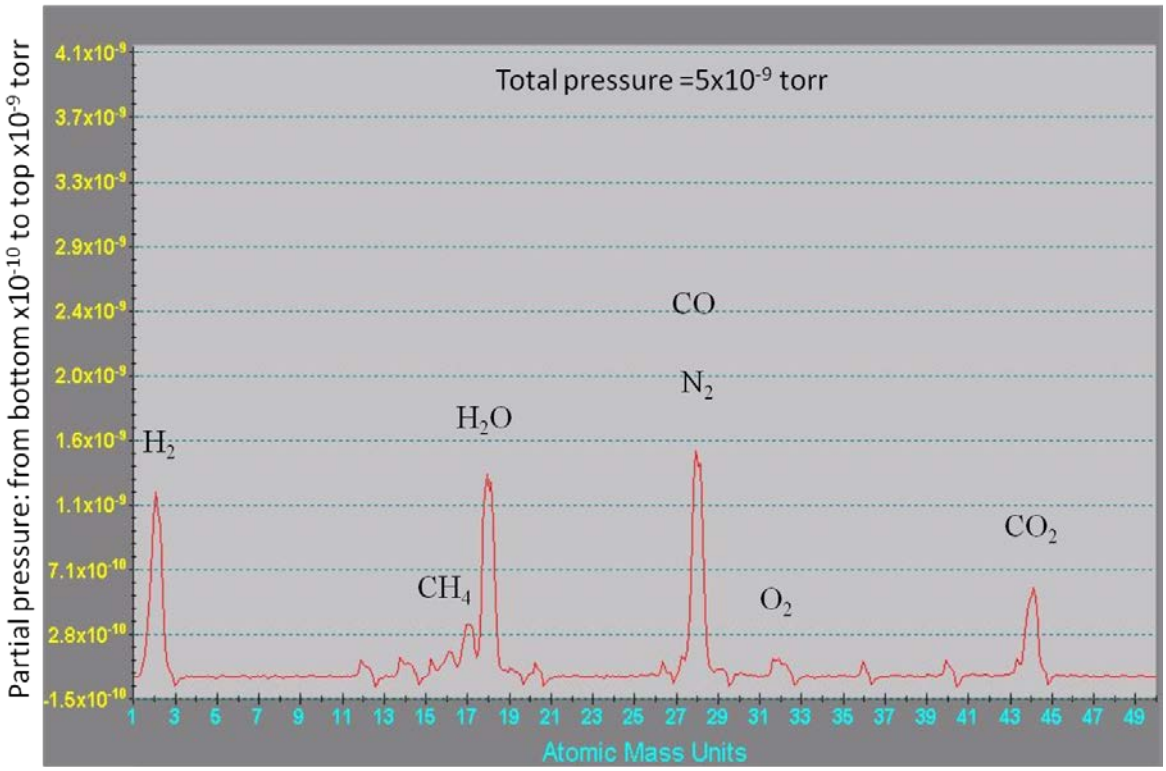

Figure 2.6. Residual gas analysis read from RGA.

2.3. The UHV STM Positioning System

The field emission measurement, in general, is to measure the emission current vs. the voltage applied between an anode and the cathode which is formed with nano-material films. The emission current is strongly dependent on the distance between the anode and the films on a micro-meter scale. Therefore, precise controlling and measuring of the distance between the anode and cathode are crucial. The Aris 5000 UHV-compatible Scanning Tunneling Microscope (STM) made by Burleigh instruments Inc. [2] is used to achieve the controlling and distance measurement of the precise positioning of the anode. This system consists of two piezo actuators, an inchworm motor and a scanning tube. The inchworm motor can be driven by applied voltages, and so move the attached anode tip forward and backward from as slow as 2 nanometers per second up to one hundreds of micrometers per second. The piezo is activated by controlling voltages

and is capable of moving in the x, y and z directions with ranges of 10 micrometers. The positioning assembly and the sample housing set-up are seated on a vibration buffering system for the case of gas effects on field emission; See Figure 2.7. or a stainless steel base mounted on a vibration isolation system was used for the case of Cs deposition; see Figure 2.8.

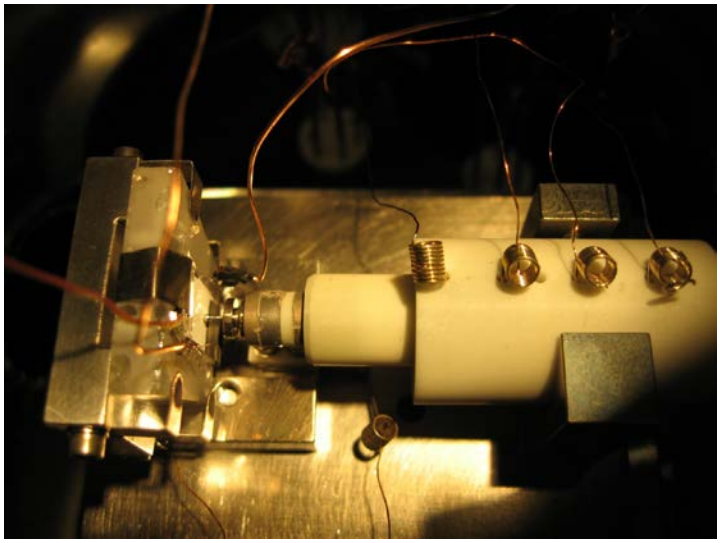

Figure 2.7. Sample holder and inch-worm of field emission position system for gas exposure.

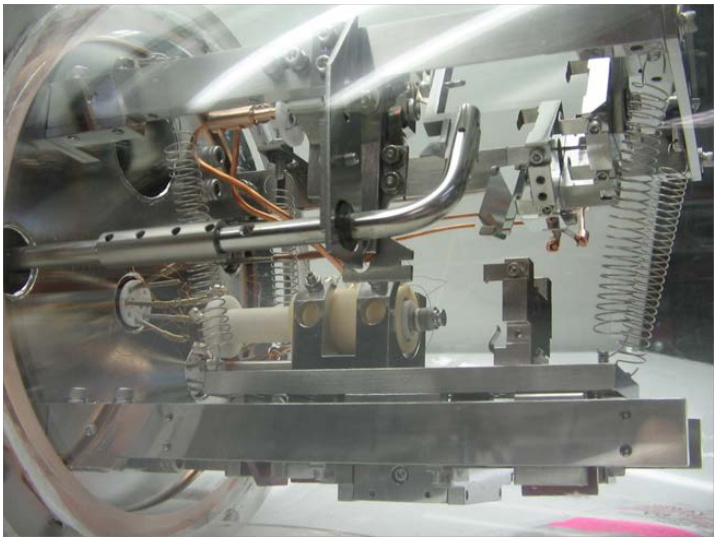

Figure 2.8. Sample holder and inch-worm of field emission position system for Cs deposition.

All the positioning movements are controlled by a computer through an electronic controlling unit. The anode tip can be either manually-controlled or computer-controlled to move in both fast speed mode and slow speed mode, so that the sample can be easily loaded with the fast speed mode and the desired position can be precisely achieved with slow speed mode. A CCD camera equipped with a telescope and a monitor for positioning outside the chamber, is used to assist in carrying out this process. The telescope focuses on the sample stage through a viewport and the camera captures the image on the monitor for positioning tip and sample. For sample loading, the chamber is opened by removing the 8-inch viewport flange. After loading the sample, the 8-inch viewport flange is sealed with a new copper gasket. The anode tip retracts in fast speed mode to leave enough space for the sample loading process. After the sample is properly loaded with the tip far from the sample surface, the anode tip is then moved rapidly to approach the sample film. When the tip is close to the sample surface--a few hundred micrometers away from sample surface--the moving mode is switched to slow mode for a more precise control and to avoid crashing into the sample. The distance between the anode and tip is monitored by an enlarged image with the monitor through the camera and telescope. While the tip is approaching the sample, a voltage of 10 volt is applied between the tip and sample, and a picoammeter is used to monitor the current between tip and sample, in case the tip and sample get too close and field emission occurs. In such a way tip-sample contact can be avoided together with the cooperation of camera-telescope monitoring and current monitoring. The slow mode speed is adjustable and can be set by a numerical scale from 0 to 100. The actual speed can be calibrated with a timer and the moved distance measured in the enlarged image of moving parts in the chamber displayed on the monitor. When the tip approaches the sample surface and is so close to

the surface that the optical image cannot be used to monitor the gap between the tip and sample, the very slow mode and set-up need to be used to further approach the sample surface but avoid touching the sample. When a voltage of 10 v is applied to tip and sample, a field emission with very small current (10^{-12} A) occurs when the tip is almost touching the sample but not actually touching (if it touched the current would be over 10^{-9} A). This gives the signal to stop moving the tip, and this is also the position considered as the surface of the sample, and the distance of the tip from the sample will be measured and used from here by retracting the tip with the inchworm.

2.4 Cesium Metal Dispenser

The Cs metal dispenser attached with a vacuum sealing port angled into the UHV chamber was purchased from SAES [3]. The dispenser is heated by running current through wires passing through the port. The heating makes a reduction reaction and subsequently evaporates the free alkali metal Cs onto the sample. The Cs evaporation yield has been precisely calibrated by SAES and under the required operating conditions, the amount of Cs can be controlled at a scale of a few µg/minute and µg/cm^2, or 10^{16} Cs atoms per minute. Figure 2.9 shows the Cs metal dispenser.

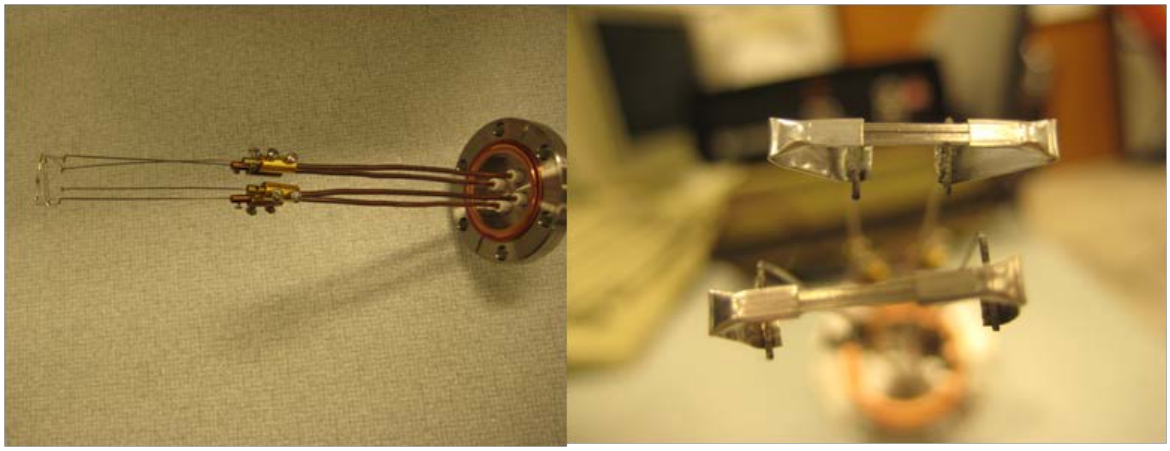

Figure 2.9. Cs metal dispensers from SAES with 2.5 cm active emitting wire.

2.4 Sample preparations

ZnO nanorod powders: ZnO nanorods 100-200nm in width and 300-600nm in length were synthesized using the DC arc discharge method with a Zn target, air pressure of 600 Torr and arc current of 30A. These were provided by Dr.Fujita's group from Dr. Yasuhisa Fujita at Shimane University in Japan.

Substrate: A piece of heavily doped P-type Si substrate 0.7 cm by 1.6 cm in size with 1000 Angstroms of silver coated by vacuum evaporation on to surface for electrical contact was used.

1 mg ZnO nanorod powder was dispersed into 20ml ethanol and sonicated for 1 hour to form a uniform suspension. The substrate was placed on a hot plate and heated to a temperature of about 120 C˚, then a few drops drops of the suspension were deposited on the silver layer and allowed to dry. The ZnO layer was about 1 μm thick. The heating at 120 C˚ allowed the suspension to dry quickly and form a uniform layer. Several drops of the mixture was sufficient to form an even layer for the experiment. Figure 2.10 shows optical and SEM images of ZnO nanorods on the substrate.

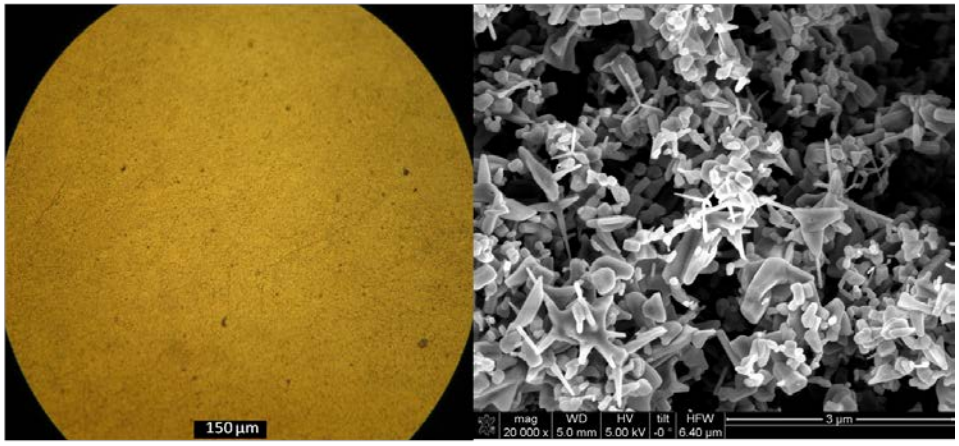

Figure 2.10. Optical image (left) and scanning electron microscopy (SEM) image (right) of ZnO nanorods sample deposited on silver-coated heavily doped P type substrate.

GaN samples: These samples were grown by molecular beam epitaxy (MBE) and were obtained from Dr. Q.Y Chen at National Sun Yat-Sen University, Taiwan. See Figure 2.11.

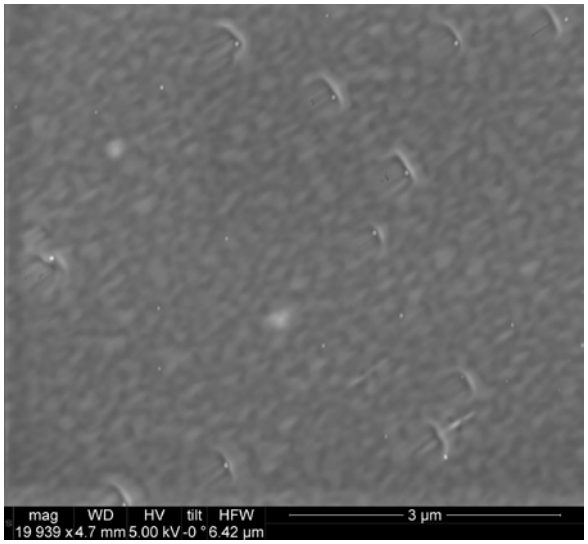

Figure 2.11. Scanning electronic microscopy image of GaN nanostructures.

ZnS samples: There were grown from aqueous solution by Jeffrey Schwartz in our lab. See Figure 2.12.

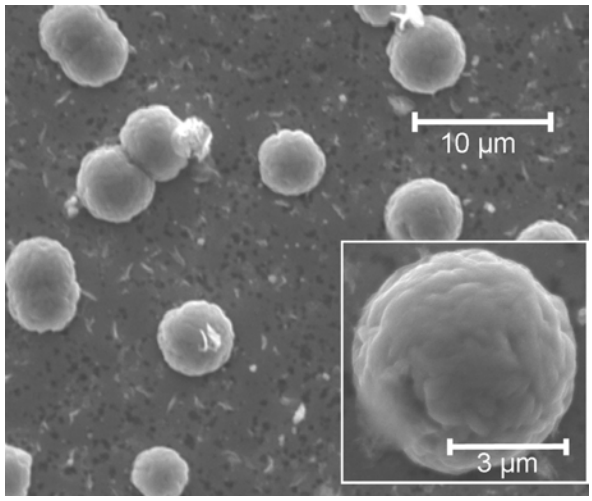

Figure 2.12. Scanning electronic microscopy image of ZnS.

Exfoliated graphene samples: There were isolated from HOPG (highly ordered pyrolytic graphite) onto a SiO2/Si substrate and made into a device with vacuum metal deposition in our lab. Figure 2.13 shows the process.

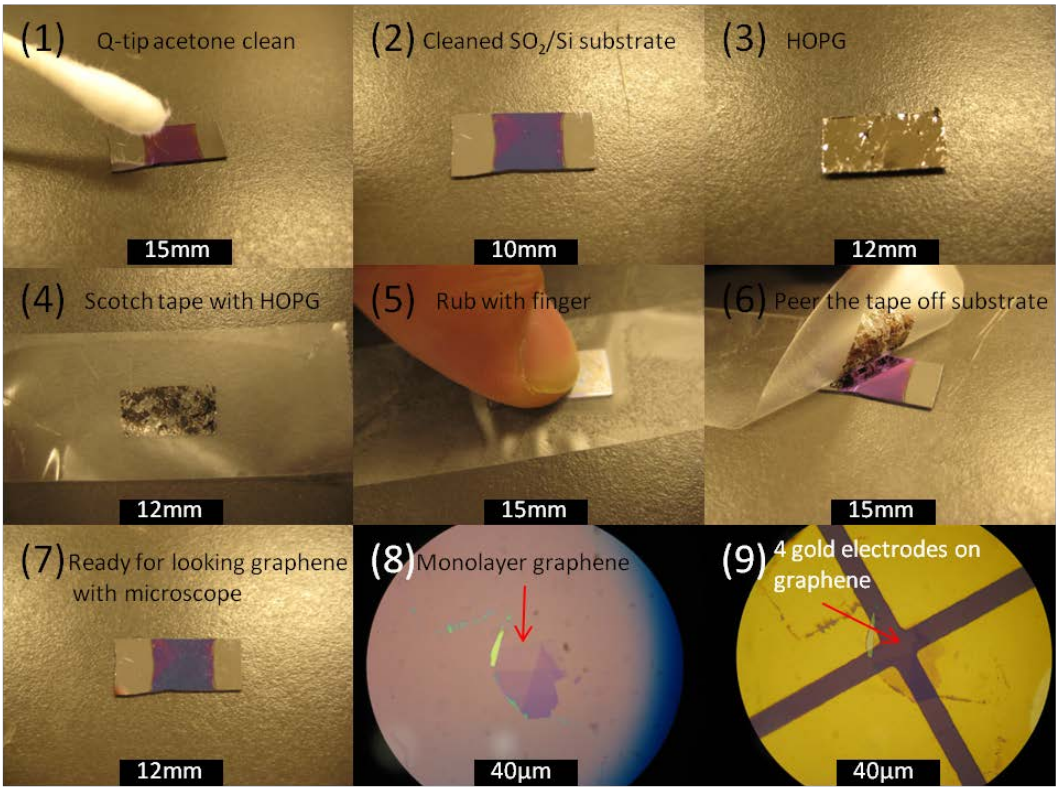

Figure 2.13. Fabrication steps of exfoliated graphene and device.

CVD graphene samples: There were grown and made into a device with vacuum metal deposition in our lab. See details in section 4.2.

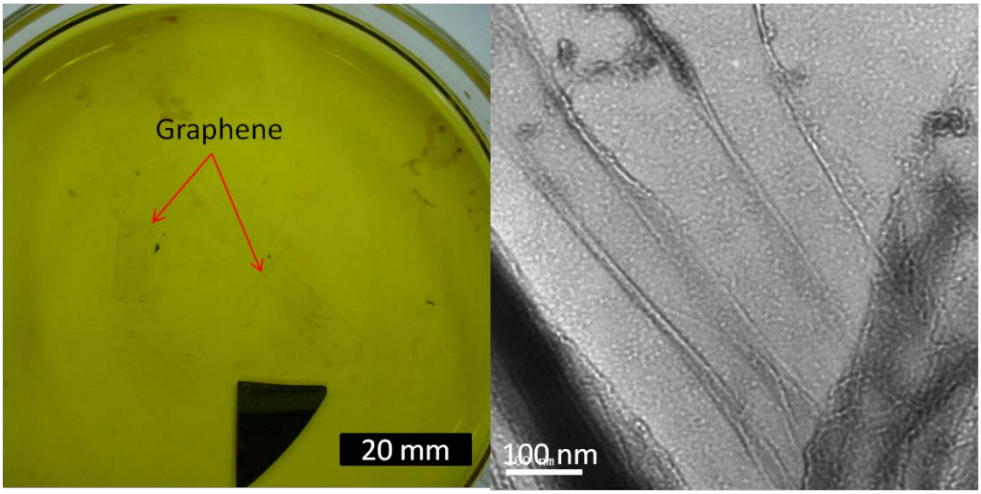

Figure 2.14. CVD-grown graphene on water (left) and its TEM image (right).

2.6 References

1. MDC Vacuum Products Corporation, 23842 Cabot Blvd, Hayward, CA 94545-1651, (510)265-3500
2. Burleigh Instruments, Inc., 7647 Main Street, Fishers, NY 14453, (585) 924-9355
3. SAES Getters, INC., 1122 E Cheyenne Mountain Blvd, Colorado Spring, CO 8090

CHAPTER 3

FIELD EMISSION PROPERTIES OF ZnO, ZnS, and GaN NANOSTRUCTURES*

In this chapter, we review the growth and field emission (FE) properties of ZnO, ZnS and GaN nanostructures. For ZnO nanostructures, we discuss in detail solution-based growth techniques, and the effects of residual gas exposure on the FE properties. We present new results showing that O_2 and CO_2 exposure do not have a significant effect on the FE properties of ZnO nanorods, but N_2 exposure significantly degrades them. We also present new results showing that Cs deposition significantly improves the FE properties of GaN nanorods.

3.1 Introduction

ZnO, ZnS and GaN nanostructures have been recently investigated as field emission (FE) electron sources for potential applications in flat panel displays and other vacuum microelectronic applications. In particular, ZnO nanostructures have received considerable interest [1-15]. The motivation is to discover new FE materials with improved properties over carbon nanotubes and Spindt-type metal microtips such as Mo microtips. Carbon nanotubes and metal microtips have been extensively studied for FE applications due to their low turn-on voltages of 1-10 V/μm [16-26]. However, the FE properties of carbon nanotubes and metal microtips degrade significantly with exposure to O_2 and oxygen-containing gases typically found in vacuum containers of flat panel displays [17, 18,23-26].This leads to operating lifetimes that are too short for commercial applications.

---

*The majority of this chapter is reproduced from *Nanoscale Photonics and Optoelectronics*, Chapter 7: "Field emission properties of ZnO, ZnS and GaN Nanostructures" by Z.M. Wang & A. Neogi (eds.), with kind permission of Springer Science and Business Media. Reference and figure numbers have been changed to accommodate this dissertation. Material in this chapter reproduced from other sources are identified in footnotes on the page where they appear.

The degradation is thought to be due to oxidation of carbon and metals under the high-electric-field conditions present during FE. It is thought that oxide-based materials such as ZnO may be less susceptible to oxidation since it is difficult to further oxidize ZnO [27]. In addition, wide-band gap semiconductors such as ZnO (3.4 eV), ZnS (3.6 eV) and GaN (3.5 eV) may exhibit band bending at the surface such as negative electron affinity (NEA) that may reduce the barrier for FE [28].

In this chapter, we discuss the growth and FE properties of ZnO, ZnS and GaN nanostructures, with an emphasis on ZnO nanorods. We discuss in detail solution-based techniques for the growth of ZnO nanorods that are well suited for commercial applications such as flat panel displays. The effects of residual gases such as O_2, CO_2, N_2, H_2, Ar and other gases on the FE properties of ZnO and GaN nanostructures are discussed in detail. We present new results showing that the FE properties of ZnO nanorods grown using the DC arc discharge technique are not significantly degraded by exposure to O_2 and CO_2, but are significantly degraded by exposure to N_2. This is thought to be due to the higher reactivity of nitrogen with ZnO. In addition, we present new results on the effects of Cs deposition on the FE properties of GaN nanorods. Cs deposition is observed to reduce significantly the turn-on voltage by approximately 50%. We propose that this is due to a reduced barrier or NEA surface induced by the Cs. It would be interesting to investigate if Cs deposition reduces the turn-on voltage of ZnO, ZnS and other wide-band gap nanostructures.

3.2 ZnO Nanostructures

A wide range of techniques have been successfully employed in the production of ZnO nanostructures. Such techniques can generally be categorized as vapor or

solution-based techniques. The ZnO nanostructures produced using these methods may exist as one of a variety of different possible morphologies such as ZnO nanorods, nanoneedles, nanoribbons, nanodisks, and nanorings. Vapor-based techniques were the first used to grow ZnO nanostructures and include vapor-liquid-solid (VLS) [29-32], chemical vapor deposition (CVD) [33], plasma-enhanced CVD [34], metal-organic CVD (MOCVD) [35-39], metal-organic vapor phase epitaxy (MOVPE) [40,41], molecular beam epitaxy [42,43] and template-assisted growth processes [44]. Vapor-based techniques can be used to grow a variety of ZnO nanorods including vertically-aligned arrays of ZnO nanorods, nanorod heterostructures [45], and alloyed and doped nanorods [46-48]. The FE properties of vapor-grown ZnO nanostructures have been extensively studied and found to be comparable to those of carbon nanotubes [1-15]. Recently, solution-based or hydrothermal techniques using zinc salts in an aqueous solution were developed in which ZnO nanostructures could be grown at low temperatures of about 100 ^{o}C [49-59]. Nanorods could be grown as suspended particles in solution or attached to a substrate in a random or vertically-aligned configuration. Solution-based growth techniques can be more easily scaled to large deposition areas since they are less expensive and use significantly lower temperatures than vapor-based techniques. The FE properties of vapor and solution-grown ZnO nanostructures have been reported to be the same [28,60-62]. Thus, solution-based techniques are well suited for mass production of flat panel displays and other large-area FE applications.

In VLS techniques, catalyst nanoparticles such as Au, Ni, Co, Cu or Sn are used and remain embedded in the tips of the ZnO nanostructures as they grow [29-32]. The growth mechanism involves the dissolution of Zn vapor into the catalyst nanoparticles at high temperatures of about 900 ^{o}C. The Zn precipitates out upon saturation and oxidizes

to form ZnO. This technique can be used to grow nanorod heterostructures having different compositions along the axial direction. However, the interfaces in the heterostructures are usually not sufficiently abrupt to produce quantum confinement effects due to alloying caused by the embedded nanoparticles [63]. The embedded nanoparticles also produce defect sites that may lead to oxidation and degradation of FE properties. Another disadvantage of VLS techniques is that they involve the use of vacuum that makes the process costly.

Recently, MOCVD and MOVPE growth techniques have been developed that do not require the use of catalyst nanoparticles [35-41]. These techniques can be used to grow nanorods in a random, vertically-aligned or mosaic pattern depending on the substrate, growth temperature and Zn/O precursor ratio [39]. Using MOVPE, it is possible to grow high-quality nanorod heterostructures having abrupt interfaces exhibiting quantum effects [45]. Other vapor-based techniques include physical vapor deposition such as thermal evaporation of powders of Zn [64,65], ZnO [66,67], ZnO and SnO_2 or In_2O_3 [68,69], or ZnO and graphite [70].

In addition, there are pulsed laser deposition (PLD) [71] and DC arc discharge [72] techniques. PLD has, until recently, received only limited attention as a means to prepare ZnO nanorods compared to the previous methods discussed, despite its widespread use in the manufacture of thin films of ZnO and other materials. ZnO nanorods only form within a certain range of temperatures and pressures by PLD, outside of which a thin film is deposited instead. This restriction on growth conditions, as well as the expense of the equipment necessary for the process, may contribute to PLD's lower popularity in ZnO nanostructure preparation compared to other methods. The PLD

method does, however, possess the advantages of one's ability to dynamically and easily alter the partial pressures of the gases present during deposition, as well as the close correspondence of the chemical makeup of the deposited ZnO to that of the source material, allowing one to control easily the level of doping. The DC arc discharge technique involves a DC arc discharge in air. Figure 3.1 shows a scanning electron microscopy (SEM) image of ZnO nanorods grown using the DC arc discharge technique with a Zn target, air at a pressure of 610 Torr and arc current of 30 A [72]. The nanorods measure approximately 100-200 nm in width and 300-600 nm in length. They are *n*-type due to donor formation by oxygen vacancies and impurities.

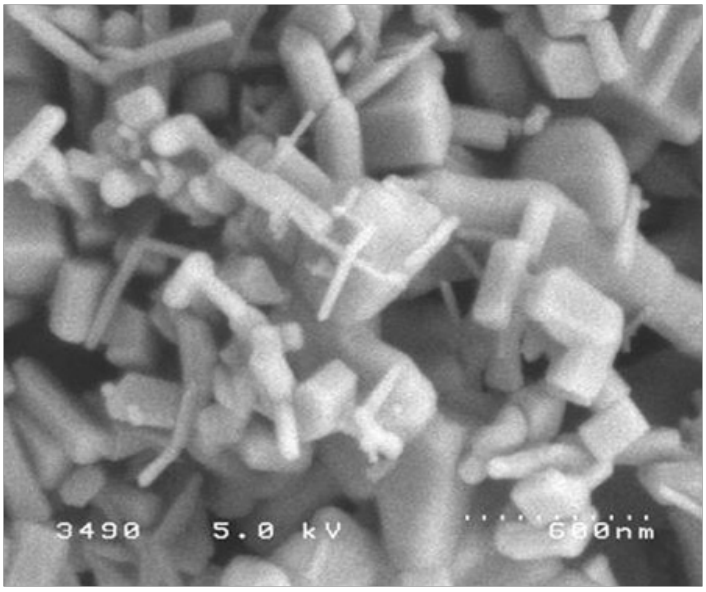

Figure 3.1. Scanning electron microscope image of ZnO nanorods grown using the arc discharge technique. Scale denotes 600 nm.

Solution-based or hydrothermal techniques for the growth of ZnO nanostructures use an aqueous solution of a zinc salt that is thermally decomposed at low temperatures of about 100 ^{o}C to produce ZnO [49-59]. The growth solution is typically made of an equimolar mixture of a zinc salt, such as $Zn(NO_3)_2 \cdot 6H_2O$, and hexamethylenetetramine,

also known more simply as hexamine or methenamine, with concentrations on the order of 10 mM [49]. Additionally, an amine complexing agent, such as ammonia, is regularly added to the growth solution in order to promote heterogeneous epitaxial growth of the ZnO during nanorod formation. A variety of substrates can be used such as glass, single crystal sapphire, Si/SiO_2 wafers, ZnO thin films, Zn foils and other metals. The solution is heated to a temperature ranging between 70 to 100 ^oC for several hours producing random or vertically aligned ZnO nanorods depending on the substrate material, temperature, Zn^{2+} concentration and pH of the solution [49].

Figures. 3.5-3.8 show SEM images of various ZnO nanostructures grown using solution-based techniques. Uniformly distributed and well-aligned ZnO nanorods were grown perpendicular to the substrate surface as single crystals with an easily distinguishable hexagonal-rod structure.

The growth solution for the nanostructures in Figures. 3.5-3.8 was prepared using equimolar mixtures of a zinc salt and hexamine. The pH was adjusted with a dilute solution of ammonium hydroxide or an acid containing the corresponding anion of the zinc salt used. The substrate was mounted vertically inside an autoclavable glass vial containing the prepared growth solution. The sealed vial was immersed in a water bath at the desired temperature maintained by a programmable hot plate. The zinc salts used to prepare the growth solution include zinc nitrate (NO_3^-), sulfate (SO_4^{2-}), chloride (Cl^-), and acetate (CH_3COO^-), and ranged in concentration from 0.1 M to 5.0 mM. The ZnO nanostructures were allowed to grow for 2 to 5 hours at temperatures between 60 and 80 °C. A variety of substrates were used including silver, copper, nickel, silicon, and glass.

†Figure 3.2 shows the setup of aqueous growth of ZnO nanorods and Figure 3.3 and 3.4 give Raman spectra and EDAX of ZnO nanorods made in our lab.

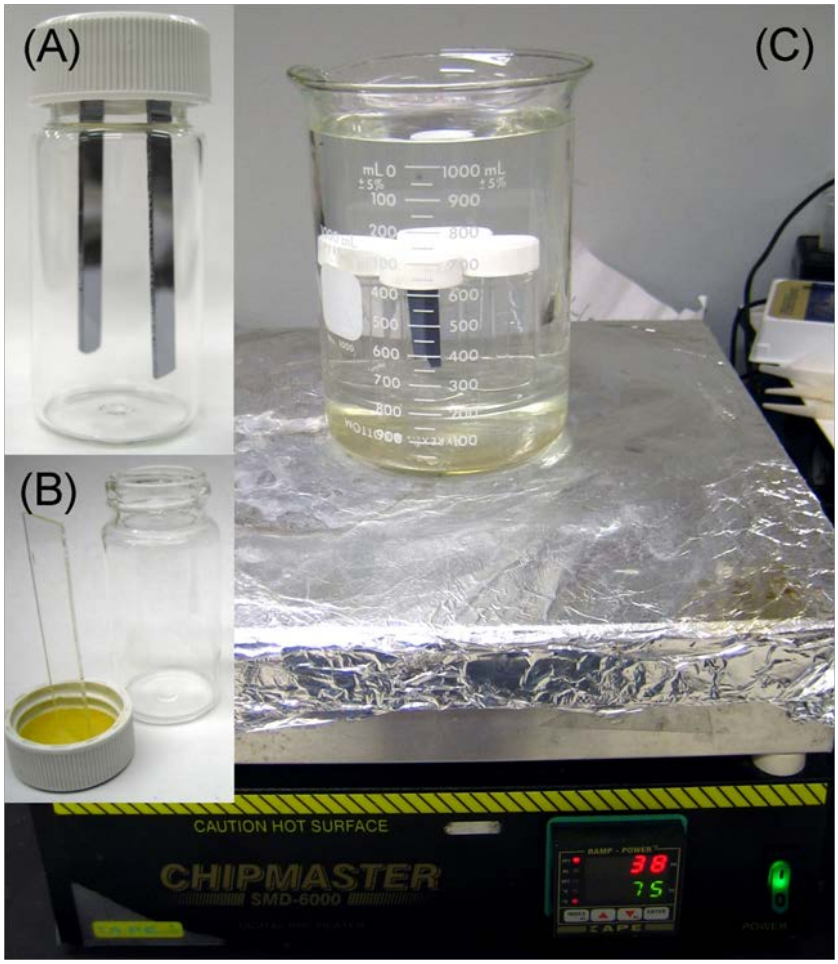

Figure 3.2. Aqueous growth of ZnO nanorods (A) Sealed growth vial with two Silicon substrate holders; (B) Disassembled growth vial with glass substrate holder; (C) Several growth vials in water bath placed on hot plate.

†Figures 3.2-3.4 and paragraphs in section 3.5 indicated with cross (†) are from work done with Jeffrey Schwartz in our lab, with REU (Research Experiences for Undergraduates summer program).

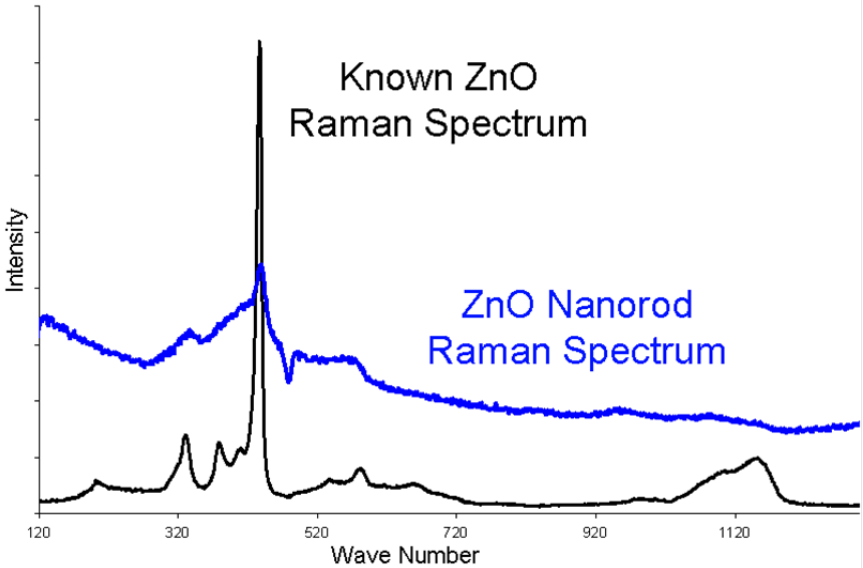

Figure 3.3. Raman Spectra of known zinc oxide sample and ZnO nanorods.

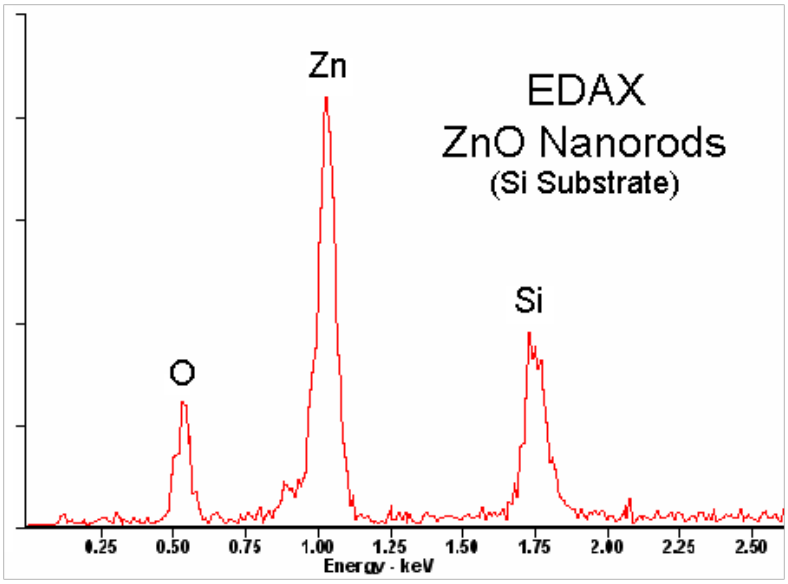

Figure 3.4. Energy-dispersive X-ray spectroscopy (EDAX) measurements of ZnO nanorods on a silicon substrate.

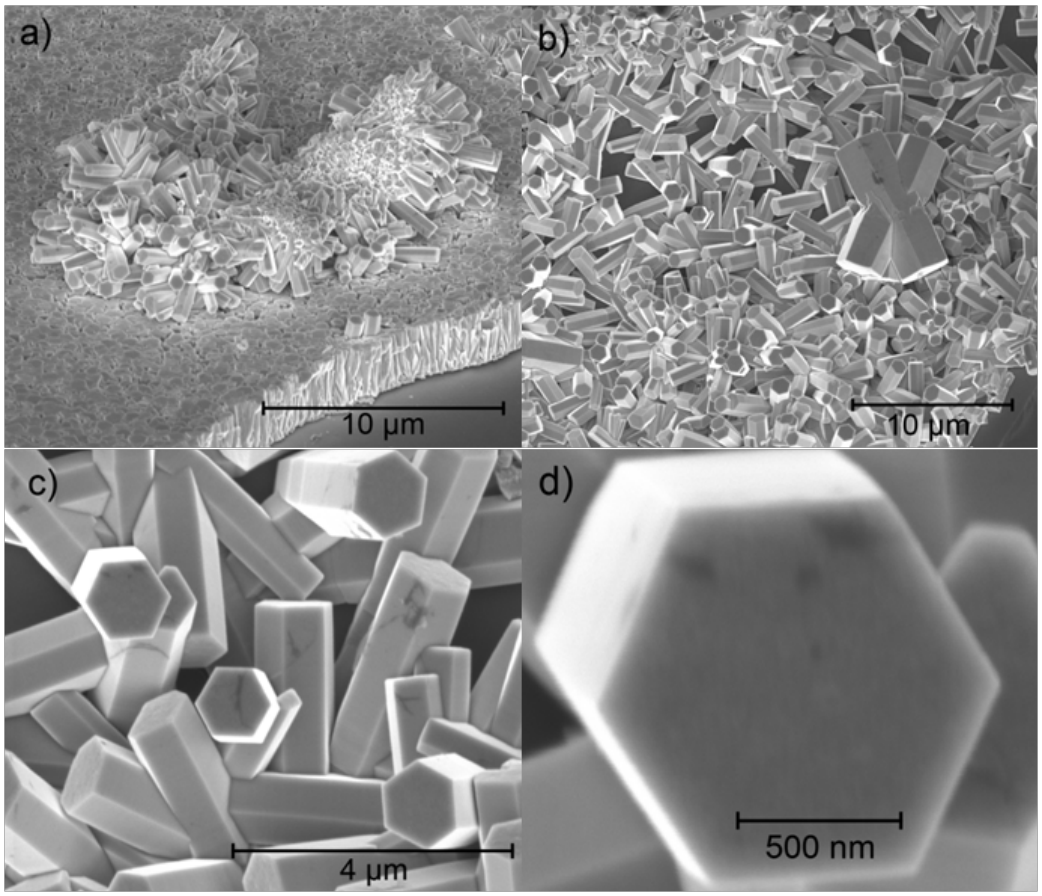

Figure 3.5. High-resolution scanning electron microscope images of ZnO nanorods prepared on a silver-coated Si wafer.

Equimolar mixtures of 0.05 M $Zn(NO_3)_2$ and hexamine were used as the growth solution. The nanorods were grown at 60 °C for 3 hours. (a) Tilted view (58°) of the edge of the sample showing a highly aligned structure of nanorods with uniform height. Also visible is a ZnO nanorod cluster that is embedded into the layer grown on the surface. (b), (c), (d) increasingly magnified images of a disordered section on the surface that allows an excellent assessment of the individual nanorod morphology and

size. Nanorods are shown to grow with uniform size distribution with clearly defined crystal facets and hexagonal cross sections

.

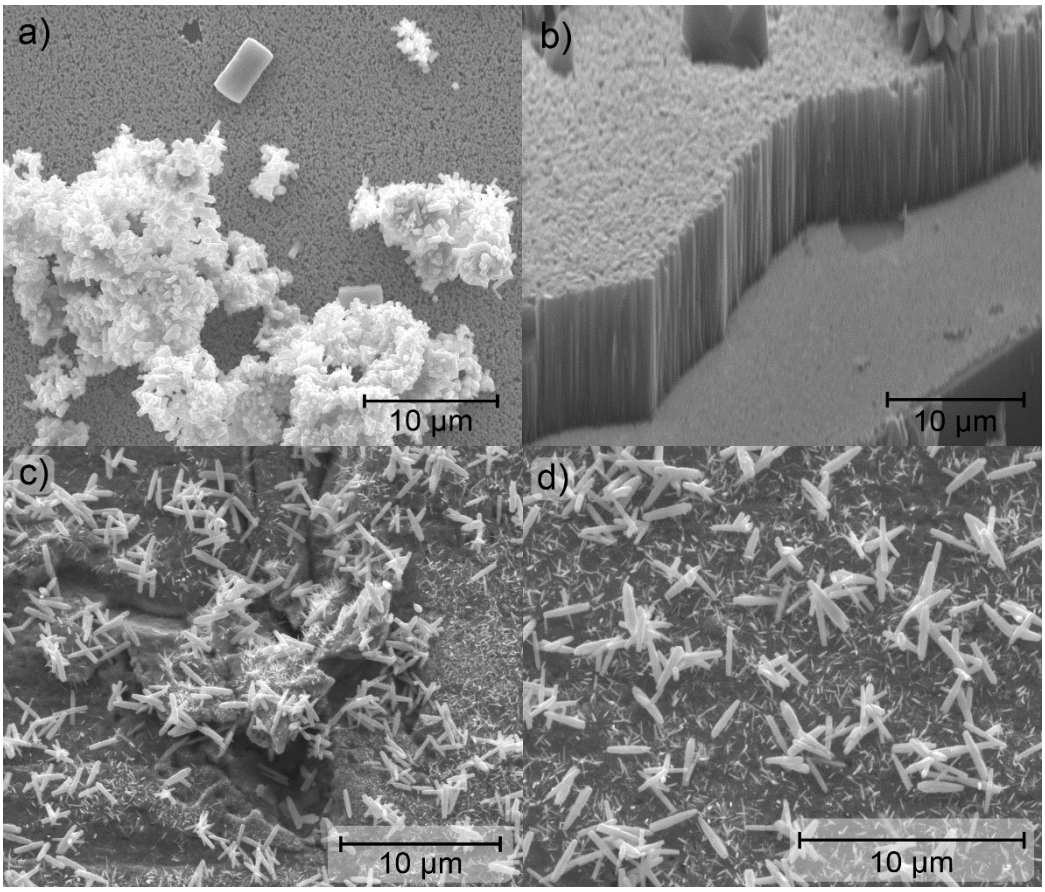

Figure 3.6. Scanning electron microscope images of ZnO nanorods grown on (a), (b) silver-coated Si wafer, and (c), (d) brass-coated Cu surface.

Equimolar solutions of (a), (b) 0.05 M, and (c), (d) 5.0 mM $Zn(NO_3)_2$ and hexamine were used as the growth solution. Nanorods grown at (a), (b) 60 °C for 3 hours, and (c), (d) 70 °C for 2 hours. (a) Top view of sample surface showing large clusters of ZnO nanorods on top of a well-aligned ZnO nanorod layer. (b) Tilted view of the edge of the sample surface showing a densely packed layer made up of tall, thin, highly-aligned ZnO nanorods. (c), (d) Randomly oriented ZnO nanorods grown on a rough brass substrate. Two different sizes are seen: large ZnO nanorods appearing to lie on top with shorter, thinner, nanorods that may have grown directly on the substrate.

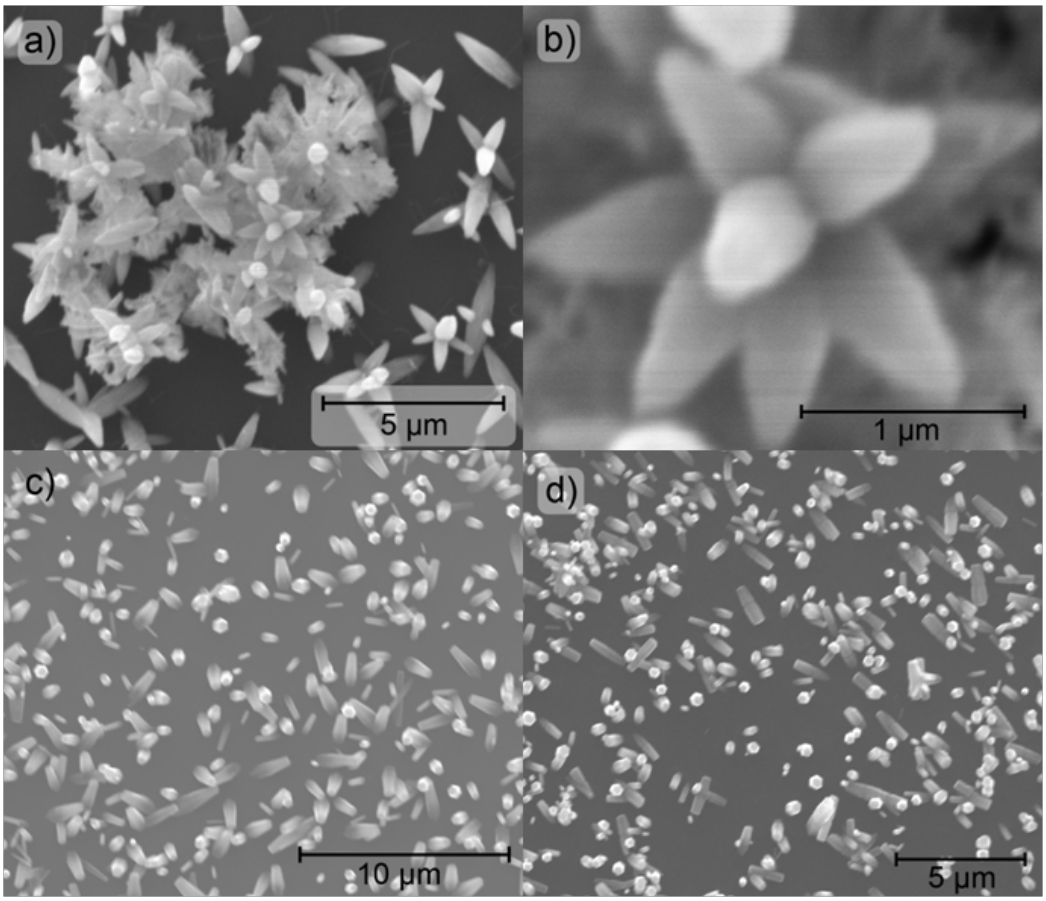

Figure 3.7. Scanning electron microscope images of ZnO nanorods grown on (a), (b) Si wafer, and (c), (d) nickel-coated Si wafer.

Equimolar solutions of (a), (b) 0.5 mM, (c), (d) 0.05 M $Zn(NO_3)_2$ and hexamine were used as the growth solution with (a), (b) 80 mM NH4OH, (c), (d) ammonia. Nanorods grown at (a), (b) 75 °C for 5 hours, (c), (d) 60 °C for 3 hours. (a) Nanoneedles grown in clusters on a Si wafer. (b) Magnified view of (a) showing a 'nano-flower' of ZnO nanoneedles. (c), (d) ZnO nanorods on a (c) Ni, (d) Si substrate showing a lower-density coverage than on other samples.

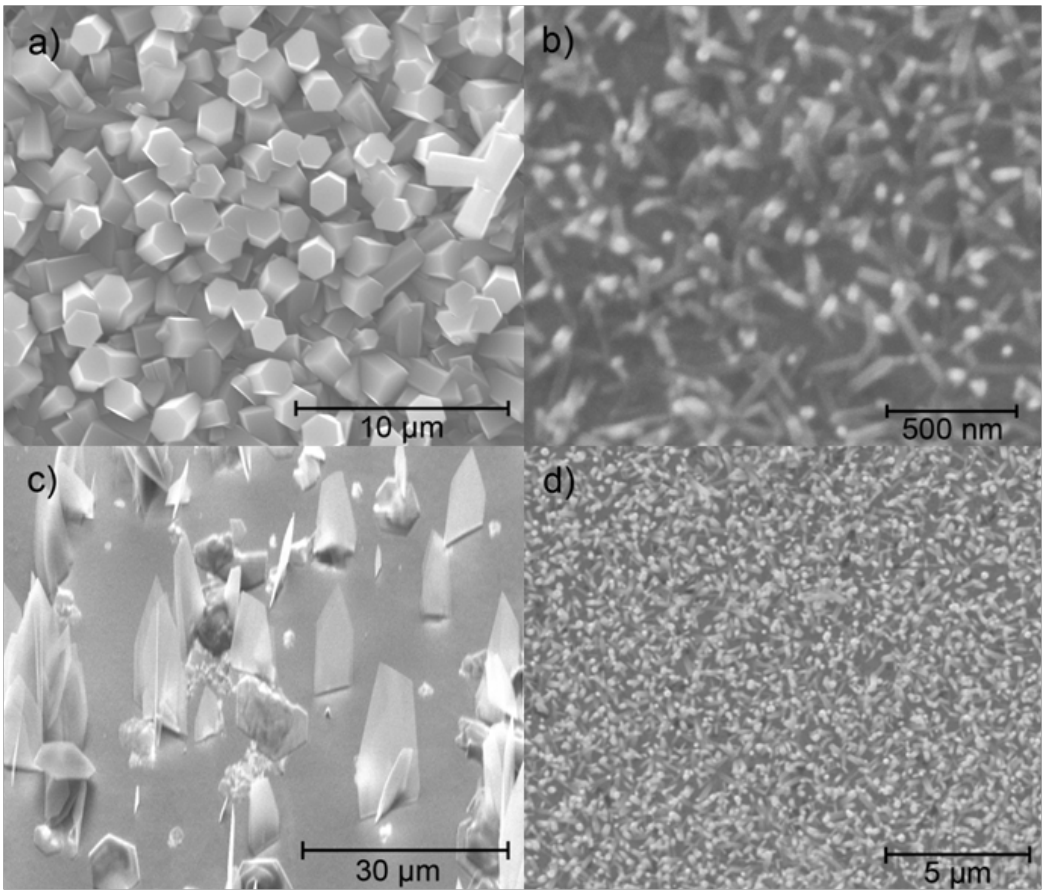

Figure 3.8. Scanning electron microscope images of ZnO nanorods grown on a silver-coated Si wafer.

Equimolar solutions of 0.05 M Zn^{2+} and hexamine were used as the growth solution. Nanorods were grown at 60 °C for 3 hours. (a) Thick (~1.7 µm), densely-packed ZnO nanorods grown using $Zn(CH_3COO)_2$. (b) Thin (~50 nm) ZnO nanowires grown using $ZnCl_2$. (c) Thin nanosheets grown using $ZnSO_4$. (d) Large uniform area of well-aligned ZnO nanorods grown using $Zn(NO_3)_2$.

3.3 Field Emission Properties

FE is the tunneling of electrons from the conduction band to the vacuum level under a high electric field. Its explanation by Fowler and Nordheim in 1928 was one of

the first successful applications of quantum mechanics [73]. In a typical experiment, the sample is placed in a vacuum chamber and an anode is positioned a distance from the sample. A voltage is applied between the anode and sample, and the resulting current measured. The FE current, *I*, versus anode-sample voltage, *V*, is described by the Fowler-Nordheim (FN) equation:

$$I = AV^2 exp\left(\frac{-b\varphi^{3/2}}{\beta V}\right)$$

where *I* is the current, *A* and *b* are positive constants, φ is the work function and *β* the geometric field enhancement factor [73]. ZnO nanorods can have *β* as high as 2 x 10^6 [3] due to their nanometer-scale features, although values of *β* for ZnO nanorods and carbon nanotubes are typically on the order of 1000. The large value of *β* results in significant FE at low applied fields on the order of volts per micron. The turn-on voltage and turn-on field for FE are defined as those values that produce a certain threshold current or current density. In addition to φ and *β*, the turn-on voltage and turn-on field depend on anode geometry, anode-sample distance, and location on the sample [74]. *I* versus *V* (*I*-*V*) data are typically plotted ln (I/V^2) versus $1/V$ to allow comparison with the straight-line behavior predicted for FE by the FN equation. We refer to such plots as FN curves. The slope of a FN curve is proportional to $\varphi^{3/2}/\beta$. Thus, changes in slope of a FN curve after prolonged operation or exposure to gases are due to changes in φ, *β* or both.

FE from ZnO nanostructures was first reported by Lee *et al* [1], who used vertically well-aligned ZnO nanorods grown using the VLS technique with Co nanoparticles at 550 ^oC. The FE measurements were carried out in a vacuum chamber at 2 x 10^{-7} Torr using

a flat anode having an area of approximately 30 mm^2 and placed approximately 250 μm from the sample. A stable FE current with a turn-on field of about 6 V/μm at a current density of 0.1 $\mu A/cm^2$ was measured. Increasing the field to 11 V/μm increased the current density to 1 mA/cm^2. These values were not as good as those of carbon nanotubes that had turn-on fields of around 1 V/μm at a current density of 90 $\mu A/cm^2$. However, subsequent investigations on ZnO nanorods reported that by reducing the rod diameter and tip radius, improving the vertical alignment and selecting the optimum areal density, the FE properties of ZnO nanorods could be improved to equal those of carbon nanotubes [2-11]. These reports investigated ZnO nanowires several tens of micrometers in length grown on W tips [2], ZnO nanoneedles having diameters of only several nanometers [3-5], ZnO nanopins [6], ZnO nanowires having different areal densities on planar substrates [7,8], tetrapod-like ZnO nanostructures [9], and ZnO nanorod arrays with different morphologies [10,11].

The effects of residual gases on the FE properties of ZnO nanostructures have not been extensively studied. Kim *et al* [13] reported the effects of O_2, N_2, Ar, air and H_2 exposure on the FE properties of ZnO nanorods grown using thermal evaporation of ZnO and graphite powders, and Co nanoparticles on a Si substrate.The vacuum chamber was at a base pressure of 2×10^{-5} Torr and gases were introduced to a pressure of 2×10^{-4} Torr. The anode-sample distance was 200 μm, and the anode consisted of a W plate having an unspecified area. They reported that O_2, N_2, Ar and air exposure degraded the FE properties, but there was full recovery of the FE properties after about 20 min of having evacuated the chamber to base pressure. They also found that H_2 exposure improved the FE properties and the improvement continued after evacuating to base pressure. In

Ref. [13], the data included the FE current as a function of time for the period covering the gas exposure and evacuation. However, FN curves before and after each exposure were not presented. Jang *et al* [14] also reported enhanced FE from ZnO nanowires by hydrogen gas exposure. Yeong *et al* [15] reported the effects of O_2 and H_2 exposure and UV illumination on the FE properties of individual ZnO nanowires grown on electrochemically sharpened Pt tips using evaporation and oxidation of Zn. The nanowires had lengths of a few microns. The chamber was at a base pressure of ~ 10^{-9} Torr and gases were introduced to a pressure of 7.5 x 10^{-7} Torr for 5 min. They found that initially O_2 exposure caused an increase in turn-on voltage of about 20%; however, the turn-on voltage returned to its original value after continued operation at base pressure. Upon additional exposure to O_2 the turn-on voltage permanently increased by 10% and did not return to its original value after operation at base pressure. They found that H_2 exposure caused a permanent reduction in the turn-on voltage of about 15%. They attributed their observations to the ionosorption of oxygen and hydrogen that created a doubly-charged layer on the surface whose field extended throughout the nanowire. This changed the carrier concentration and induced band bending. They also found that UV illumination increased the FE current by up to 2 orders of magnitude.

3.4 Effects of Residual Gas Exposure on the Field Emission Properties of ZnO Nanorods[†]

The field emission (FE) properties of ZnO nanorods have recently attracted

[†]This section is duplicated with permission of the publisher from published paper “Effects of Residual Gas Exposure on the Field Emission Properties of ZnO Nanorods”, Journal of Nanoscience and Nonotechnology, Vol.11,1-5,2011, Copyright © 2011 American Scientific Publishers. Note: Reference and figure numbers are changed to accommodate this dissertation.

considerable interest due to potential applications in FE displays and other cold cathode applications [11,62,120]. Carbon nanotubes and Mo metal microtips have been extensively studied for FE applications due to their excellent FE properties [25,121-124]. However, the FE properties of carbon nanotubes and metal microtips significantly degrade as a result of exposure to residual O_2 and oxygen-containing gases found in vacuum containers of displays [25,121-124]. The degradation is thought to be due to oxidation under high-electric-field conditions present during FE [124-126]. It is thought that ZnO and other oxide-based nanorods may not be as susceptible to degradation by O_2 and oxygen-containing gases since they are oxides [127]. To our knowledge, a detailed study of the effects of residual gases on the FE properties of ZnO nanorods is lacking [13,15]. Although many papers have focused on improving the field emission properties of ZnO nanorods [11,62,120], in this paper, we focus on the effects of residual gases on the field emission properties of ZnO nanorods. Our studies are performed in a gas environment similar to that in a real field emission device. Specifically, we compare the effects of O_2, CO_2, N_2, H_2, and Ar exposures on the FE properties of ZnO nanorods. In contrast to carbon nanotubes and metal microtips, we find that the FE properties of ZnO nanorods are not significantly degraded by O_2 and CO_2 exposures. However, the FE properties of ZnO nanorods are significantly degraded by N_2 exposure. We propose that this is due to the higher reactivity of nitrogen with ZnO. H_2 and Ar exposures are not observed to significantly degrade the FE properties.

The ZnO nanorods were synthesized using the DC arc discharge method with a Zn target, air at a pressure of 610 Torr and arc current of 30 A [72]. A scanning electron microscopy image (SEM) of the nanorods on a silver (Ag) coated Si surface is shown in

Figure 3.9 (a). An SEM image of the nanorods after FE under N_2 exposure is shown in Figure 3.9 (b). In Figure 3.9 (a), we observe nanorods of high aspect ratios measuring approximately 50 nm in width and 400 nm in length. There are many other larger ZnO particles with edges and rounded morphologies. The different morphologies are due to

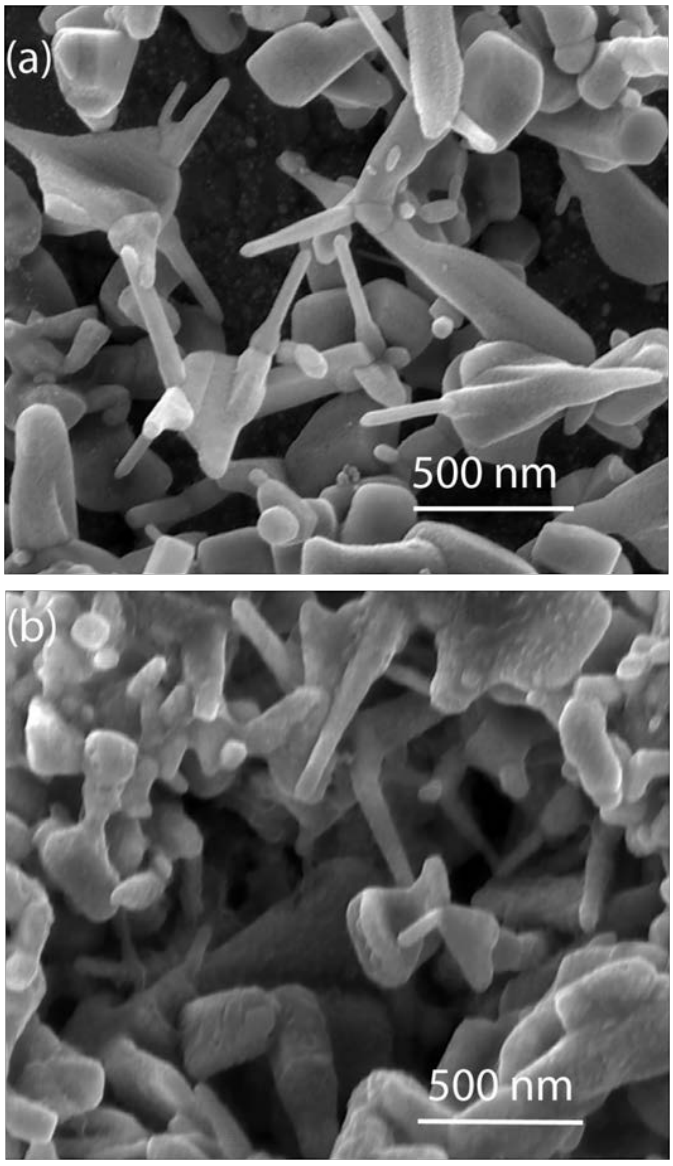

Figure 3.9. (a) Scanning electron microscopy image of the ZnO nanorods on the Ag coated Si surface. (b) Scanning electron microscopy image of the ZnO nanorods on the Ag coated Si surface after field emission under N_2 exposure. Scale denotes 500 nm.

the difference in supersaturation at the vapor-solid interface at high temperatures under air atmosphere [72]. All the particles were found to be highly crystalline using x-ray diffraction [72]. Approximately 20% of the particles displayed high aspect ratios. We expect FE to occur mainly at the apex of the high aspect ratio particles and the sharp crystallographic edges of larger particles.

The nanorods are *n*-type due to donor formation by oxygen vacancies and contain 80 ppm nitrogen impurities [72]. A mixture consisting of 1 mg of ZnO nanorods in 20 ml of ethanol was dispersed using ultrasonication for 1 hour. The mixture was deposited onto a silver coated Si substrate and allowed to dry. The thickness of the ZnO nanorod layer was approximately 1 μm.

The FE current, *I*, versus anode-sample voltage, *V*, is described by the Fowler-Nordheim (FN) equation:

$$I = AV^2 \exp\left(\frac{-b\varphi^{3/2}}{\beta V}\right) ,$$

where *A* and *b* are positive constants, φ is the work function, and β the geometric field enhancement factor [73]. The enhancement factor β is defined as $E_{local} = \beta E$, where E_{local} is the local electric field near the nanostructure and *E* is the macroscopic electric field between the anode and cathode [127]. We measured *I* versus *V* with the sample in a vacuum chamber at a base pressure < 10^{-9} Torr. The chamber was baked at 100 ^{o}C for 72 hours while being pumped using an ion pump. Residual gas analysis indicates that the main residual gases were H_2 at a partial pressure < 8 x 10^{-10} Torr and H_2O at a partial pressure of < 2 x 10^{-10} Torr. A schematic of the system used to measure the *I*-*V* curves is

shown in Figure 3.10. The tip was brought to the sample surface by a piezoelectric inchworm motor made by Burleigh Inc. [76] that was controlled by computer. The inchworm motor can move in steps as small as 2 nm/s. After the sample was loaded with the tip far from the sample surface, the inchworm motor was switched to a high speed. A camera and microscope were employed to observe the distance between the sample and the tip. To avoid touching the sample surface with the tip, the speed was slowed to about 120 nm/s when the tip-sample distance was about 100-200 μm. While at low speed, we applied a voltage of about 10 volts between the tip and the sample. We simultaneously monitored the current between the sample and tip with a picoammeter. The tip was controlled to stop at approximately 0.5 μm from the surface by optical inspection using the microscope. The picoammeter was monitored to make sure there was no tip-sample contact during the approach.

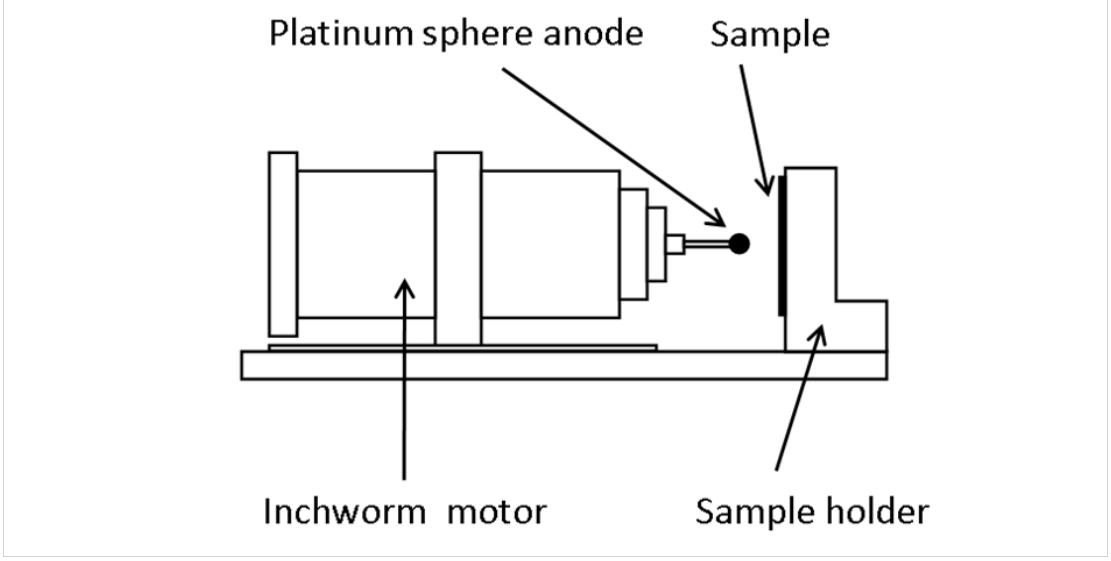

Figure 3.10. Schematic of the system used to measure the field emission current versus voltage curves consisting of a spherical platinum anode approximately 1 mm in diameter positioned 25 μm from the sample using an inchworm motor.

We considered this as the point of origin when measuring the tip-sample distance. The tip was then retracted from the origin with the inchworm motor to a specified distance from the sample at a rate of 0.12 μm/s.

The FE current was collected from a localized region of the sample using a spherical platinum anode having a diameter of approximately 1.0 mm (see in Figure 3.10). We used a spherical anode instead of a planar anode to avoid problems that are known to occur with planar anodes: non-uniform anode-sample distance due to non-parallel alignment of the anode and sample, and anode edge effects [74]. Ref. [74] gives a method for calculating the effective FE area in our experiment. Using this method, we calculate an emission area of approximately $5x10^{-3}$ mm^2. Using the inchworm motor as described above, the anode was positioned 25.0 ± 0.5 μm from the sample surface to simulate typical distances between emitter and anode in device structures [77]. Low FE currents of approximately 20-2000 pA were used to avoid heating of the ZnO nanorods. These correspond to current densities within the range 0.4–40 $\mu A/cm^2$ that are at most about an order of magnitude less than the current densities of 300 $\mu A/cm^2$ that have been reported to produce heat-induced damage in ZnO nanorods [129]. In order to obtain a stable field emission current, we initially cleaned and conditioned the ZnO nanorods by applying a tip voltage of 650 V in a vacuum of 10^{-9} Torr and at a tip-sample distance of 25 μm for 30 minutes. This resulted in a FE current of about 10-100 pA.

In Figure 3.11-3.15, we show the collected data plotted as ln (I/V^2) versus $1/V$. This is done to allow comparison with the straight-line behavior for FE predicted by the FN equation. The positive slope of the FN curves at low voltages is due to a small leakage current across the connectors on the order of 0.1 pA. At high voltages, the curves show

a negative slope, in agreement with the FN equation. We define the turn-on voltage for FE as the smallest voltage at which the FE current is observed above the leakage current. The insets in Figure 3.11-3.15 are the corresponding *I-V* curves plotted using a log-linear scale after subtraction of the leakage current. Immediately after the initial cleaning process and right before exposure to the gases, the *I-V* curves are measured as shown by the solid squares in Figure 3.11-3.15. To achieve 65 L of exposure (1 L = 10^{-6} Torr·s), gas is introduced at a pressure of 3 x 10^{-7} Torr for 216 s while the sample is biased to produce approximately 20 pA of FE current. The vacuum chamber is then evacuated to

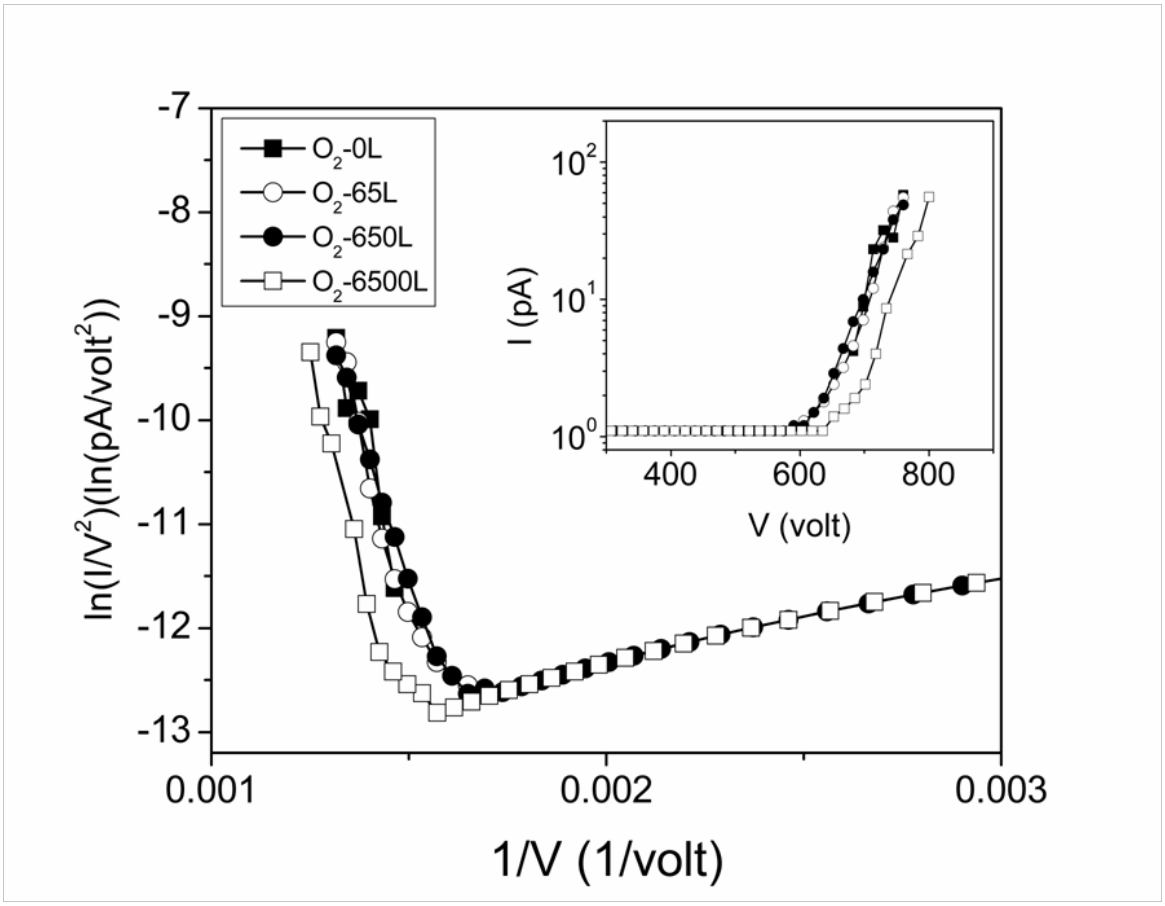

Figure 3.11. Field emission versus voltage data for the ZnO nanorods after 0 L, 65 L, 650 L and 6,500 L of O_2 exposure at 3 x 10^{-7} Torr.

< 10^{-9} Torr and the FE *I–V* curves are measured, as shown by the open circles. In this manner, the nanorods are not exposed to gases during the *I-V* curve measurement. To achieve 650 L and 6,500 L of exposure, the procedure described above is repeated for 2,160 s and 21,600 s, respectively. For each set of gas exposures, the anode is positioned over a different area of the sample. The difference in the turn-on voltages for different gases is attributed to variations in nanorod morphology with different sample area.

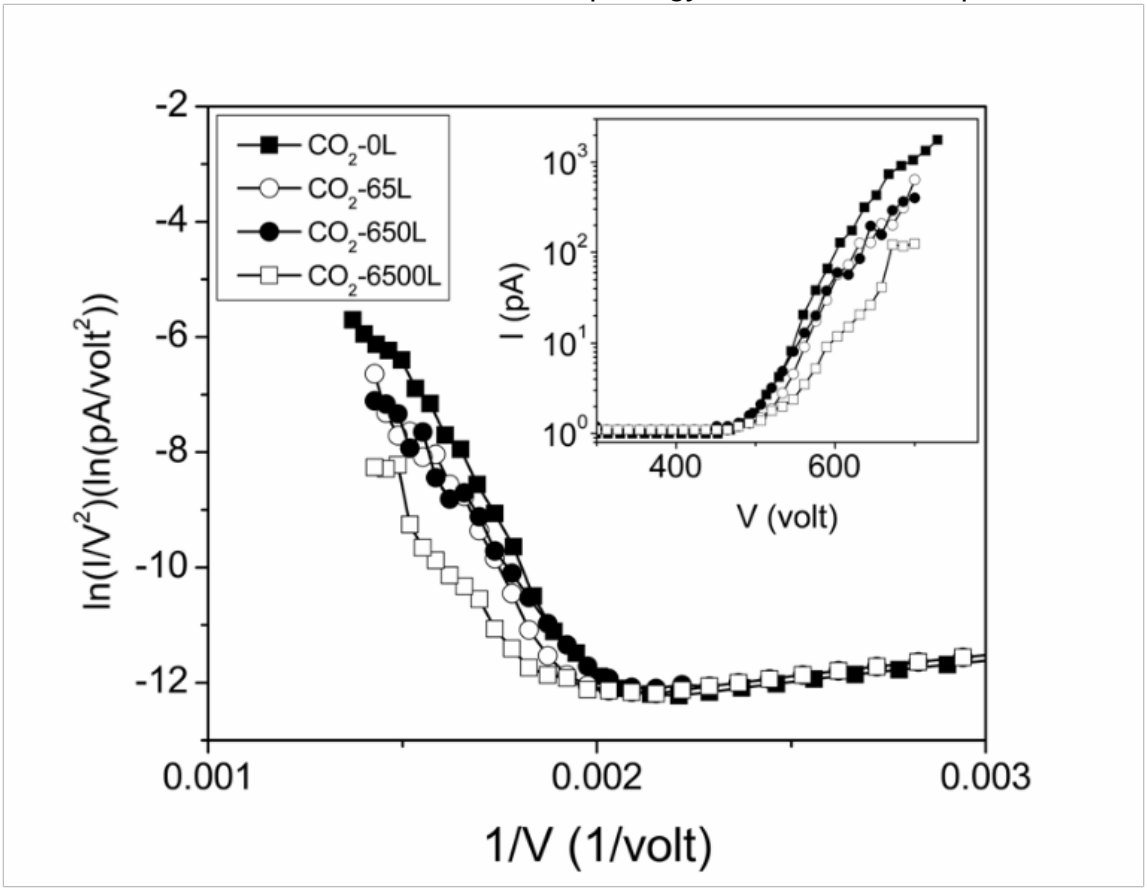

Figure 3.12. Field emission versus voltage data for the ZnO nanorods after 0 L, 65 L, 650 L and 6,500 L of CO_2 exposure at 3 x 10^{-7} Torr.

As shown in Figure 3.11, O_2 exposure does not have a significant effect on the FE properties of ZnO nanorods. After 65 L and 650 L of O_2 exposure, the turn-on voltage

decreases slightly from approximately 640 V to 610 V, while the FE current at higher voltages remains approximately the same. After 6,500 L of O_2 exposure, the turn-on voltage returns to its initial value of 640 V prior to exposure, and the FE current decreases slightly from 60 to 20 pA at 760 V.

As shown in Figure 3.12, CO_2 exposure also does not have a significant effect on the FE properties. After 65 L and 650 L of CO_2 exposure, the turn-on voltage remains approximately the same, and the FE current decreases slightly from about 70 to 50 pA at 690 V. After 6,500 L of exposure, the turn-on voltage increases slightly from approximately

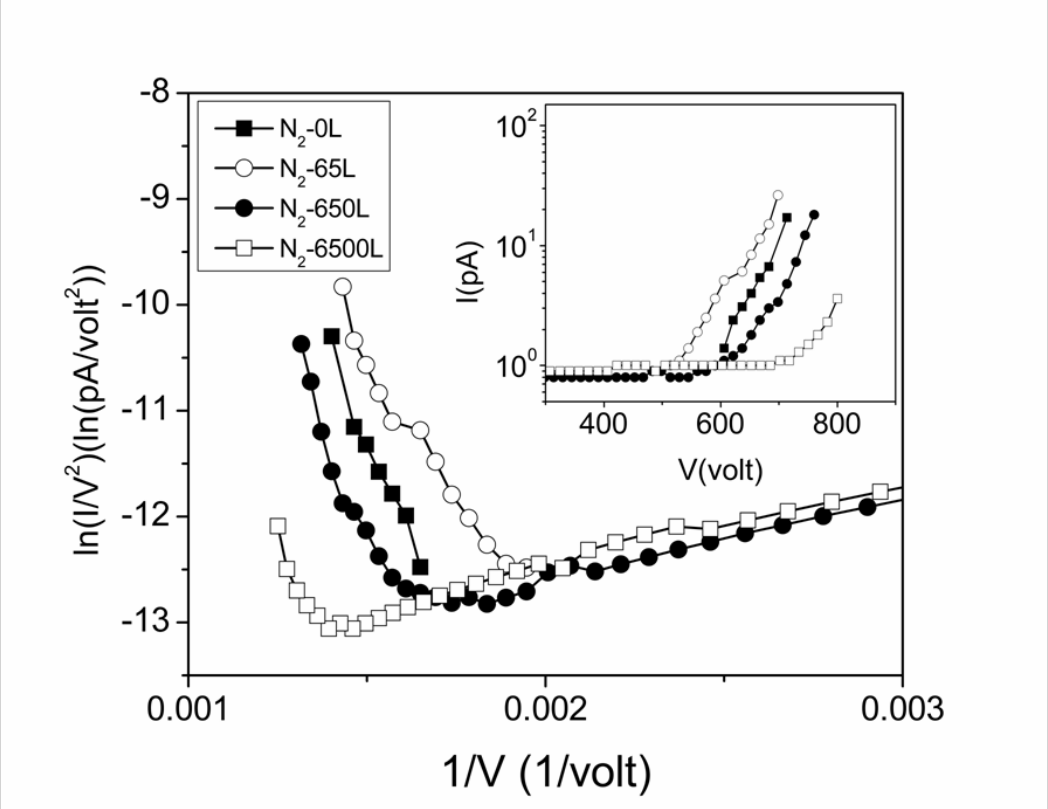

Figure 3.13. Field emission versus voltage data for the ZnO nanorods after 0 L, 65 L, 650 L and 6,500 L of N_2 exposure at 3 x 10^{-7} Torr.

500 to 530 V, and the FE current decreases from around 70 to 10 pA at 690 V. By contrast, the FE properties of carbon nanotubes and Mo microtips are significantly degraded by exposure to O_2 and oxygen containing gases such as CO_2 [120].

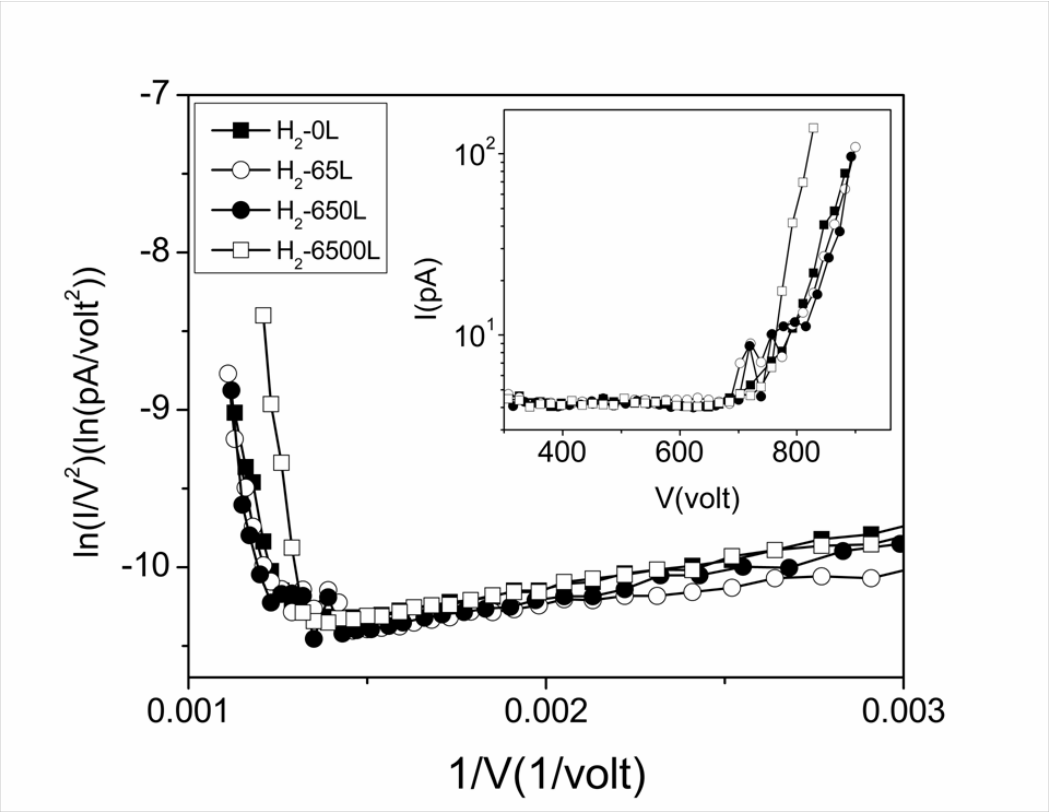

Figure 3.14. Field emission versus voltage data for the ZnO nanorods after 0 L, 65 L, 650 L and 6,500 L of H_2 exposure at 3 x 10^{-7} Torr.

As shown in Figure 3.13, N_2 exposure results in significant degradation of the FE properties. Initially, after 65 L of N_2 exposure, the FE properties improve slightly. The turn-on voltage decreases from approximately 580 to 520 V, and the FE current increases slightly from approximately 7 to 15 pA at 680 V. Adsorbates have been reported to degrade the FE properties of nanostructures such as carbon nanotubes and Mo microtips by increasing the work function. Initial exposure to gases has been shown to improve the FE properties by cleaning [25,121-125]. However, after 650 L of N_2 exposure, the turn-on

voltage increases to 590 V, and the FE current decreases from 20 to 4 pA at 700 V. After 6,500 L of N_2 exposure, the turn-on voltage increases significantly to 740 V, and the FE current at 700 V decreases from 20 pA to below the level of the leakage current. In contrast, the FE properties of carbon nanotubes and Mo microtips are not significantly degraded by exposure to N_2.

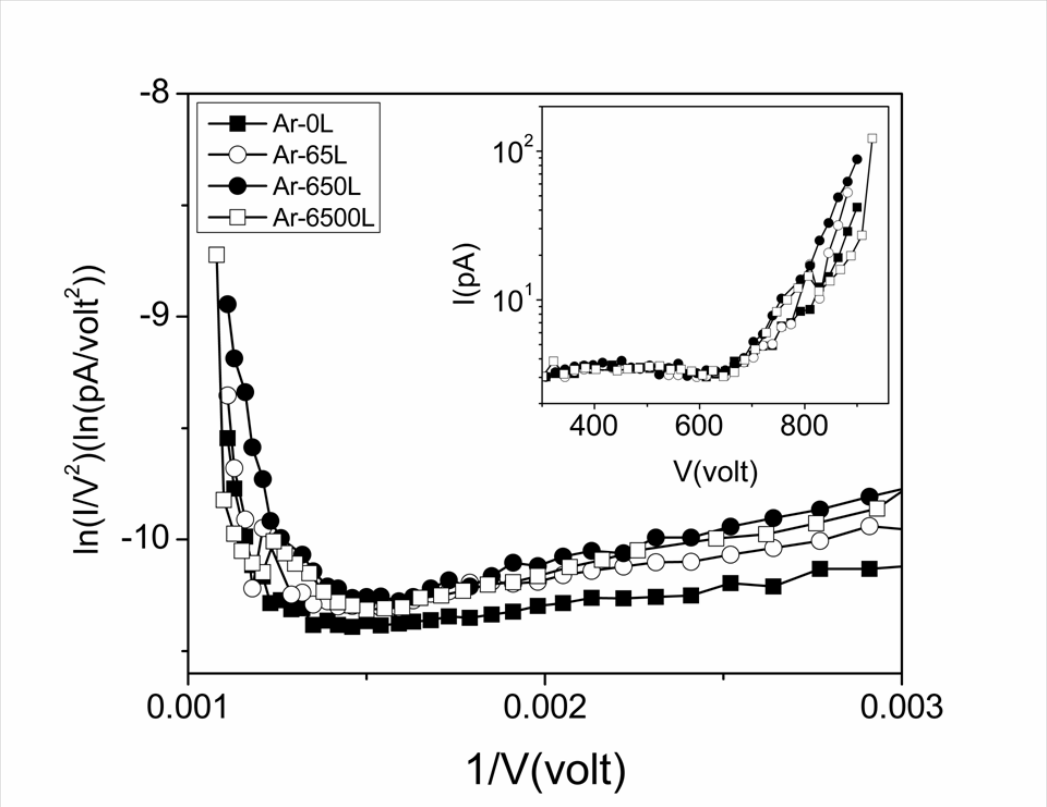

Figure 3.15. Field emission versus voltage data for the ZnO nanorods after 0 L, 65 L, 650 L and 6,500 L of Ar exposure at 3 x 10^{-7} Torr.

As shown in Figure 3.14, 65 L and 650 L of H_2 exposure does not have a significant effect on the turn-on voltage or FE current of ZnO nanorods. After 6,500 L of H_2 exposure, the FE current at higher voltages increases from approximately 20 to 200

pA at 830 V. Prolonged H_2 exposure has been reported to significantly improve the FE properties of Mo microtips [121,125] and diamond-coated microtips [78,79] due to surface cleaning. We propose that surface cleaning is responsible for the increase in the FE current we observe after H_2 exposure. As shown in Figure 3.15, Ar exposure does not have a significant effect on the FE properties. After 650 L of Ar exposure, the turn-on voltage decreases slightly from approximately 750 V to 705 V, and the FE current increases from 44 to 80 pA at 885 V. After 6,500 L of Ar exposure, the turn-on voltage and FE current are approximately the same as before exposure.

We propose that O_2 and CO_2 exposures do not have a significant effect on the FE properties of ZnO nanorods because O_2 and other oxygen-containing species present under high-field conditions do not significantly react with ZnO due to the difficulty of further oxidation. It has been reported that the morphology of ZnO films is improved when the films are exposed to oxygen plasma due to a decrease in the number of oxygen vacancies [74]. This results in an increase in conductivity. With regard to our observations under nitrogen gas exposure, we have concluded on the basis of Ref. [130] that the high-field conditions present under FE provide a sufficient electric field to allow the formation of atomic nitrogen. In Ref. [130], the field between the electrodes was about 5×10^6 $V \cdot m^{-1}$. These conditions allowed for the production of atomic and ionic nitrogen species. Table 1 shows the ionization energies of all the gases used. This serves as an indicator of the ease/difficulty of ionization of the gases. Atomic nitrogen has been reported to modify structurally and morphologically the crystalline lattice of ZnO by substitution of oxygen by nitrogen [81,82]. The FE properties of nanostructures such as ZnO are significantly improved as a result of an increase in the aspect ratio of the nanostructures that increases

the geometric enhancement factor β to values as high as β = 1173 [131] and β = 5583 [128,132] for ZnO. In a typical FE experiment, the geometric enhancement factor β magnifies the electric field to values in the range 10^8-10^{10} V/m, orders of magnitude higher than the ionization threshold field for nitrogen dissociation reported in Ref. [128]. We propose that the atomic nitrogen reacts with ZnO and structurally damages the nanorods. Figure 3.9 (b) shows damage to the nanorods after FE under 6500 L of N_2 exposure. This damage may decrease the geometric field enhancement factor, β, and increase the turn-on voltage. In addition, because O has one more electron than N, the substitution of O by N would lead to a locally hole-rich region, which could increase the work function.

Table 1. Ionization energy of gases used

Gas	O	CO_2	N	H	Ar
Ionization Energy (ev)	13.61	13.77	14.53	13.59	15.75

Source: *Handbook of Chemistry and* Physics, Edited D.R Lide, 74th Edition, National Institute of Standards and Technology, (CRC Press, Ann Arbor 1994), p 205. [133].

In conclusion, we have measured the effects of O_2, CO_2, N_2, H_2, and Ar gases on the FE properties of ZnO nanorods. In contrast to carbon nanotubes and Mo microtips, O_2, and CO_2 gases do not have a significant effect on the FE properties of ZnO nanorods. However, N_2 is observed to significantly degrade the FE properties and we propose that this is due to the dissociation of N_2 into atomic nitrogen species which react with ZnO. H_2 and Ar exposure are not observed to significantly degrade the FE properties.

3.5 ZnS Nanostructures

Like ZnO, ZnS is a wide band gap semiconductor that has attracted considerable interest for its luminescent and electrical properties with applications in light emitting diodes [83], flat panel displays [84,85], transparent conductive coatings [86], and buffer layers in solar cells [87]. Numerous methods have been used in the preparation of ZnS thin films [87,88] and nanostructures [89-93], including thermal evaporation [89,90], RF sputtering [87], and solution-based growth processes [88,91,92]. ZnS nanostructures such as nanorods, nanowires, and nanobelts can be grown as single crystals with high aspect ratios and in good electrical contact with conducting metallic substrates making them ideal candidates for FE experiments [89,91].

Vapor phase deposition processes, such as thermal evaporation, rely on heating ZnS at high temperatures inside a deposition chamber under an inert atmosphere (Ar or N_2) containing small amounts of reducing gasses (H_2 or CO) [89,90]. The ZnS nanostructures form from the vaporized precursor material through the VLS and VS growth modes with a uniform distribution across the substrate surface. Electron microscopy, however, reveals a randomly oriented arrangement, unlike the well-aligned structure of ZnO nanorods produced through a similar growth process, which is less desirable for FE due to lower geometric field enhancement factors [84,89]. Although vapor deposition techniques are commonly used to produce high quality ZnS nanostructures, these methods possess several distinct disadvantages making them undesirable for large scale adoption. Such deposition methods can involve corrosive and highly toxic hydrogen sulfide gas [84,87] as well as require vacuum systems and often employ high growth temperatures in excess of 1000 °C [89,90], which limit the choice of substrates suitable

for deposition. Additionally, high temperature deposition of ZnS requires a thorough exclusion of O_2 gas from the growth environment due to the ease at which ZnS is converted to ZnO with even minor traces of O_2 present [90].

As an alternative to vapor deposition, high quality ZnS thin films and nanostructures may instead be grown through aqueous solution-based processes [88,91-93]. Aqueous solution growth of ZnS nanostructures is a straightforward, low temperature process that uses relatively safe and inexpensive precursor materials and does not require specialized equipment, unlike thermal vapor deposition. Using a water-soluble zinc salt, such as $ZnCl_2$, $ZnSO_4$, or $Zn(CH_3COO)_2$, and a sulfide ion source, such as thiourea ($CS(NH_2)_2$) or Na_2S, ZnS nanostructures may be grown in a variety of forms. Under alkaline conditions, thiourea decomposes in solution to give off bisulfide ions, SH^-, which in turn react to form sulfide ions via the following reactions [88],

$$CS(NH_2)_2 + OH^- \rightarrow SH^- + CH_2N_2 + H_2O$$
$$SH^- + OH^- \leftrightarrow S^{2-} + H_2O$$

The Zn^{2+} and S^{2-} ions present in the solution precipitate out as ZnS. Complexing agents may also be used, particularly in thin film deposition, in order to increase the amount of ZnS formed and promote a more heterogeneous deposition on the substrate surface, which results in the formation of smoother and more optically transparent film [88]. Ammonia is a common complexing agent for Zn^{2+} that can be used in combination with sodium citrate, which has been shown to increase the amount of ZnS deposited [88]. These complexing agents also have the added benefit of acting to raise the pH of the growth solution, which is necessary for sulfide ion formation.

Lu et al. report the large scale growth from aqueous solution of well-aligned ZnS nanobelts and their field emitting properties [91,94]. The nanobelts were synthesized from an aqueous growth solution prepared using a mixture of $Zn(CH_3COO)_2$, thiourea, and ethylenediamine (EDA), using NaOH to adjust the pH. A zinc foil substrate was immersed in the growth solution and sealed inside an autoclavable vial which was heated to 160 °C for 10 hours. During this initial growth phase a layer of $ZnS(EDA)_{0.5}$ is reported to be deposited on the zinc foil substrate. Following the growth of the $ZnS(EDA)_{0.5}$ layer, the substrate was washed in DI water and ethanol then dried under vacuum at 70 °C for 5 hours. The substrate was then heat-treated at 250 °C under vacuum for 30 minutes in order to decompose the $ZnS(EDA)_{0.5}$ into ZnS. Scanning electron microscopy reveals that ZnS prepared in this manner forms well-aligned, vertically oriented, nanobelts which can attain dimensions of approximately 30 nm thick, 300-500 nm wide, and several micrometers in length. The ZnS nanobelts exhibit a highly crystalline structure and grow uniformly over large areas. The zinc metal substrate was found to play a crucial role in the formation of nanobelts, acting as a secondary source of Zn^{2+} ions and providing a structurally compatible surface for ZnS growth. When using a silicon substrate instead of zinc, ZnS nanobelts have been shown to form as smaller and more disorganized nanoparticles which are formed in solution and deposited on the substrate surface. Additional factors which play an important role in growing ZnS nanobelts include the concentration of the zinc salt as well as the pH of the solution, with high aspect ratio, vertically aligned, nanobelts formed using a Zn^{2+} concentration of about 12.5 mM and a pH of 10. The ZnS nanobelts were found to have a low turn-on field of around 3.8 V/μm which is thought to be due to their geometric characteristics, such as their high aspect

ratio and sharp corners, resulting in calculated field enhancement factors of over 1800. The relative ease in which highly aligned ZnS nanobelts may be grown along with their excellent field emitting properties makes them a promising candidate for use in field emitting device applications.†

† An aqueous mixture of thiourea (CH_4N_2S), sodium citrate ($Na_3C_6H_5O_7$), and zinc salt (zinc sulfate primarily) were used to grow zinc sulfide. The pH was adjusted using a dilute ammonium hydroxide solution until the desired pH level was reached. Like the zinc oxide, growing temperatures for the zinc sulfide ranged from about 70 to 80 °C, but the growth time was shorter, usually only 1 or 2 hours. The concentrations of the zinc salt, thiourea, and sodium citrate in the growth solution were from 0.05 M to 0.5 mM.

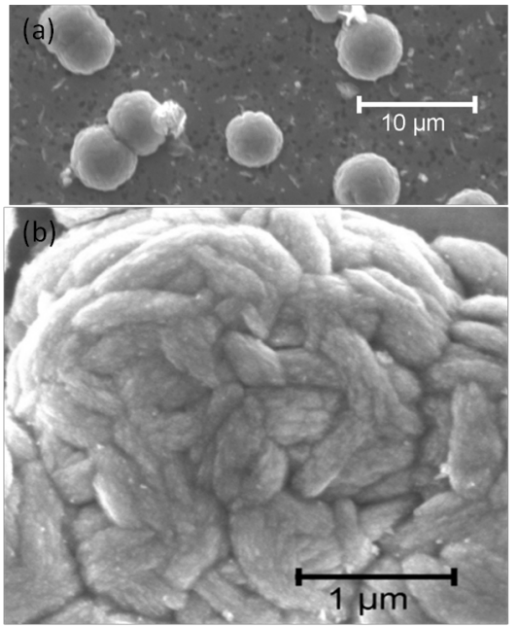

Figure 3.16. SEM images of ZnS shaped spheres (a) ZnS spheres on substrate and (b) A close view of ZnS sphere.

† Figures 3.16-3.22 and paragraphs in this section indicated with cross (†) are from work done with Jeffrey Schwartz in our lab, with REU (Research Experiences for Undergraduates summer program).

† Figure 3.16 is a scanning electron microscope image of zinc sulfide. Irregularly shaped spheres or bumps appear to cover much of the substrate surface. These spheres grew considerably larger than the ZnO nanorods, having a diameter of several micrometers as opposed to the diameters of some of the nanorods which were only a few hundred nanometers.

† We have investigated the effects of Ar, N2, H2, O2, CO2 and H2O on the FE properties of ZnS with the same method as for ZnO. The results show in Figure 3.17-21.

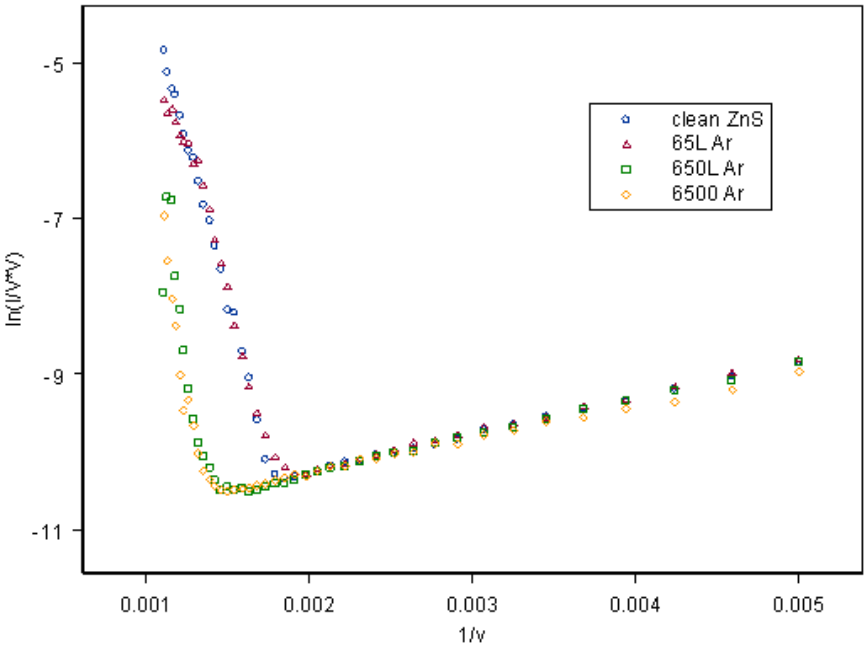

Figure 3.17. Fowler-Nordheim curves for the ZnS nanorods after exposures of 0 L, 65 L, 650 L and 6,500 L at 3 x 10^{-7} Torr of Ar.

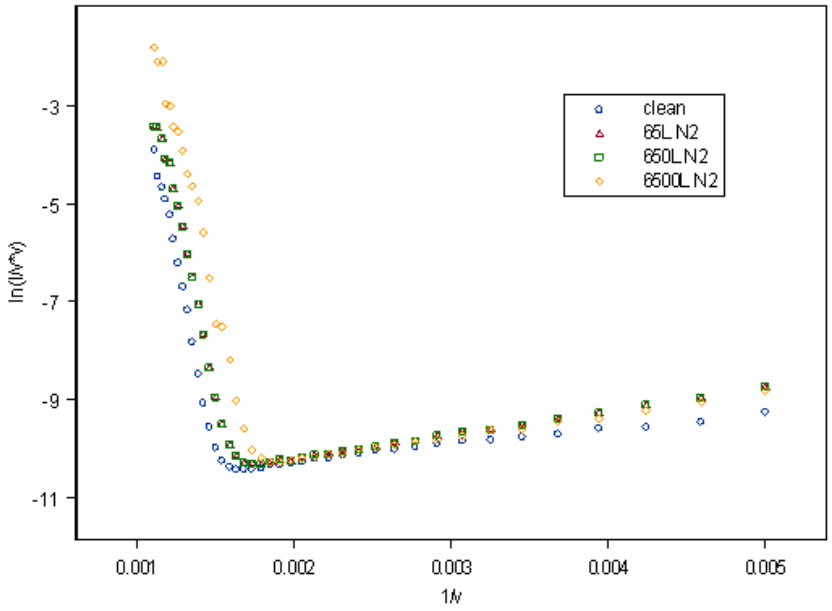

Figure 3.18. Fowler-Nordheim curves for the ZnS nanorods after exposures of 0 L, 65 L, 650 L and 6,500 L at 3 x 10^{-7} Torr of N_2.

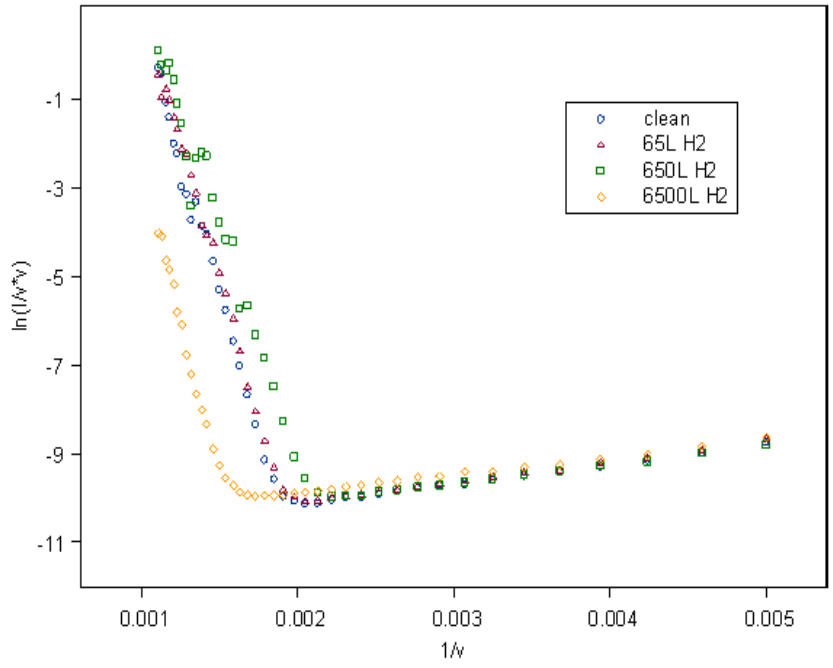

Figure 3.19. Fowler-Nordheim curves for the ZnS nanorods after exposures of 0 L, 65 650L and 6,500 L at 3 x 10^{-7} Torr of H_2.

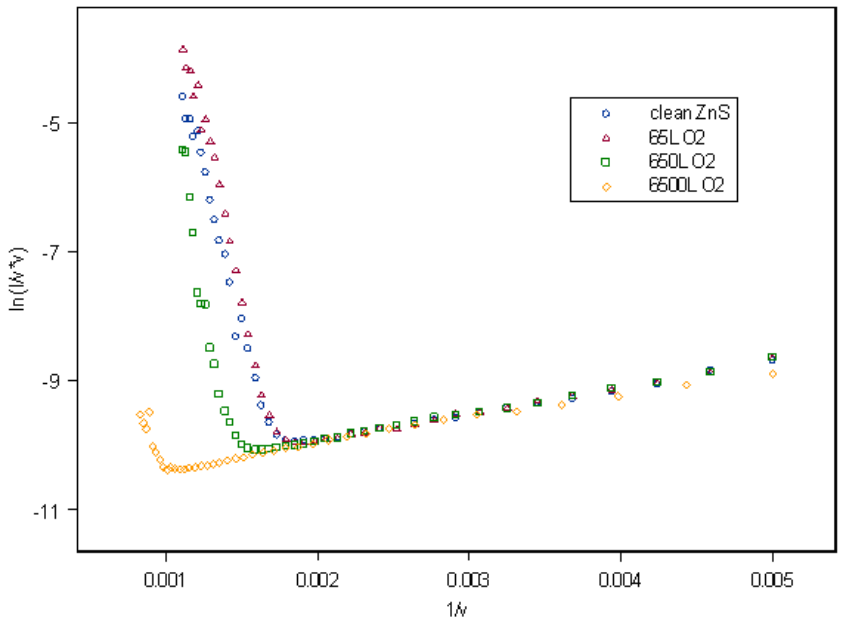

Figure 3.20. Fowler-Nordheim curves for the ZnS nanorods after exposures of 0 L, 65 650L and 6,500 L at 3 x 10-7 Torr of O_2.

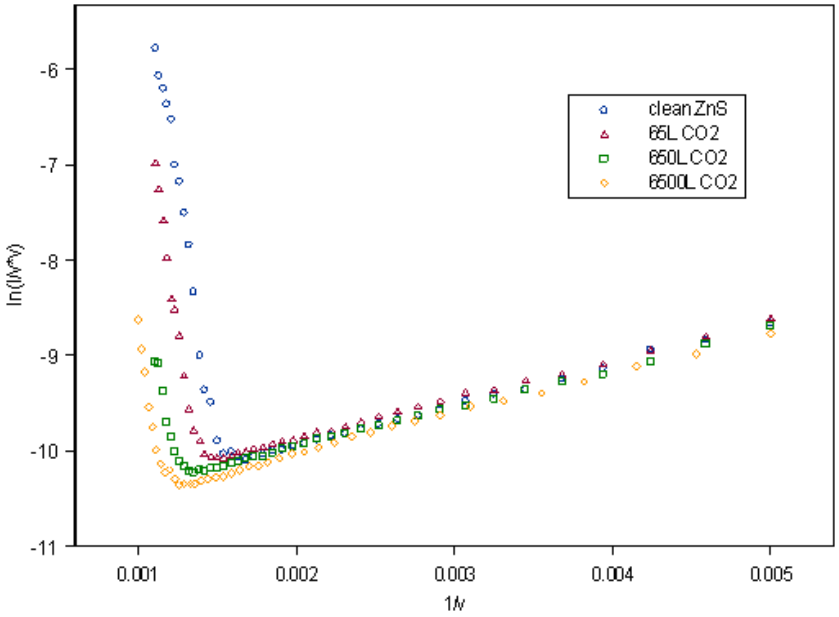

Figure 3.21. Fowler-Nordheim curves for the ZnS nanorods after exposures of 0 L, 65 L, 650 L and 6,500 L at 3 x 10-7 Torr of CO2.

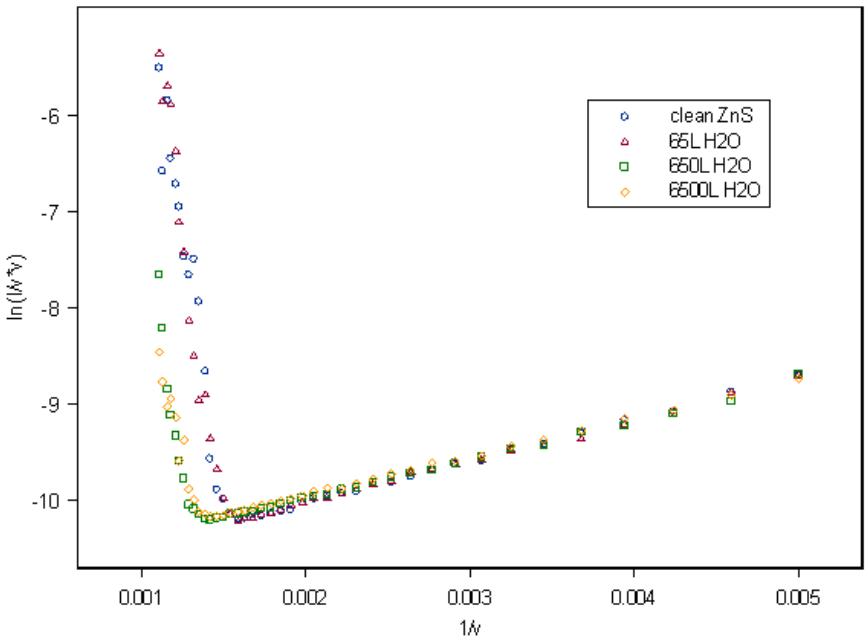

Figure 3.22. Fowler-Nordheim curves for the ZnS nanorods after exposures of 0 L, 65 L, 650 L and 6,500 L at 3 x 10^{-7} Torr of H_2O.

† It was found that Ar, CO_2, O_2, and water vapor degraded the field emission of the ZnS sample while N_2 showed a slight improvement. H_2 initially improved the field emission of the sample but then caused degradation upon longer exposure.

3.6 GaN Nanorods

Various nanostructures based on GaN can be produced using a number of methods depending on the form of the structure intended to be produced [95]. Such structures can take the form of nanorods, nonowires, nanofilms, hexagonal pyramids, and possibly other forms. Production could involve the use of PLD, CVD, epitaxial growth, and dc sputtering. Characterization of a given structure can involve methods such as X-ray diffraction, electron microscopy and other methods. GaN, having an electron affinity of

2.7–3.3 eV [96] and an electron effective mass of 0.2 times the mass of a free electron [97], is considered useful in the potential development of FE based devices. It also has very high physical and chemical stability, which, while making it a very durable medium, also makes the manipulation of the substance all the more difficult [96]. GaN is of technological interest due to its role in the operation of UV, blue, and green light emitting diodes, and blue lasers [98] as well as the potential development of thin screen monitors with brightness and efficiency attributes that are superior to liquid crystal display technology [99].

Of particular interest are GaN nanorods which have interesting crystal structures and FE properties. PLD has proven to be an effective method of producing GaN nanorods [100]. GaN nanorods produced using this method have a single crystalline hexagonal Wurzite structure, and have a diameter of 5-20 nm, and a length on the order of microns. Experiments have shown such GaN to have a turn-on voltage of 8.4 V/μm and a current density of 0.96 mA/cm^2 under an applied voltage of 10.8 V/μm measured under a pressure of 2×10^{-6} Torr.

Doped nanorods can also be produced using a simple VLS thermal evaporation process involving the use of GaN based powders (Ga_2O_3:GaN,Ga_2O_3:GaN) [101]. The powders are mixed in with a doping element such as phosphor, and applied to a Si (111) substrate with a 5 nm thick gold film. The combination is then placed in a quartz oven and heated to temperatures over 1000 ^oK. The resulting *p*-doped GaN nanorods, which can be characterized using x-ray diffraction and scanning electron microscopy, have a single crystal Wurzite structure with a diameter of 10-40 nm and a length on the order of tens of microns. Unlike non-doped GaN nanorods, they tend to have a rough, curved surface

structure that is responsible for the enhanced FE properties (reduced turn-on voltage) of the nanorods. The turn-on voltage for such nanorods depends on the amount of doping applied to the rods. Undoped nanorods have a turn-on voltage, under a pressure of 2 x 10^{-6} Torr, of 6.1–12.0 V/μm giving a current density of 0.01 mA/cm^2, while doped nanorods have a turn-on voltage of 5.1 V/μm with the same current density. In comparison, an alternative GaN structural format, namely thin film amorphous GaN, has been shown to have a turn-on voltage of 5 V/μm and a maximum current density of 500 mA/cm^2 [103].

Another nanorod format developed by a Japanese research group includes needle-like bicrystalline GaN which can serve as low cost, large area emitters [102]. These structures are manufactured on a 20 nm gold substrate, and have a sharp tip and bicrystalline structural defects, which is hypothesized to be the cause of its FE properties. The diameter of the nanorods is 200 nm up to a certain length at which point the diameter gradually decreases until it cuts off with a diameter of 10 nm giving the rods a pencil-like structure. The FE of the rods is performed using a rod-like tip with a 1 mm^2 cross section as an anode. The tip is separated from the sample at a distance of 125 μm, and the applied voltage has a range of 0 to 1000 V set at increments of 20 V at a pressure of 6 x 10^{-6} Torr. The turn-on voltage for the sample is 7.5 V/μm at a current density of 0.01 mA/cm^2.

In the previously described methods for the growth of GaN nanostructures, the mechanism of nanostructure formation is VLS [104]. For nanostructures to form, very thin metallic layers, which usually exist as tiny grains, were used as a catalyst to promote nucleation and growth of the nanostructure. Metal catalysts reduce melting-point due to alloying effect and seed nucleation and as the nanostructure growth commences, the

nano-droplets continue to stay atop, acting as the source for the continuing growth of the nanostructures.

Despite its effectiveness in fostering nanostructure formation, in VLS growth, traces of catalysts inevitably contaminate the growing material, hence altering its electronic band structure. Therefore, if one can replace such extrinsic seeding procedures with an intrinsic means, say by use of the same atomic constituents as a seed or through substrate surface morphology engineering, the impurity problems may be solved. Seo *et al* [105,106] introduced a concept of nano-capillary condensation suggesting that nanorods would nucleate on specific sites, and as islands on the substrate begin to impinge one another, Ga atoms would condense in the nano-valleys [105,106]. Such nano-capillaries thus exclude extrinsic catalysis in the traditional VLS mechanism based on foreign metallic elements. The nano-capillaries enable the nanorods to form in single directions, resulting in more manageable nanostructures for device applications.

Figure 3.23 illustrates the procedure of the nano-capillary condensation and the ensuing nanorod growth. The nucleation and growth process starts with three randomly chosen precursor nuclei on the vertices of an irregular triangle, as shown in Fig.10 (a). Consequently, a voided region of equilateral triangle would develop as illustrated in Fig. 10(b) when the islands encounter each other. The voided triangular areas are thermodynamically unstable so that a transformation would take place to reduce the urface energy by corner filling via some self-regulated surface diffusion along the edges. This eventually results in a hexagonal nanotrench, as sketched in Fig. 10(c).

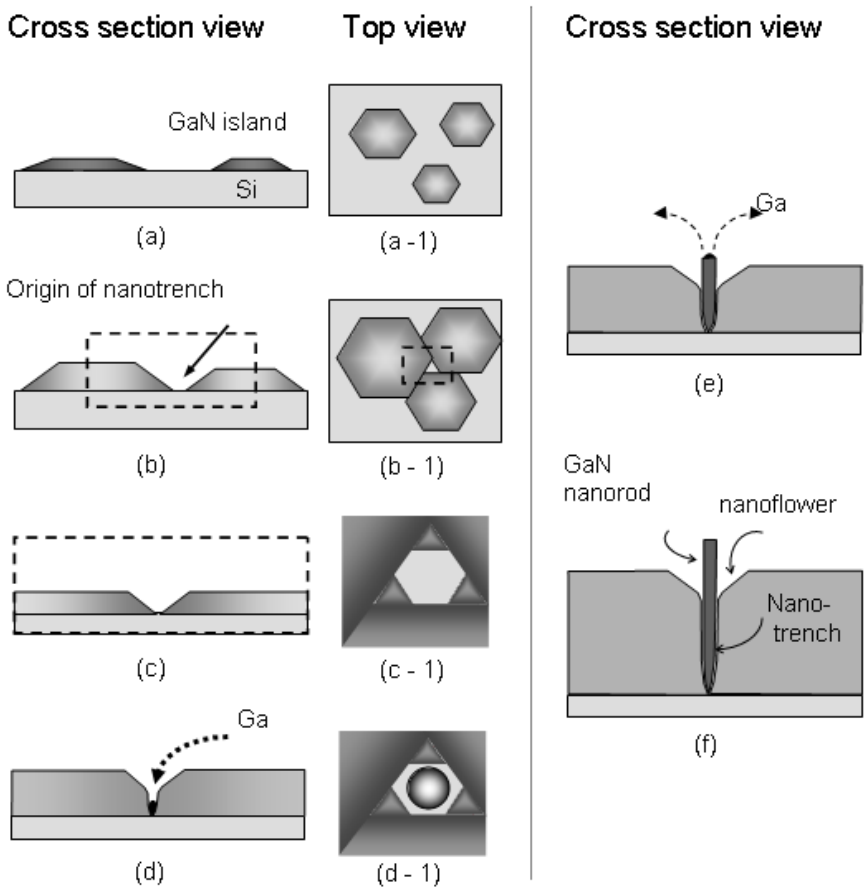

Figure 3.23. Evolution of nanorod: (a) Initial stage of GaN island growth. (b) Impinging hexagonal islands and the formation of a triangular void region. (c) Corner filling of the triangular void and its evolution into hexagonal shape, precursor to the nanoflower. (d) Evolution of the nanoflower and start of the nanotrench formation and capillary condensation of Ga atoms in the trench. (e) VLS growth mechanism prevails and the nanorod grows faster, leading to protrusion above the nanoflower. As the protrusion occurs, the condition for capillary condensation diminishes and VS growth mechanism takes over. (f) The ultimate structure.

With the hexagonal empty region in place, the islands would continue to grow in the vertical dimension and the six facets surrounding the region would then be elevated,

eventually becoming what one observes as a six-leaf nanoflower. The nanotrenches underneath the nanoflower are essentially like an attached capillary tube, as shown in Figure 23 (d). When the capillary tube is long enough, capillary condensation of Ga atoms occurs as a consequence of the decreases in the equilibrium vapor pressure due to the reduced radius of curvature, *r*, of a concave surface, as seen from the Thomson (Lord Kelvin) equation: $k_B T \log[P_{Ga}(r)/P_{Ga}(\infty)]=2\gamma^{LV}V_{Ga}/r$. k_B is Boltzmann constant, $P_{Ga}(r)$ the actual vapor pressure, $P_{Ga}(\infty)$ the saturated vapor pressure, γ^{LV} surface tension, V_{Ga} the molar volume, *r* the radius of liquid droplets.

GaN nanorods grow faster along <0001> via the canonical VLS mechanism [104] by reaction of the nitrogen plasma with Ga liquid clusters while its surrounding GaN islands also grow alongside to form the base material, though at a slower rate. Figs. 10(c)-(f) illustrate this sequence of evolution. Here, as a nanorod outgrows the nanotrench and starts to stick out of the base film surface, the equilibrium vapor pressure would gradually increase, which favors the evaporation of the droplets on top of the nanorods, as shown in Fig. 10(e). The process eventually reaches a steady state after which the rods grow at the same rate as the surrounding film via the VS growth mechanism.

In addition to the above naturally-occurring process, Seo *et al* [107] and Chu *et al* [108] have also envisaged a method to foster the capillary effects by surface engineering via ion-beam surface modifications. With self-implantation of Si into Si substrates, they were able to control the growth of nanorod arrays. Periodic patterns were realized first by traditional UV lithography followed by Si ion self-implantations. The defects generated as a result, especially the vacancies, coupled with the heating process provide the necessary driving force for nucleation and growth in the implanted area. The

density of nanorods in the patterned arrays can be controlled by the energy and dosage of the self-implantation that determines the vacancy concentration near the free surface. Linear arrays of 10 μm in width were patterned on Si (111) substrates by conventional UV-lithography such that masked and unmasked regions alternated themselves. The samples were then implanted with 40 kV Si ions to various dosages at room temperature with the Si beam current kept below 100 nA to avoid excessive target heating. Due to the nature of forward momentum transfer by ion implantation, an interstitial rich region takes shape in the region close to the end of projectile range deep in the substrate, leaving behind a vacancy-rich region close to the free surface. Upon heating prior to the GaN growth, the vacancies would coalesce to give a corrugated surface that forms the basis of nano-capillaries. While this method may produce the nanorods more easily, growth conditions can be set, especially the flow rate ratio of Ga:N to achieve the nanorod structure.

In any case, the nanorods grow faster than the surrounding matrix area via VLS growth mechanism at the early stage, while intrinsic polarity might have also contributed to the protrusion of the nanorods [109]. The sample preparation followed typical cleaning by HF etching as a precaution for further ultrahigh vacuum (UHV) processing, in which the Si substrates were transferred into an MBE growth chamber with a base pressure of ~ 10^{-10} Torr. The samples went through an 810 ºC pre-heating for 50 minutes before deposition in order to get rid of any HF residue. A buffer layer of GaN (0001) was first grown under an equivalent N/Ga pressure ratio ~ 100 at 550 ˚C. The ensuing growth of nanorods and the accompanying matrix thin film on the GaN buffer was carried out at an N/Ga equivalent pressure ratio ~ 30. The N_2 plasma power

was ~ 500 W and the substrate temperature was ~ 720 ˚C during the film deposition [110].

†Figure 3.24 shows the SEM and AFM (atomic force microscope) images of the obtained nanostructure sample.

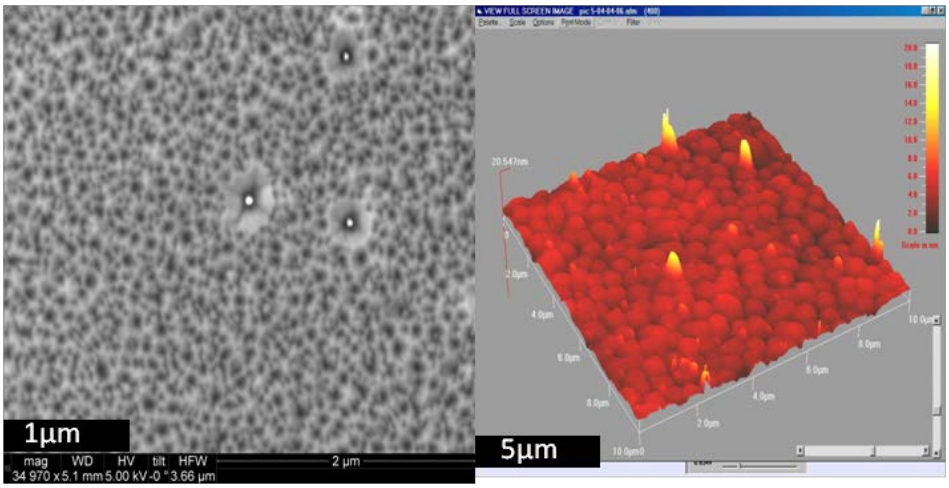

Figure 3.24. Scanning electronic microcope image (left) and atomic force microscope image (right) of GaN nanorods.

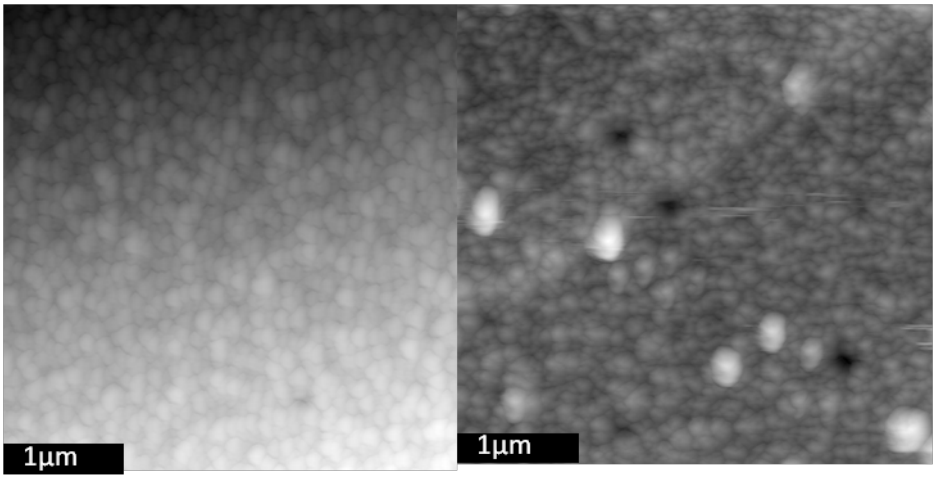

Figure 3.25. Atomic force microscope images of GaN (left) before Cs deposition and (right) after Cs deposition.

†Figures 3.24-3.25 and paragraphs in section 3.6 indicated with cross (†) are from work done with Morgan Lynch in our lab, with REU (Research Experiences for Undergraduates summer program).

The FE properties of the obtained nanostructured samples were studied as a function of various exposures of O_2, CO_2, H_2O and N_2 gases from 65 L to 6500 L. The experimental set-up and procedure were as described in the previous section in this paper on the effects of gases on ZnO nanorods grown using the arc discharge method, except that the anode-sample distance was approximately 3.7 μm. As shown in Figure 3.27 (a), after 6,500 L of O_2 exposure, the turn-on voltage increased significantly by approximately 100% from 170 to 340 V. The slope of the FN curve also increased indicating an increase in work function of 60%, assuming β remained the same. As shown in Figures 3.27 (b) and 3.28 (a), after 6,500 L of CO_2 and H_2O exposure, the turn-on voltage increased by approximately 35% and 38%, respectively; from 200 to 270 V and 240 to 330 V, respectively. The work function increased significantly by 50% after CO_2 exposure, but remained approximately the same after H_2O exposure. After 6,500 L of N_2 exposure, the turn-on voltage increased by approximately 35%, from 340 to 460 V, and the work function remained approximately the same, as shown in Figure 3.28 (b).

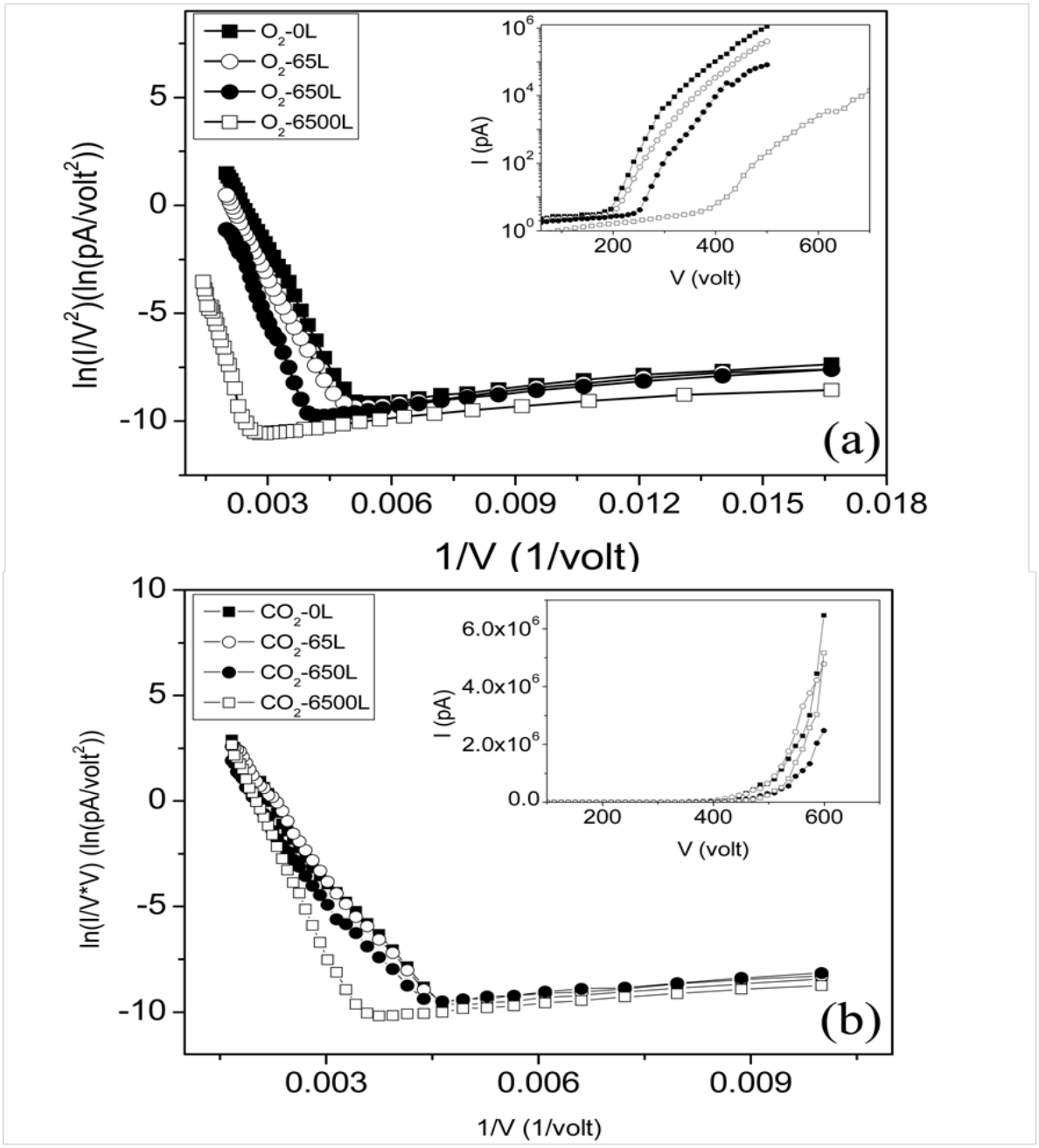

Figure 3.26. Fowler-Nordheim curves for the GaN nanorods after exposures of 0 L, 65 L, 650 L and 6,500 L at 3 x 10^{-7} Torr of (a) O_2 and (b) CO_2.

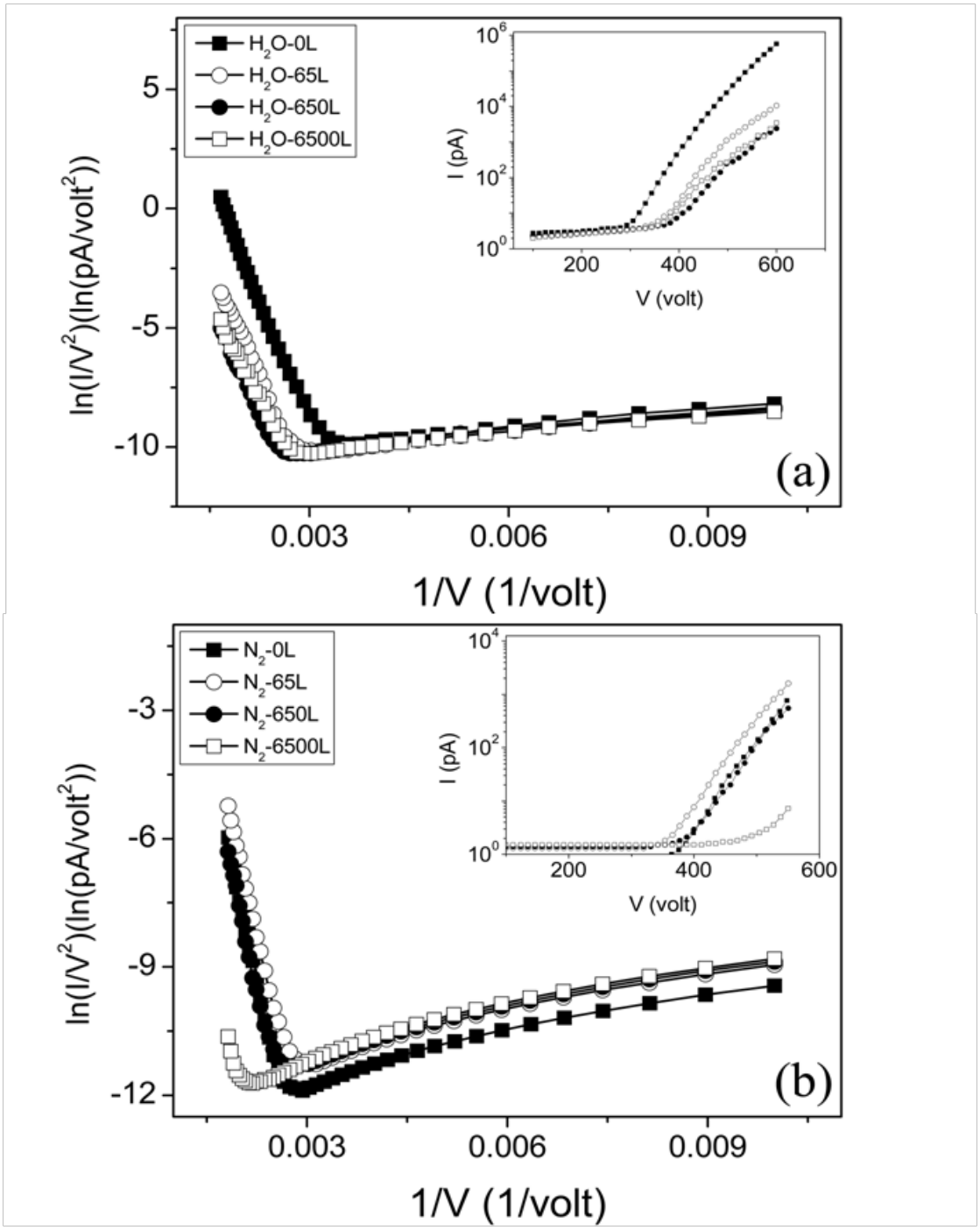

Figure 3.27. Fowler-Nordheim curves for the GaN nanorods after exposures of 0 L, 65 L, 650 L and 6,500 L at 3 x 10^{-7} Torr of (a) H_2O and (b) N_2.

We also investigated the effects of Cs deposition on the FE properties of the GaN nanorods. The sample was placed in a UHV chamber at a base pressure < 10^{-10} Torr. A Cs-metal dispenser from SAES Getters [111] was used to deposit approximately 1 monolayer of Cs on the sample. As shown in Figure 3.28, Cs deposition resulted in a decrease in turn-on voltage of approximately 30%, from 370 to 260 V. The work function decreased by approximately 60%, assuming β remained the same. We propose that the improvement in FE properties is due to a Cs-induced space-charge layer at the surface that reduces the barrier for FE such as by producing an NEA surface [112-115]. It has been reported that Cs deposition on GaN films produces an NEA surface [116-118]. It would be interesting to investigate if Cs deposition improves the FE properties of ZnO, ZnS and other wide-band-gap nanostructures.

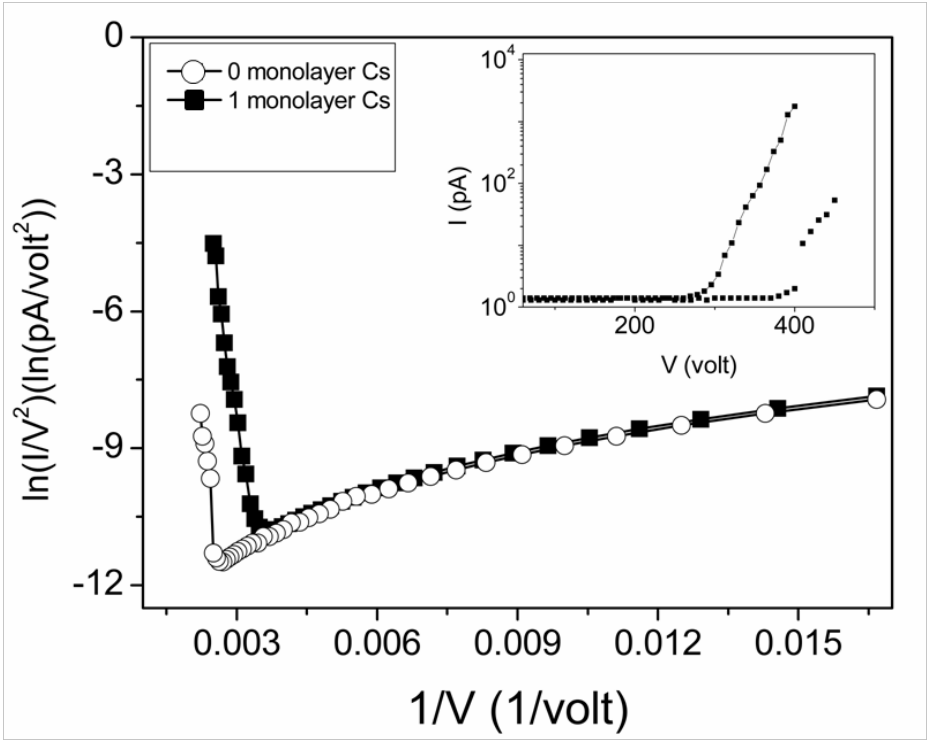

Figure 3.28. Fowler-Nordheim curves for the GaN nanorods before and after 1 monolayer of Cs exposure.

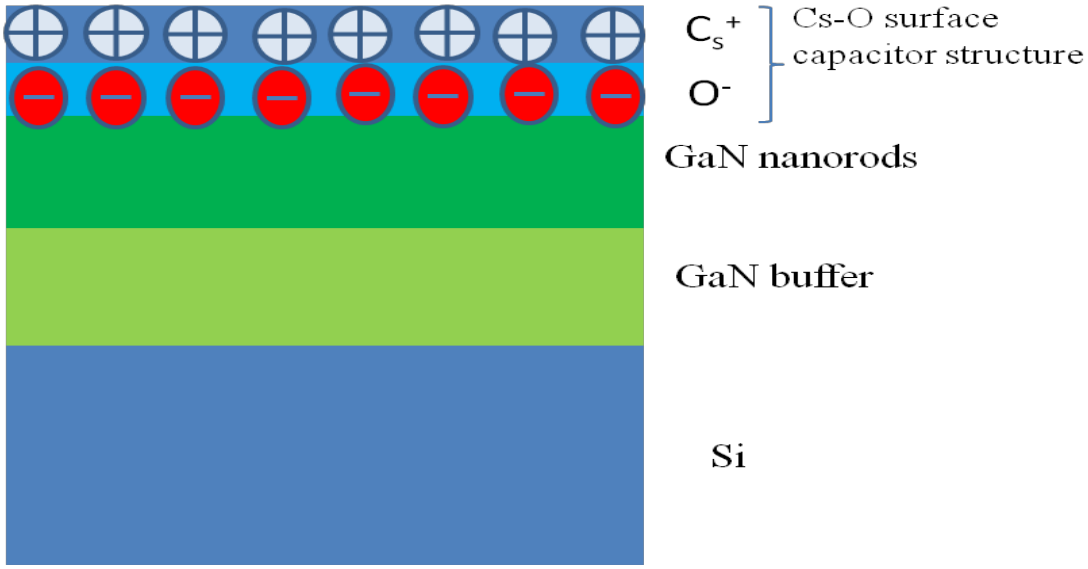

Figure 3.29. Schematic illustration of Cs deposition forming a space-charge layer.

The mechanism that Cesium deposition reduces the turn-on voltage can be considered as follows: A layer of cesium atoms deposited on the GaN nanorods combines with O_2 adsorbed on the GaN nanorods to form a space-charge layer on the very surface. The space-charge layer produces an electrical field inward to the GaN nanorods. This electrical field helps pull electrons from inside of GaN to the surface layer of cesium. Once the electrons reach cesium with the lowest work function, electrons can escape easily from the GaN and form FE, as shown in Figure 3.29.

We note that in the same family of the III-Nitrides, InN has recently been reported to show record-low turn-on voltages; however, its long-term performance stability as compared to GaN, which may last as long as 8 hours at 1mA FE current, is still unclear

[119]. It remains for future studies to understand what dictates the turn-on characteristics and to what extent one can work to reduce it for practical device applications when the fundamental surface physics or chemistry is better known.

3.7 Acknowledgments

J.J. Schwartz, M.H. Lynch and I thank the National Science Foundation Research Experience for Undergraduates program for support. This work was supported, in part, by a Faculty Research Grant from the University of North Texas. Support by the National Science Council of Taiwan is acknowledged.

3.8 References

1. Lee, C.J., Lee, T.J., Lyu, S.C., Zhang, Y., Ruh, H., Lee, H.J.: Field emission from well-aligned zinc-oxide nanowires grown at low temperature. Appl. Phys. Lett. 81, 3648-3650 (2002).
2. Dong, L.F., Jiao, J, Tuggle, D.W., Petty, J.M., Ellis S.A., Coulter, M.: ZnO nanowires formed on tungsten substrates and their electron field emission properties. Appl. Phys. Lett. 82, 1096 (2003).
3. Zhu, Y.W., Zhang, H.Z., Sun, X.C., Feng, S.Q., Xu, J., Zhao, Q., Xiang, B., Wang, R.M., Yu, D.P.: Efficient field emission from ZnO nanoneedle arrays. Appl. Phys. Lett. 83, 144 (2003).
4. Li, Y.B., Bando, Y., Goldberg, D.: ZnO nanoneedles with tip surface perturbations: excellent field emitters. Appl. Phys. Lett. 84, 3603 (2004).
5. Tseng, Y.K., Huang, C.J., Cheng, H.M., Lin, I.N., Liu, K.S., Chen, I.C.: Characterization and field-emission properties of needle-like zinc oxide nanowires grown vertically on conductive zinc oxide films. Adv. Funct. Mater. 13, 811-814 (2003).

6. Xu, C.X., Sun, X.W.: Field emission from zinc oxide nanopins. Appl. Phys. Lett. 83, 3806 (2003).
7. Li, S.Y., Lin, P., Lee, C.Y., Tseng, T.Y.: Field emission and photofluorescent characteristics of zinc oxide nanowires synthesized by a metal catalyzed vapor-liquid-solid process. J. Appl. Phys. 95, 3711 (2004).
8. Jo, S.H., Lao, J.Y., Ren, Z.F., Farrer R.A., Baldacchini, T., Fourkas, J.T.: Field emission studies on thin films of zinc oxide nanowires. Appl. Phys. Lett. 83, 4821-4823 2003).
9. Wan, Q., Yu, K., Wang, T.H., Lin, C.L.: Low field electron emission from tetrapod-like ZnO nanostructures synthesized by rapid evaporation. Appl. Phys. Lett. 83, 2253-2255 (2003).
10. Zhao, Q., Zhang, H.Z., Zhu, Y.W., Feng, S.Q., Sun, X.C., Xu, J., Yu, D.P.: Morphological effects on the field emission of ZnO nanorod arrays. Appl. Phys. Lett. 86, 203115-203115 (2005).
11. Ye, Z.Z., Yang, F., Lu, Y. F., Zhi, M. J.,Tang, H. P., Zhu, L. P.: ZnO nanorods with different morphologies and their field emission properties. Solid State Communications 142, 425 (2007).
12. Xu, C.X., Sun, X.W., Chen, B.J.: Field emission from gallium-doped zinc oxide nanofiber array. Appl. Phys. Lett. 84, 1540 (2004).
13. Kim, D.H., Jang, H.S., Lee, S.Y., Lee, H.R.: Effects of gas exposure on the field-emission properties of ZnO nanorods. Nanotechnology 15, 1433-1436 (2004).

14. Jang, H.S., Kang, S.O., Nahm, S.H., Kim, D.H., Lee, H.R., Kim, Y.I.: Enhanced field emission from the ZnO nanowires by hydrogen gas exposure. Materials Letters 61, 1679-1682 (2007).
15. Yeong, K.S., Meung, K.H., Thong, J.T.L.: The effects of gas exposure and UV illumination on field emission from individual ZnO nanowires. Nanotechnology 18, 185608-185611 (2007).
16. Temple, D.: Recent progress in field emitter array development for high performance applications. Mater. Sci. Eng. R 24, 185.
17. Schwoebel, P.R., Brodie, I.: Surface-science aspects of vacuum microelectronics, J. Vac. Sci. Technol. B 13, 13911410 (1995).
18. Chalamala, B.R., Wallace, R.M., Gnade, B.E.: Surface conditioning of active field emission cathode arrays with H_2 and helium. J. Vac. Sci. Technol. B 16, 2855-2858 (1998).
19. de Heer, W.A., Chatelain, A., Ugarte, D.: A carbon nanotube field-emission electron source. Science 270, 1179 (1995).
20. Gulyaev, Y.V., Chernozatonskii, L.A., Kosakovskaja, J.Z., Sinitsyn, N.I., Torgashov, G.V., Zakharchenko, Y.F.: Field emitter arrays on nanotube carbon structure films. J. Vac. Sci. Technol. B 13, 435 (1995).
21. Wang, Q.H., Setlur, A.A., Lauerhaas, J.M., Dai, J.Y., Seelig, E.W., Chang, R.P.H.: A nanotube-based field-emission flat panel display. Appl. Phys. Lett. 72, 2912 (1998).
22. Choi, W.B., Chung, D.S., Kang, J.H., Kim, H.Y., Jin, Y.W., Han, I.T., Lee, Y.H., Jung, J.E., Lee, N.S., Park, G.S., Kim, J.M.: Fully sealed, high-brightness carbon-nanotube field-emission display. Appl. Phys. Lett. 75, 3129-3131 (1999).

23. Dean, K.A., Chalamala, B.R.: The environmental stability of field emission from single walled carbon nanotubes. Appl. Phys. Lett. 75, 3017-3019 (1999).
24. Lim, S.C., Choi, Y.C., Jeong, H.J., Shin, Y.M., An K.H., Bae, B.J., Lee, Y.H., Lee, N.S., Kim, J.M.: Effect of gas exposure on field emission properties of carbon nanotube arrays. Adv. Mater. 20, 1563-1567 (2001).
25. Wadhawan, A., Stallcup, R.E., Stephens, K.F., Perez, J.M., Akwani, I.A.: Effects of O_2, Ar, and H_2 gases on the field-emission properties of single-walled and multiwalled carbon nanotubes. Appl. Phys. Lett. 79, 1867-1869 (2001).
26. Sheng, L.M., Liu, P., Liu, Y.M., Qian, L., Huang, Y.S., Liu, L., Fan, S.S.: Effects of carbon-containing gases on the field-emission current of multiwalled carbon-nanotube arrays. J. Vac. Sci. Technol. A 21, 1202 (2003).
27. See, for example, Yi, G.C., Wang, C., Park, W.I.: ZnO nanorods: synthesis, characterization and applications. Semicond. Sci. Technol. 20, 22-34 (2005).
28. Wei, A., Sun, X.W., Xu, C.X., Dong, Z.L., Yu, M.B., Huang, W.: Stable field emission from hydrothermally grown ZnO nanotubes. Appl. Phys. Lett. 88, 213102 (2006).
29. Wagner, R.S. and Ellis, W.C.: Vapor-liquid-solid mechanism of single crystal growth. Appl. Phys. Lett. 4, 89 (1964).
30. Huang, M.H., Wu, Y.Y., Feick, H., Tran N., Weber E., and Yang, P.D.: Catalytic growth of zinc oxide nanowires by vapor transport. Adv. Mater. 13, 113 (2001).
31. Li, S.Y., Lee, C.Y. and Tseng, T.Y.: Copper-catalyzed ZnO nanowires on silicon (100) grown by vapor-liquid-solid process. J. Cryst. Growth 247, 357 (2003).

32. Ding Y., Gao, P.X., and Wang, Z.L.. Catalyst-nanostructure interfacial lattice mismatch in determining the shape of VLS grown nanowires and nanobelts: a case of Sn/ZnO. J. Am. Chem.oc. 126, 2066 (2004).
33. Konenkamp, R., Boedecker, K., Lux-Steiner, M.C., Poschenrieder, M., Zenia, F., Clement, C.L., Wagner, S., Appl. Phys. Lett. 77, 2575 (2000).
34. Liu, X., Wu, X., Cao, H., and Chang, R.P.H.: Growth mechanism and properties of ZnO nanorods synthesized by plasma-enhanced chemical vapor deposition. J. Appl. Phys. 95, 3141 (2004).
35. Park, W.I., Kim, D.H., Jung, S.W., and Yi, G.C.: Metaloranic vapor-phase epitaxial growth of vertically well-alligned ZnO nanorods. Appl. Phys. Lett. 80, 4232 (2002).
36. Park, W.I., Yi, G.C., Kim, M.Y, Pennycook, S.J.: ZnO nanoneedles grown vertically on Si substrates by non-catalytic vapor-phase epitaxy. Adv. Mater. 14, 1841 (2002).
37. Kim, K.S., Kim, H.W.: Synthesis of ZnO nanorod on bare Si substrate using metal organic chemical vapor deposition. Physica B 328, 368 (2003).
38. Maejima, K., Ueda, M., Fujita, S., Fujita, S.: Growth of ZnO nanorods on a-plane (120) sapphire by metal-organic vapor phase epitaxy. Japan. J. Appl. Phys. 42, 2600 (2003).
39. Park, J.Y., Oh, H., Kim, J.J., Kim, S.S.: Growth of ZnO nanorods via metalorganic chemical vapor deposition and their electrical properties. J. Cryst. Growth 287, 145-148 (2006).
40. Park, W.I., Kim, D.H., Jung, S.W., Yi, G.C.: Appl. Phys. Lett. 80, 4232 (2002).
41. An, S.J., Park, W.I., Yi, G.C., Kim, Y.J., Kang, H.B., Kim, M.: Heteroepitaxial fabrication and structural characterizations of ultrafine GaN/ZnO coaxial nanorod heterostructures. Appl. Phys. Lett. 84, 3612 (2004).

42. Heo, Y.W., Varadarajan, V., Kaufman, M., Kim, K., Norton, D.P., Ren, F., Fleming, P.H.: Site-specific growth of ZnO nanorods using catalysis-driven molecular-beam epitaxy. Appl. Phys. Lett. 81, 3046-3048 (2002).
43. Pearton, S.J., Tien, L.C., Norton, D.P., Hung-Ta, W., Ren, F.: Nucleation control for ZnO nanorods grown by catalyst-driven molecular beam epitaxy. Appl. Surf. Sci. 253, 4620-4625 (2007).
44. Li, Y., Meng, G.W., Zhang, L.D., Phillip, F.: Ordered semiconductor ZnO nanowire arrays and their photoluminescence properties. Appl. Phys. Lett. 76, 2011 (2000).
45. Park, W.I., Yi, G.C., Kim, M., Pennycook S.J.: Quantum confinement observed in Zn)/ZnMgO quantum structures. Adv. Mater. 15, 526 (2003).
46. Geng, B.Y., Wang, G.Z., Jiang, Z., Xie, T., Sun, S.H., Meng, G.W., Zhang, L.D.: Synthesis and optical properties of S-doped ZnO nanowires. Appl. Phys. Lett. 82, 4791.
47. Bae, S.Y., Seo, H.W., Park, J.: Vertically-aligned sulfur-doped ZnO nanowires synthesized via chemical vapor deposition. J. Phys. Chem. B 108, 5206 (2004).
48. Wan, Q., Li, Q.H., Chen, Y.J., Wang, T.H., He, X.L., Gao, X.G., Li, J.P.: Positive temperature coeficient resistance and humidity sensing properties of Cd-doped ZnO nanowires. Appl. Phys. Lett. 84, 3085 (2004).
49. Vayssieres, L.: Growth of arrayed nanorods and nanowires of ZnO from aqueous solutions. Adv. Mater. 15, 464-466 (2003).
50. Wang, Z., Qian, X., Yin, J., Zhu, Z.: Aqueous solution fabrication of large-scale arrayed obelisk-like zinc oxide nanorods with high efficiency. J. Solid State Chem. 177, 2144-2149 (2004).

51. Lee, J.H., Leu, I.C., M.H. Hon: Substrate effect on the growth of well-aligned ZnO nanorod arrays from aqueous solution. J. Cryst. Growth 275, e2069-e2075 (2005).
52. Lin, C.C., Chen H.P., Chen, S.Y.: Synthesis and optoelectronic properties of arrayed p-type ZnO nanorods grown on ZnO films/Si wafer in aqueous solutions. Chem. Phys. Lett. 404, 30-34 (2005).
53. Tak, Y, Yong, K.: Controlled growth of well-aligned ZnO nanorod array using a novel solution method. J. Phys. Chem. B 109, 19263-19269 (2005).
54. Wahab, R., Ansari, S.G., Kim, Y.S., Seo, H.K., Kim, G.S., Khag, G., Shin, H.S.: Low temperature solution synthesis and characterization of ZnO nano-flowers. Mater. Res. Bull. (2006), doi: 10.1016/j.materresbull.2006.11.035.
55. Yu, K., Jin, Z., Liu, X., Liu, Z., Fu, Y.: Synthesis of size-tunable ZnO nanorod arrays from $NH_3{\cdot}H_2O/ZnNO_3$ solutions. Materials Lett. 61, 2775-2778 (2007).
56. Liu, B. Zeng, H.C.: Hydrothermal synthesis of ZnO nanorods in the diameter regime of 50 nm. J. Am. Chem. Soc. 125, 4430 (2003).
57. Li, Z.Q., Xiong, Y.J., Xie, Y.: Selected-control synthesis of ZnO nanowires and nanorods via a PEG-assisted route. Inorg. Chem. 42, 8105 (2003).
58. Choy, J.H., Jang, E.S., Won, J.H., Chung, J.H., Jang, D.J., Kim, Y.W.: Hydrothermal route to ZnO nanocoral reefs and nanofibers. Appl. Phys. Lett. 84, 287 (2004).
59. Wang, J.M., Gao, L.: Wet chemical synthesis of ultralong and straight single-crystalline ZnO nanowires and their excellent UV emission properties. J. Mater. Chem. 13 2551 (2003).

60. Marathe, S.K., Koinkar, P.M., Ashtaputre, S.S., More, M.A., Gosavi, S.W., Joag, D.S., Kulkarni, S.K.: Efficient field emission from chemically grown inexpensive ZnO nanoparticles of different morphologies. Nanotechnology 17, 1932-1936 (2006).
61. Ahsanulhaq, Q., Kim, J.H., Hahn, Y.B.: Controlled selective growth of ZnO nanorod arrays and their field emission properties. Nanotechnology 18, 485307-485313 (2007).
62. Chen, J.C., Chai, W., Zhang, Z., Li, C., Zhang, X.: High field emission enhancement of ZnO-nanorods via hydrothermal synthesis. Solid State Electronics 52, 294-298 (2008).
63. Gudiksen, M.S., Lauhon, L.J., Wang, J., Smoth, D.C., Lieber, C.M.,: Growth of nanowire superlattice structures for nanoscale photonics and electronics. Nature 415, 617-620 (2002).
64. Dai, Y., Zhang, Y., Li, Q.K., Nan C.W.: Synthesis and optical properties of tetrapod-like zinc oxide nanorods. Chem. Phys. Lett. 358, 83 (2002).
65. Lyu, S.C., Zhang, Y., Lee, C.J., Ruh, H., Lee, H.J.: Low-temperature growth of ZnO nanowire array by a simple physical vapor-deposition method. Chem. Mater. 15, 3294 (2003).
66. Zhang, Y., Wang, N., Gao, S., He, R., Miao, S., Liu, J., Zhu, J., Zhang, Z.: A simple method to synthesize nanowires. Chem. Mater. 14, 3564 (2002).
67. Yao, B.D., Chan, Y.F., Wang N.: Formation of ZnO nanostructures by a simple way of thermal evaporation. Appl. Phys. Lett. 81, 757 (2002).
68. Gao, P.X., Wang, Z.L.,: Self-assembled nanowire-nano-ribbon junctions arrays of ZO. J. Phys. Chem. B 106, 12653 (2002).

69. Lao, J.Y., Wen, J.G., Ren, Z.F.: Hierarchical ZnO nanostructures. Nano Lett. 2, 1287 (2002).

70. Gundiah, G., Deepak, F.L., Govindaraj, A., Rao, C.N.R.: Carbothermal synthesis of the nanostructures of AlO_3 and ZnO. Top. Catal. 24, 137 (2003).

71. Choi,J.H., Tabata, H., Kawai, T., J. Cryst. Growth 226, 493 (2001).

72. Obuliraj, S.K., Yamauchi, K., Hanada, Y., Miyamoto, M., Ohba, T., Morito, S., Fujita, Y.: Nitrogen doped ZnO nanomaterials for UV-LED applications. Proc. 2nd IEEE Int. Conf. NanoMicro Eng. Mol. Sys., 159-162 (2007).

73. Fowler, R.H., Nordheim, L.: Electron emission in intense electric fields. Proc. R. Soc. London, Ser. A 119, 173-181 (1928).

74. Boscolo, I., Cialdi, S., Fiori, A., Orlanducci, S., Sessa, V., Terranova, M.L., Ciorba, A., Rossi, M.: Capacitive and analytical approaches for the analysis of field emission from carbon nanotubes in a sphere-to-plane diode. J.Vac.Sci.Technol. B 25, 1253-1260 (2007).

75. Mo, Y., Neogi, A., Perez, J.M., Fujita, Y.: Effects of residual gases on the field emission properties of ZnO nanorods. Poster presented at the Japan Society for the Promotion of Sciences - University of North Texas Winterschool on Nanophotonics, University of North Texas, Denton, TX, February 14-15, 2008.

76. EXFO Burleigh, Quebec, Canada (www.exfo.com/en/burleigh.asp).

77. Ito, F., Tomihari, Y., Okada, Y., Konuma, K., Okamoto, A.: Carbon-nanotube-based triode-field-emission displays using gatedemitter structure. IEEE Elect. Dev. Lett. 22, 426 (2001).

78. Liu, J., Zhirnov, V.V., Choi, W.B., Wojak, G.J., Myers, A.F., Cuomo, J.J., Hren, J.J.: Electron emission from a hydrogenated diamond surface. Appl. Phys. Lett. 69, 4038-4040 (1996).
79. Lim, S.C., Stallcup II, R.E., Akwani, I.A., Perez, J.M.: Effects of O_2, H_2, and N_2 gases on the field emission properties of diamond-coated microtips. Appl. Phys. Lett. 75, 1179-1181 (1999).
80. Liu, M. Kim, H.K.: Ultraviolet detection with ultrathin ZnO epitaxial films treated with oxygen plasma. Appl. Phys. Lett. 84, 173175 (2004).
81. Losurdo, M, Giangregorio, M.M., Capezzuto, P., Bruno, G., Malandrino, G., Blandino, M., Fragala, I.L.: Reactivity of ZnO: Impact of polarity and nanostructure. Superlattices and Microstructures 38, 291-299 (2005).
82. Maki, H., Ichinose, N., Sakaguchi, I., Ohashi, N., Haneda, H., Tanaka, J.: The effect of the nitrogen plasma irradiation on ZnO single crystals. Key Eng. Materls. 216, 61 (2002).
83. Yamaga, S., Yoshikawa, A., Kasa, H.: Electrical and optical properties of donor doped ZnS films grown by low-pressure MOCVD. J. Cryst. Growth 86, 252-256 (1988).
84. Ye, C., Fang, X., Li, G., Zhang, L.: Origin of the green photoluminescence from zinc sulfide nanobelts. Appl. Phys. Lett. 85, 3035-3037 (2004).
85. Vacassy, R., Scholz, S.M., Dutta, J., Plummer, C.J.G., Houriet, R., Hofmann, H.: Synthesis of Controlled Spherical Zinc Sulfide Particles by Precipitation from Homogeneous Solutions. J. Am. Ceram. Soc. 81, 2699-2705 (1998).
86. Liu, X., Caia, X., Maob, J., Jinc, C.: ZnS/Ag/ZnS nano-multilayer films for transparent electrodes in flat display application. Appl. Surf. Sci. 183, 103-110 (2001).

87. Shao, L.X., Chang, K.H., Hwang, H.L.: Zinc sulfide thin films deposited by RF reactive sputtering for photovoltaic applications. Appl. Surf. Sci. 212–213, 305-310 (2003).
88. Johnstona, D.A., Carlettoa, M.H., Reddyb, K.T.R., Forbesa, I., Miles, R.W.: Chemical bath deposition of zinc sulfide based buffer layers using low toxicity materials. Thin Sol. Films 403–404, 102-106 (2002).
89. Meng X.M., Liu, J., Jiang, Y., Chen, W.W., Lee, C.S., Bello, I., Lee, S.T.: Structure- and size-controlled ultrafine ZnS nanowires. Chem. Phys. Lett. 382, 434-438 (2003).
90. Zhu, Y.C., Bando, Y., Xue, D.F.: Spontaneous growth and luminescence of zinc sulfide nanobelts. Appl. Phys. Lett. 82, 1769-1771 (2003).
91. Lu, F., Cai, W., Zhang, Y., Li, Y., Sun, F., Heo, S.H., Cho, S.O.: Appl. Phys. Lett. 89, 231928 (2006).
92. Khosravi, A.A., Kundu, M., Jatwa, L., Deshpande, S.K., Bhagwat, U.A., Sastry, M., Kulkarni, S.K.: Green luminescence from copper doped zinc sulphide quantum particles. Appl. Phys. Lett. 67, 2702-2704 (1995).
93. Zhang, D., Qi, L., Cheng, H., Ma, J.: Preparation of ZnS Nanorods by a Liquid Crystal Template. J. Colloid Interface Sci. 246, 413-416 (2002).
94. Lu, F., Cai, W., Zhang, Y., Li, Y.,Sun, F., Heo, S.H., Cho, S.O.: Fabrication and Field-Emission Performance of Zinc Sulfide Nanobelt Arrays. J. Phys. Chem. C 111, 13385-13392 (2007).
95. Ha, B., Seo, S.H., Cho, J.H., Yoon, C.S., Yoo, G-C.Y., Park, C.Y., Lee, C.J.: optical and field emission properties of thin single-crystalline GaN nanowires. J. Phys. Chem. B 109, 11095-11099 (2005)

96. Yilmazoglu, O., Pavlidis, D., Litvin, Yu.M., Hubbard, S., Tiginyanu, I.M., Mutamba K., Hartnagel, H.L., Litovchenko, V.G., . Evtukh, A.: Field emission from quantum size GaN structures. Applied Surface Science 220, 46–50 (2003).
97. Komirenko, S.M., Kim, K.W., Kochelop, V.A., Stroscio, M.A.: High-field electron transport controlled by optical photon emission in nitrides. International Journal of High Speed Electronics and Systems. 12, 1057-1081 (2002).
98. Goodman, S.A., Auret, F.D., Koschnick, F.K., Spaeth, J.-M., Beaumont, B., Gilbart, P.: Field-enchanced emission rate and electronic properties of a defect introduced in n-GaN by 5.4 mev He-ion irradiation. Appl. Phys. Lett. 74, 809-811 (1999)
99. Tong, X.L., Jiang, D.S., Li, Y., Liu, Z.M., Luo, M.Z.: Folding field emission from GaN onto polymer microtip array by femtosecond pulsed laser deposition. Appl. Phys. Lett. 89, 061108-1-061108-3 (2006).
100. Ng, D.K.T., Hong, M.H., Tan, L.S., Zhu, Y. W., Sow, C.H.: Field emission enhancement from patterned gallium nitride nanowires. Nanotechnology 18, 375707-375711 (2007).
101. Ye, F., Xie, E.Q., Pan, X.J., Li, H., Duan, H.G., Jia, C.W.: Field emission from amorphous GaN deposited on Si by dc sputtering. J. Vac. Sci. Technol. B 24, 1358-1361 (2006).
102. Liu, B.D., Bando, Y., Tang, C.C., Xu, F.F., Hu, J.Q., Golberg, D.: Needlelike bricrystalline Gan nanowires with excellent field emission properties. J. Phys. Chem. B 109, 17082-17085 (2005).

103. Berishev, I., Bensaoula, A., Rusakova, I., Karabutov,A., Ugarov, M., Ageev, V.P.:Field emission properties of GaN films on Si(111). Appl. Phys. Lett.73, 1808-1810 (1998).

104. Levitt, Albert P., Whisker Technology, Wiley-Interscience, New York, 1970.

105. Seo, H.W., Chen, Q.Y., Tu, L.W., Hsiao, C.L., Iliev, M. N., Chu, W.K.: Catalytic nanocapillary condensation and epitaxial GaN nanorod growth. Phys. Rev. B 71, 235314 (2005)

106. Seo, H.W., Chen, Q.Y., Iliev, M.N., Tu, L.W., Hsiao, C.L., Meen, J.K., Chu, W.K.: Epitaxial GaN nanorods free from strain and luminescent defects. Appl. Phys. Lett. 88, 153124 (2006).

107. Seo, H.W., Chen, Q.Y., Tu, L.W., Chen, M., Wang, X.M., Tu, Y.J., Shao, L., Lozano O., Chu, W.K.: GaN nanorod assemblies on self-implanted (111) Si substrates. Microelectronic Engineering 83, 1714 (2006).

108. Chu, W.K., Seo, H.W., Chen, Q.Y., Wang, X.M., Tu, L.W., Hsaio, C.L., Chen, M., Tu, Y.J., US Patent Pending, 60/696,020.

109. Tsai, M.-H., Jhang, Z.-F., Jiang, J.-Y., Tang, Y.-H., Tu, L.W.: Electrostatic and structural properties of GaN nanorods/nanowires from first principles. Appl. Phys. Lett. 89, 203101 (2006).

110. Tu, L.W., Hsiao, C.L., Chi, T.W.: Self-assembled vertical GaN nanorods grown by molecular-beam epitaxy. Appl. Phys. Lett. 82, 1601 (2003).

111. SAES Getters, Inc., Colorado Springs, CO 80906.

112. Sommer, A.H. Photoemissive Materials, John Wiley and Sons, New York, 1968.

113. Bell, R.L. Negative Electron Affinity Devices, Clarenson Press, Oxford, 1973.

114. Zhu, Wei (ed.), Vacuum Microelectronics, Wiley, New York, 2001.

115. Modinos, A., Field, Thermionics, and Secondary Electron Emission Spectroscopy, Plenum Press, New York, 1984.

116. Martinelli, R.U., Pankove, J.I.: Secondary electron emission from the GaN:Cs-O surface. Appl. Phys. Lett. 25, 549-551 (1974).

117. Monch, W., Kampen, T.U., Dimitrov, R., Ambacher, O., Stutzmann, M.: Negative electron affinity of cesiated p-GaN(0001) surfaces. J. Vac. Sci. Technol. B 16, 2224-2228 (1998).

118. Machuca, F., Zhi, L., Sun, Y., Pianetta, P., Spicer, W.E., Pease, R.F.W.: Oxygen species in Cs/O activated gallium nitride (GaN) negative electron affinity photocathodes. J. Vac. Sci. Technol. B 21, 1863-1869 (2003).

119. Wang, K.R., Lin, S.J., Tu, L.W., Chen, M., Chen, Q.Y., Chen, T.H., Chen, M.L., Seo, H.W., Tai, N.H., Chang, S.C., Lo, I.K., Wang, D.P., Chu, W.K.: InN nanotips as excellent field emitters. Appl. Phys. Lett. 92, 123105 (2008)

120. Lee, J-H., Chung, Y-W., Hon, M-H. and Leu, I-C.: Appl. Phys. A 97, 403-408 (2009)

121. Kim, S., Cho, E., Han, S., Cho, Y., Hee, S., Kim, C. and Ihm, J.: Solid State Commun. 149, 670 (2009)

122. Ribaya, B.P., Leung, J., P.Brown, Rahman M. and Nguyen, C.V.: Nanotechnology 19, 185201 (2008)

123. Calderon-Colon, X., Geng,H., Gao,B., An,L., Cao,G. and Zhou, O.: Nanotechnology 20, 325707 (2009)

124. Sheng L. M., Liu P., Liu Y. M., Qian L., Huang Y. S., Liu L., and Fan S. S.: J. Vac. Sci. Technol. A 21, 1202 (2003)

125. Chalamala B.R., Wallace R.M., and Gnade B.E.: J. Vac. Sci. Technol. B 16, 2855 (1998)

126. Bonard, J-M. and Klinke, C.: Phys.Rev. B 67,115406 (2003)

127. Yi, G.C., Wang, C. and Park, W. I.: Semicond. Sci. Technol. 20, 22 (2005)

128. Cao, B., Teng, X., Heo, S., Li, Y., Cho, S., Li, G. and Cai, W.: J. Phys. Chem. C 111,2470 (2007)

129. Xiao, J., Zhang, G., Bai, X., Yu, L., Zhao, X., and Guo, D.: Vacuum 83, 265 (2009)

130. Liu, J., Sun, F. and Yu, H.: Curr. Appl Phys. 5, 625 (2005)

131. Cheng, C-L., Chao, S-H. and Chen, Y-F.: J. Cryst. Growth 311, 4381 (2009)

132. Zhang, Z., Huang, J., He, H., Lin, S., Tang, H., Lu, H. and Ye, Z.: Solid-State Electron. 53 578 (2009)

133. Lide, D.R. (ed.): *Handbook of Chemistry and* Physics, Edited D.R Lide, 74th Edition, National Institute of Standards and Technology, (CRC Press, Ann Arbor 1994), p 205.

CHAPTER 4

TUNING GRAPHENE RESISTIVITY BY LIGHT[†]

Resistance of a chemical vapor deposition (CVD) grown graphene film—transferred from water to a SiO_2/Si substrate—increases to a higher saturation value upon exposure to light of various wavelengths. We systematically investigated the phenomenon through both experimental and theoretical simulation methods. Experiments were performed with light from the visible to ultraviolet (UV) spectrum. With the same light intensity, we found that the shorter the wavelength of the light is, the higher the saturation resistance. Light in visible range causes a slight increase (up to 10%) in the resistance of the sample. A big jump in saturation resistance was found, starting from 400 nm UV irradiation. Under laboratory conditions, the tunable range approached up to 3 times of the original resistance with 254 nm UV in about 5 minutes. As soon as the light was removed, the resistance of the sample falls to its original value exponentially and slowly, with a time constant of several days. The changes are reversible and repeatable. First-principle calculations and analysis based on density functional theory show that light induced splitting of interfacial residual water molecules between a defected graphene and a SiO_2 surface may play a key role in the observed phenomenon. Our theoretical analysis also shows that 1). A water molecule nearby a graphene defect is easier to be split than the case of no defect existing; 2).There is a series of meta-stable partially disassociated

---

[†]This chapter is part of our current research work collaborating with Dr. Guanglin Zhao, Dr. Zhou Ye in the Department of Physics and Dr. Shizhong Yang and Mr. Lei Zhao in the Department of Computer Science at Southern University and A&M College, Baton Rouge, LA. The work is in part funded by Dr. Guanglin Zhao's group and computing simulation is conducted by Dr. Shizhong Yang's group.

states for an interfacial water molecule. Disassociation energies are calculated to be from 2.5 eV to 4.6 eV, that match the experimental observation range from visible to 254 nm UV light. Our results provide a way to tune the resistivity of CVD-grown graphene by light, and our analysis suggests that defected graphene may be a good candidate as a photo-catalyst for water splitting.

4.1 Introduction

Graphene, a truly two dimensional material with a carbon honey comb plane structure has attracted tremendous attention since its first realization in 2004, largely due to its unique electronic properties that makes it a promising candidate to replace silicon in the next generation of semiconductor devices and sensing applications [1-7]. In graphene, all carbon atoms are surface atoms, which is different from bulk materials where the number of surface atoms is only a small fraction of the total. As a result, all carbon atoms in graphene are exposed to the surroundings, which can make the electronic properties of graphene very sensitive to the environment. Many studies have been conducted, focusing on the effect of different adsorbates on the electronic transport properties of graphene [8-15]. Hydrogenation and oxidation of graphene, where carbon atoms on graphene chemically bind with hydrogen or oxygen atoms, accompanied with a sp^2 to sp^3 transition of the carbon bond, can convert graphene from a conductor to an insulator [16-20]. Chemical doping using different molecules, such as NO_2 on graphene, can cause slight but detectable changes to electronic properties of graphene [11]. Physisorption of H_2, O_2, N_2, CO, CO_2, and NH_3 does not lead to a significant effect on electronic properties of graphene, as reported by several groups through both experimental and theoretical studies [12,13]. One of the main purposes of those studies

was to find a reliable way to tune graphene from a conductor to a semiconductor, to meet the requirements of new and fast electronic applications. The effects of water molecules, one of the main components in the environment, on the electronic properties of graphene have also been reported [1, 4]. Yavari *et al*. reported an observation concerning the reduction of the conductivity of a CVD grown graphene film in different humidity environments and proposed that a band gap up to 0.2 eV was opened [14]. Theoretical studies found that water molecules play the role of the electron acceptor when adsorbed on graphene, and this effect is enhanced when considering the existence of the silicon dioxide substrate [15]. Recently there have been reports [21-25] suggesting that adatoms on graphene can be ionized by applying a gate voltage, and the ionization of adatoms causes a sharp change in the electrostatic potential. In this paper, we report new observations in which the resistance of a CVD grown graphene film, which is transferred from deionized (DI) water to a SiO_2 surface, can be tuned and controlled by exposure to light from the visible to ultraviolet (UV). Furthermore, we performed first-principle calculations based on the density functional theory (DFT) with a plane wave basis set to illustrate the process. Our simulation and analysis show that there is a series of possible meta-stable disassociation states (ranging from 2.6 eV to 4.85 eV) of a water molecule in between a defected graphene plane and a silicon dioxide surface. Input energy, such as light, can drive an interfacial H_2O molecule to different partially disassociation states, depending on the wavelength of incident light. The hydrogen ion from a split water molecule attaches to the graphene as a scattering center, and results in an increase of resistance of the sample. This work provides a new and convenient way to tune the

electronic properties of graphene, and a potential application to use CVD-grown graphene as a catalyst for solar splitting of water molecules.

4.2 Experimental Observations

Graphene is grown on a copper foil by the CVD method in a quartz tube furnace (See Figure 4.1) with a 2-inch inner diameter under the following conditions: temperature of 950 ºC, flow rates of 50 sccm for H_2 and 100 sccm for CH_4, and total pressure of 30 Torr for 10 minutes.

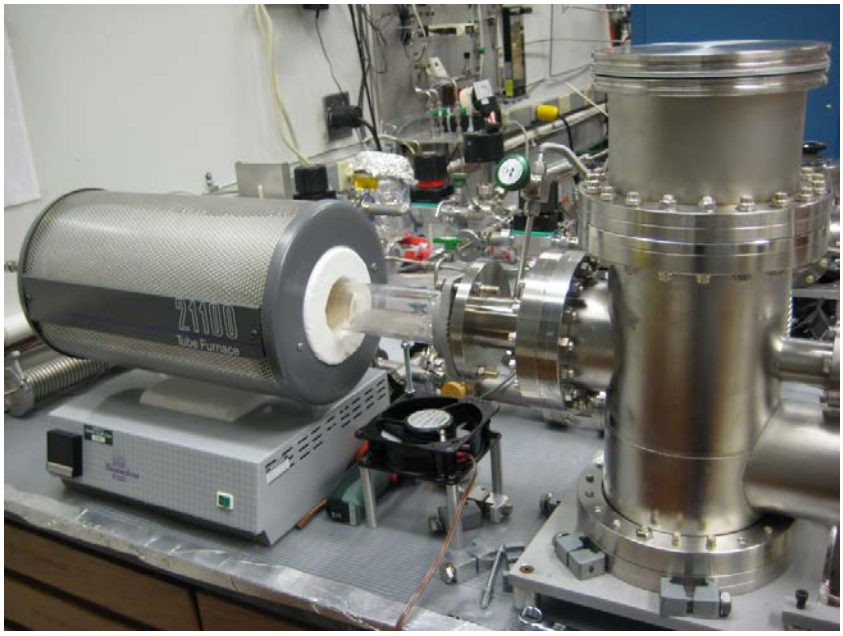

Figure 4.1. CVD system for growth and annealing of graphene.

After the copper foil is etched off in a $Fe(NO_3)_3$ solution of 1 M concentration, the floating graphene sheet is floated on the surface of 500ml of DI water; this operation is repeated 5 times for cleaning. Finally, the graphene film is transferred from the DI water onto a SiO_2 substrate, which consists of a highly p-doped Si wafer covered with a thermally grown 300nm SiO_2 layer. Four electrodes are made by thermally evaporating 10nm of Ti, 200nm of Ag, and 30nm of Au, consecutively on the sample in vacuum at a

pressure of 5×10^{-6}Torr. A sample holder of four gold-coated copper probes is used to contact the electrodes and a box with BNC out-lead connection is used for I-V measurements. The above process is shown in Fig.4.2.

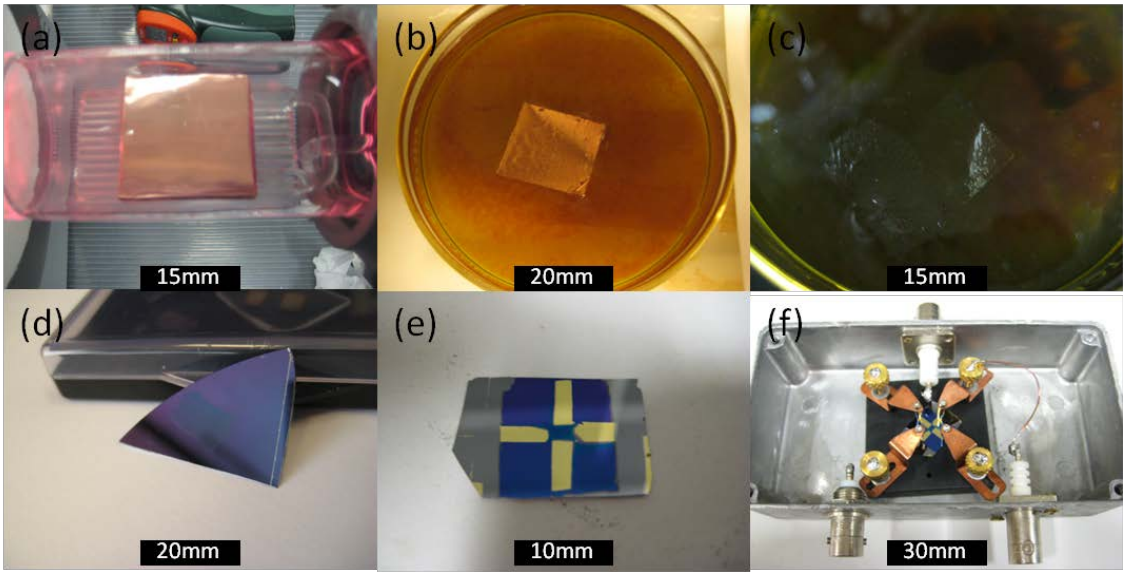

Figure 4.2. Fabrication of CVD graphene and its device. (a) A piece of 20mmx20mm with thickness of 25 μm copper foil before graphene CVD growth; (b) A copper foil after graphene growth floating on 1M $Fe(NO_3)_3$ solution for etching Cu from its bottom; (c) CVD graphene floating on solution after Cu etched; (d) CVD graphene transferred to SiO_2/Si substrate; (e) A device with four gold electrodes; (f) A device set on a sample holder ready for I-V measurement.

A comparing device with four electrodes is made of exfoliated monolayer graphene for light exposure I-V measurements (See Figure 4.3). The size of exfoliated graphene is often at a scale of micrometers. Therefore, making electrodes on exfoliated graphene for I-V measurement becomes more difficult than that on CVD grown graphene with size at scale of millimeters or centimeters. 200 mesh and 50 mesh TEM sample grids are used as a mask to make gold electrodes by vacuum metal evaporation. The width of

the bar in 200 mesh TEM grid is about 10 micrometers and this is the size of the device of exfoliated graphene. 50 mesh grids is for extending the electrodes to bigger size so that they can be more easily extended to a size of millimeter scale for measurement.

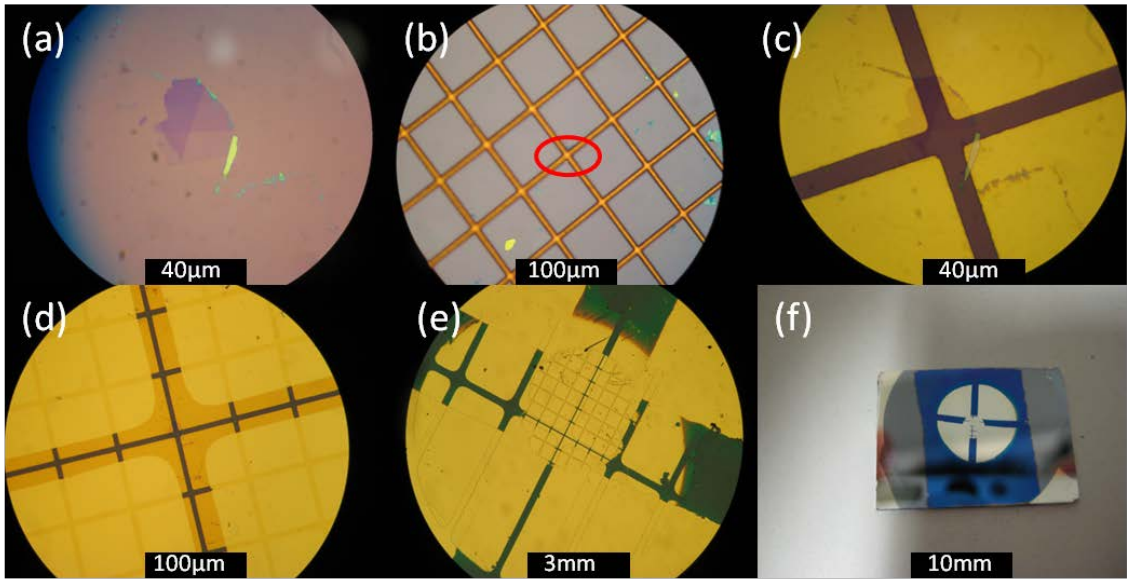

Figure 4.3. Fabrication of exfoliated grphene and its device. (a) Exfoliated monolayer graphene on SiO_2/Si substrate; (b) A 200 mesh grid placed as a mask; (c) 4 gold electrodes formed on monolayer graphene with vacuum metal evaporation; (d) Extended electrodes formed with 50 mesh TEM grid as a mask; (e) Larger extended electrodes formed, (f) Exfoliated mono graphene device with 4 gold electrodes with size of diameter of 8 mm.

The quality of the CVD-grown graphene is compared to exfoliated graphene with optical microscope image and Micro-Raman spectroscopy, as shown in Figure 4.4. Raman spectrum of CVD-grown graphene shows that it is a monolayer of graphene,

since, the full width at half maximum (FWHM) of Raman 2D peak is of 30 cm^{-1}, which is the fingerprint of monolayer graphene. However, there is a D peak in the CVD-grown graphene while no D-peak appears in Raman spectrum of exfoliated graphene. Optical microscope images shows good uniformity of the CVD-grown graphene on SiO_2/Si but with some wrinkles, while the exfoliated monolayer graphene SiO_2/Si shows perfect uniform image with no single distinguishable wrinkle or spot under the same magnification. Although the quality of exfoliated graphene is better than CVD-grown graphene, the exfoliated graphene usually is micrometer scale while the CVD-grown graphene is on the order of centimeters.

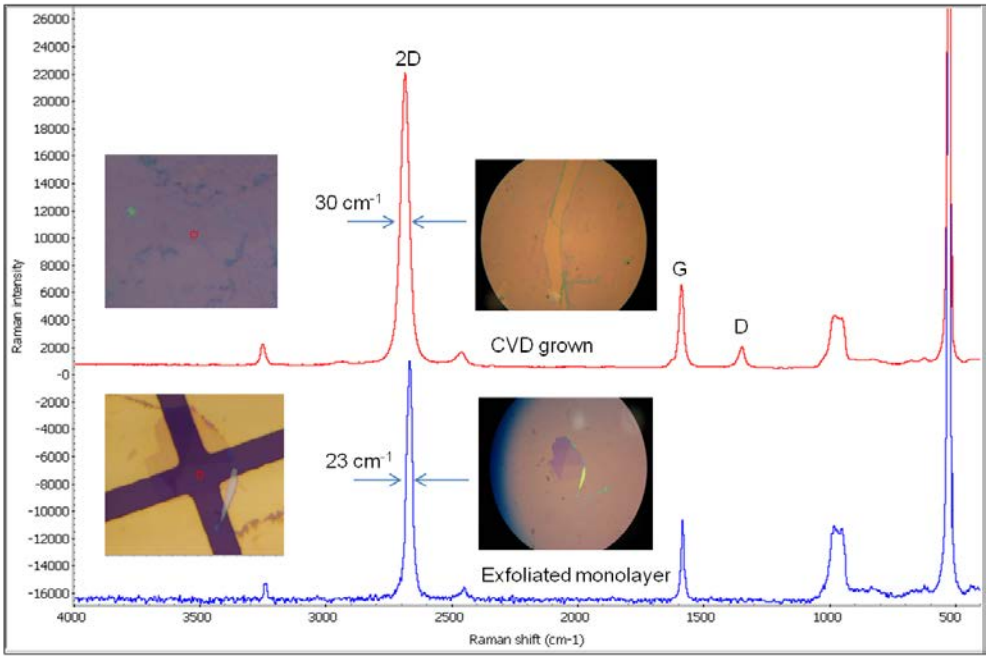

Figure 4.4. Raman spectra of CVD-grown and exfoliated MLG samples. All curves arenormalized to have the same G peak intensity. Insets show optical images of monolayer graphene of CVD grown and exfoliated, respectively.

I-V (current-voltage) characteristics and I-t (current-time) with fixed voltage of the sample without and with light exposure are measured using a Keithley 485 Auto ranging

Picoameter and Keithley 487 Picoameter/Voltage Source programmed with Labview for data acquisition. See the system in Figure 4.5.

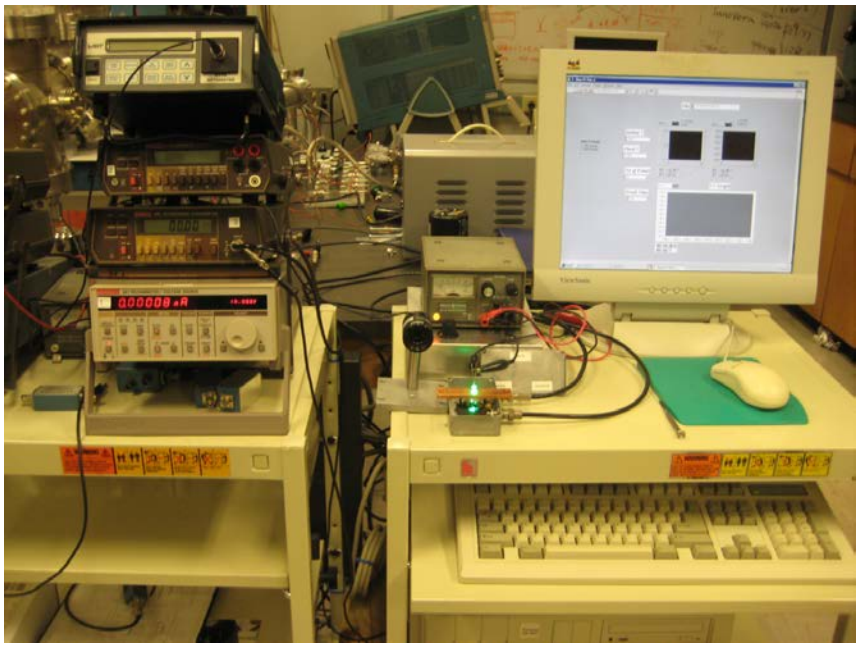

Figure 4.5. Computer-lab view controlled System of I-V measurement with light exposure setup and UDT S37 optometer for light calibration.

Transmission electron microscopy (TEM) images of CVD grown graphene are also taken for detailed structures. (See Figure 4.6 (a) and (b)). A close view of a sample holder with four gold-coated copper probes for contacting the electrodes is shown in Figure 4.6 (c). Micro-Raman spectroscopy at different steps of the process is carried out to examine the quality of the graphene from which the sample device is made and used for this study. The 17 cm^{-1} full-width-at-half-maximum (FWHM) of the 2D Raman peak at about 2700 cm^{-1} (see Figure 4.6 (d)) demonstrates that the grown sample is monolayer graphene [26,27]. Figure 4.6 (e) shows the I-V characteristics of the graphene sample and

demonstrates that the device has a good Ohmic contact. The sample size is 3 mm × 4 mm.

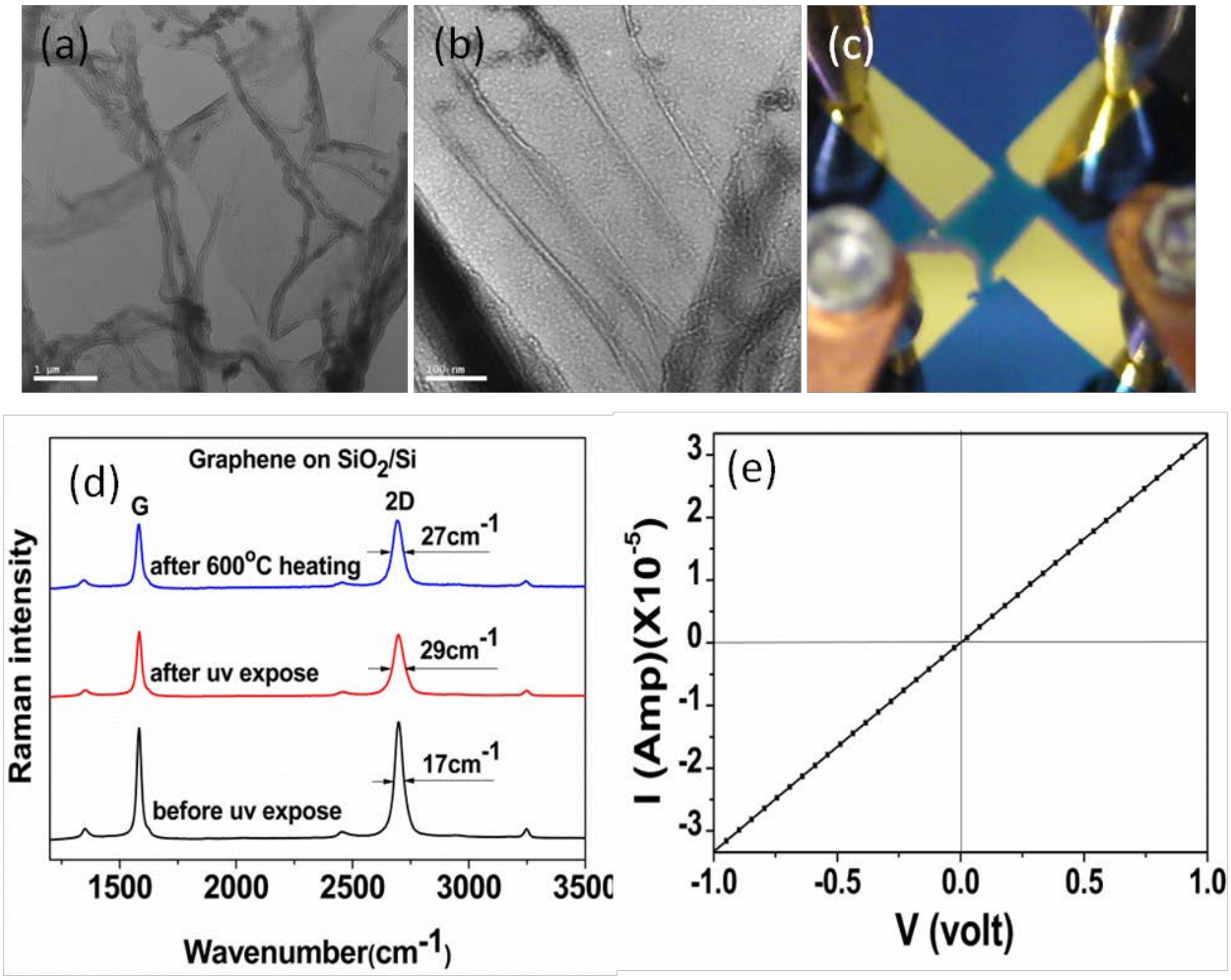

Figure 4.6. (a) and (b) TEM images of a typical CVD graphene sample at magnifications of 3,000 and 28,000 with scale bars of 1μm and 100 nm, respectively; (c) Photograph of our device; (d) micro Raman spectra of the graphene sample. Black: before 254 nm UV light exposure, Red: after 10 minutes of exposure to 254 nm UV light, Blue: after subsequent heating at 600°C for 10 minutes, respectively. (e) I-V characteristics of the graphene sample measured in air at room temperature.

We used the above device to investigate the resistance of the graphene sample as a function of time under exposure to light of different wavelengths. In the measurements, the output voltage between the two electrodes is fixed at 1V, while the current is recorded every 2 seconds when the sample is exposed to light at a particular wavelength. The light sources are LEDs of different peak wavelengths (630-380 nm) or a Xenon gas lamp (365 and 254 nm with filters) at a distance of 2 cm from the sample. The exposures are made in the following order: red (630 nm), orange (605 nm), yellow (595 nm), green (525 nm), aqua (507 nm), blue (472 nm), pink (440 nm), violet (420 nm) and UV (400 nm, 380 nm, 365 nm, and 254 nm). The intensity of the light at each wavelength is carefully calibrated and monitored by an optometer to ensure that light at each wavelength has the same incident intensity of 2 mW/cm^2. We observe that smaller wavelength light produces an increase in the saturation value of the sample's resistance, as shown in Figure 4.7 and Figure 4.8.

Experiments were carried out in which the wavelength of the incident light was changed from longer to shorter. The total exposure time at each wavelength was 10 minutes. Figure 4.7 shows a basic characteristic of the phenomenon. In the visible light range, incident light only slightly increased the resistance of the sample. When the incident light was in the UV range (starting from about 400 nm), the saturation resistance of the sample jumped to a higher value. The shorter the wavelength of the incident light, the higher the saturation resistance. The largest saturation resistance observed is about 2.5 times the value before light exposure. The small drop of resistance at the time of each light source (LED) switching (switched every 10 minutes) is due to the fact that the I-V measurement is continuous, during the time period of replacing the LED light source

(usually 20-30 seconds), and the resistance of the sample decays slightly although the drop does not significantly affect the saturation value of resistance resulting from the subsequent exposure.

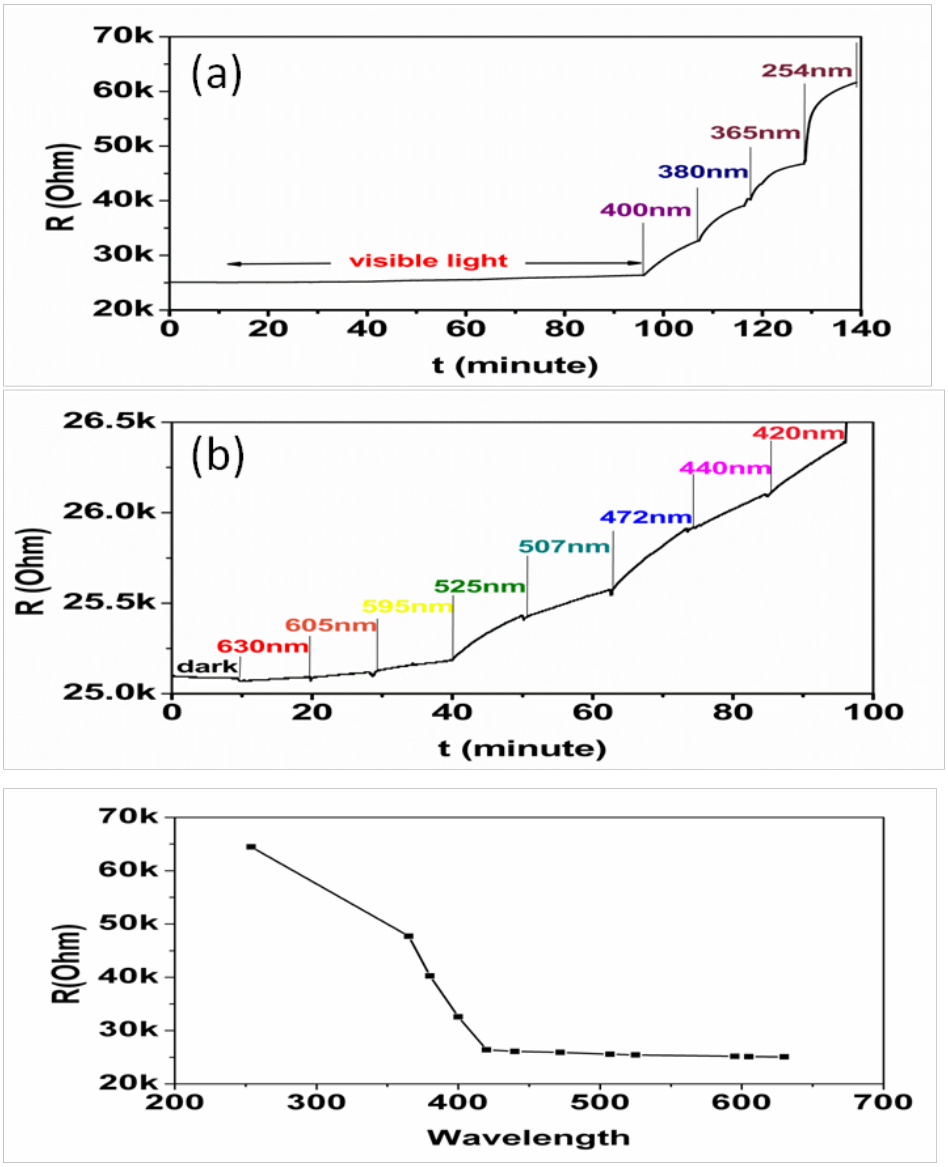

Figure 4.7. Resistance vs. expose light wavelength. Exposure time for each wavelength is 10 minutes. (a) Resistance vs. expose light wavelength in range of 630nm to UV light of 254 nm ; (b) a scale enlargement graph for the range of visible light in (a); (c) saturation values of resistance vs. light wavelength.

The time-resistance curve of the sample shown in Figure 4.8 (a) shows a typical exponential increase with a time constant of several minutes (for instance, 1.6 minutes for UV 254 nm). When the incident light is turned off, the resistance of the sample decays exponentially with a much larger time constant of tens of hours (for example, 21 hours after 254 nm UV irradiation), as shown in Figure 4.8 (b). Fluctuations in Figure 4.8 (b) are attributed to uncontrollable humidity changes in the environment during the long time decay [15]. The above observations are repeatable.

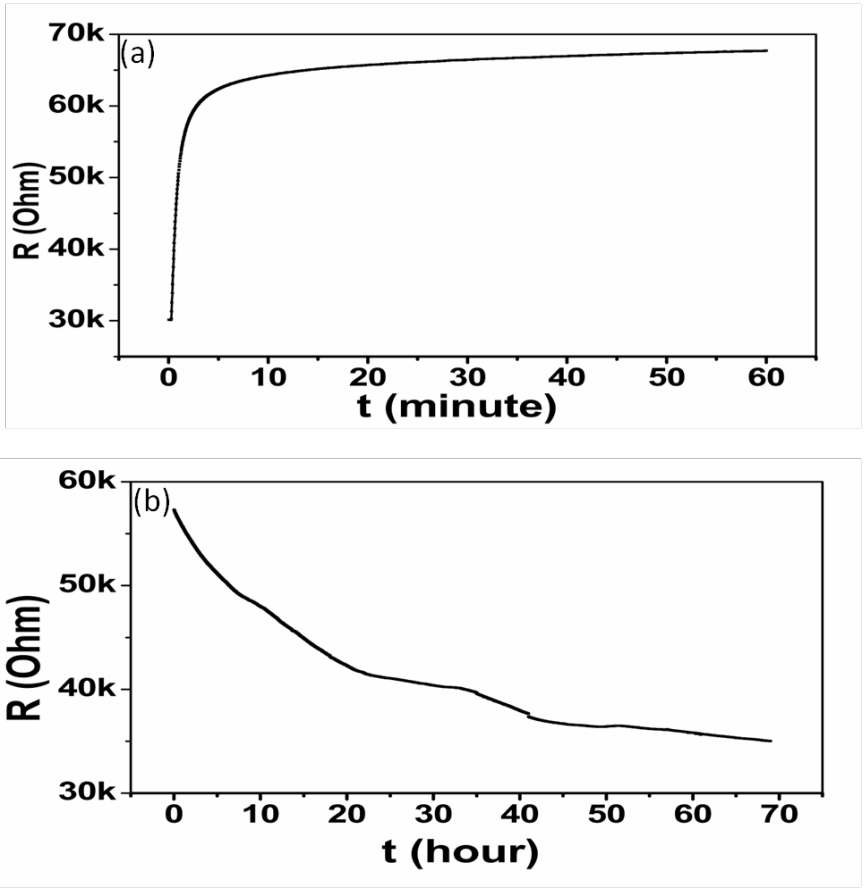

Figure 4.8. (a) Resistance vs. time measured under exposure to 254 nm UV; (b) time-decay process of resistance after turning off the light (254 nm UV).

Fitting with 1-term and 2-term exponential functions were carried out for curves

shown in Figure 4.8. As shown in Figures 4.9-4.12, and in order to compare the time constants for the change in resistance induced by light, we fitted the curves in Figure 4.7 (a), (b) with 1-term and 2-term exponential functions. The results are shown in Table 2.

Table 2 Time constants for resistance change under different wavelengths of light in Figure 4.7.

Light Wavelength (nm)	Time constant τ_1 (minute)	Time constant τ_2 (minute)	Adj. R-square (2-term)	Time constant τ (minute)	Adj. R-square * (1-term)	Resistance after light exposure R_e (Ω)	R_e/R_i (R_i=25068 Ω, R_i,original resistance)
630	49.97	49.95	0.8868	49.95	0.8877	25068	1.000
595	14.19	14.19	0.9765	14.19	0.9767	25182	1.005
525	12.44	12.44	0.9988	12.43	0.9988	25432	1.015
507	298.24	298.24	0.9965	286.42	0.9966	25549	1.019
472	24.62	24.62	0.9990	286.24	0.9990	25906	1.033
440	54.64	54.64	0.9979	51.85	0.9980	26102	1.041
420	61.51	0.69	0.9991	40.20	0.9990	26392	1.053
400	12.29	12.29	0.9999	12.29	0.9999	32372	1.291
380	5.17	5.17	0.9993	5.17	0.9993	40371	1.610
365	4.19	4.19	0.9978	4.19	0.9979	46728	1.864
254	0.55	5.94	0.9998	2.06	0.9704	61614	2.458

τ_1 and τ_2 are the time constants when fitting with $R = A_1 e^{-t/\tau_1} + A_1 e^{-t/\tau_2} + R_0$, and τ is the time constants when fitting with $R = Ae^{-t/\tau} + R_0$. It is found, from 254 nm to 472 nm, that the shorter the wavelength, the shorter the time constant. R-square is equal to 1 for perfect fitting. Light wavelength, photon energy and photon flux are also given in Table 3 for reference.

Table 3. Light wavelength, photon energy and photon flux.

Wavelength (nm)	630	605	595	525	507	472	440	420	400	380	365	254
Photon energy (eV)	1.97	2.06	2.08	2.36	2.45	2.63	2.82	2.95	3.10	3.26	3.40	4.88
Photon flux at 2 mW/cm^2 (x10^{15}/cm^2·s)	6.34	6.07	5.99	5.29	5.10	4.74	4.43	4.23	4.03	3.83	3.68	2.56

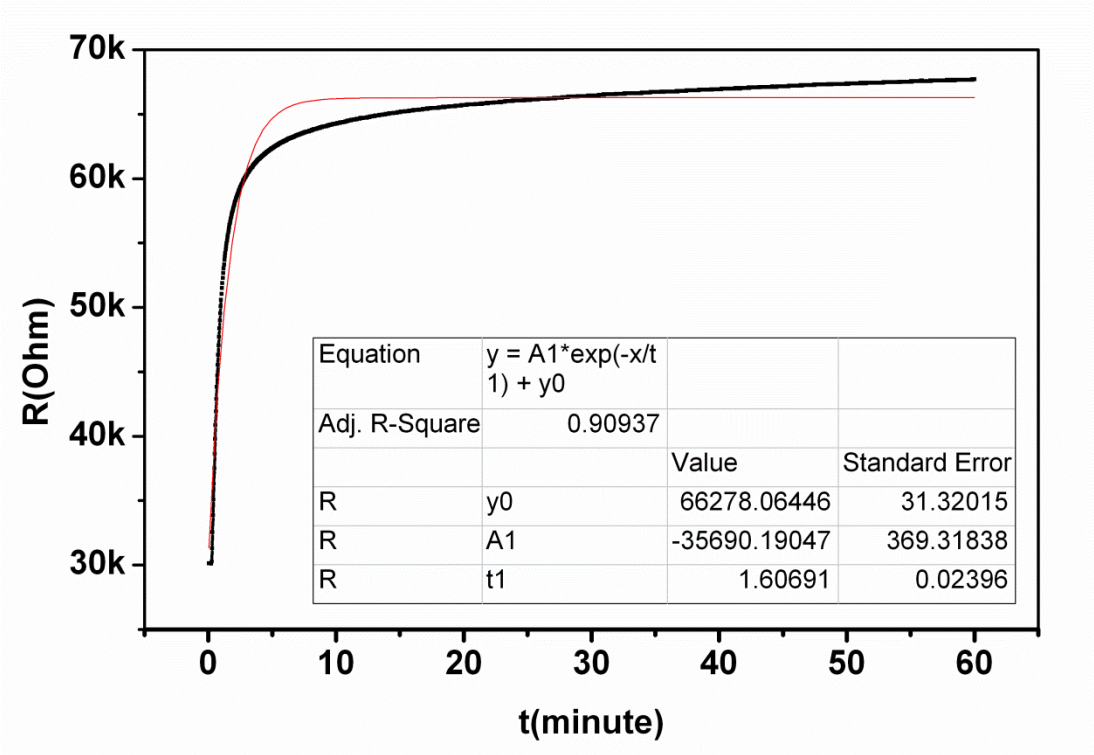

Figure 4.9. Fitting for Figure 4.8 (a) with 1-term exponential function.

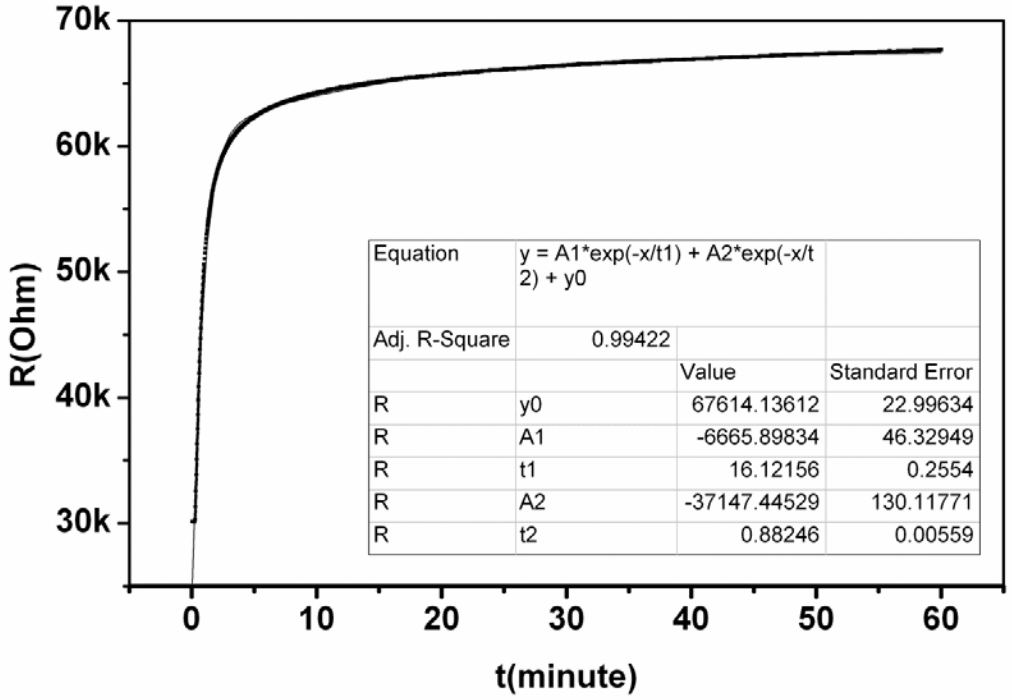

Figure 4.10. Fitting for Figure 4.8 (a) with 2-term exponential function.

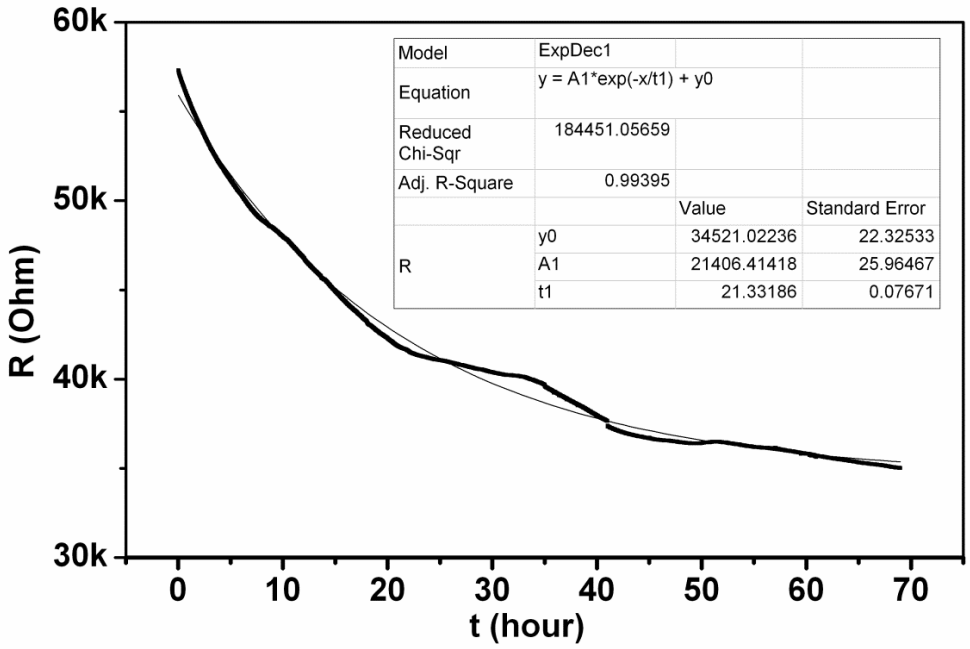

Figure 4.11. Fitting for Figure 4.8 (b) with 1-term exponential function.

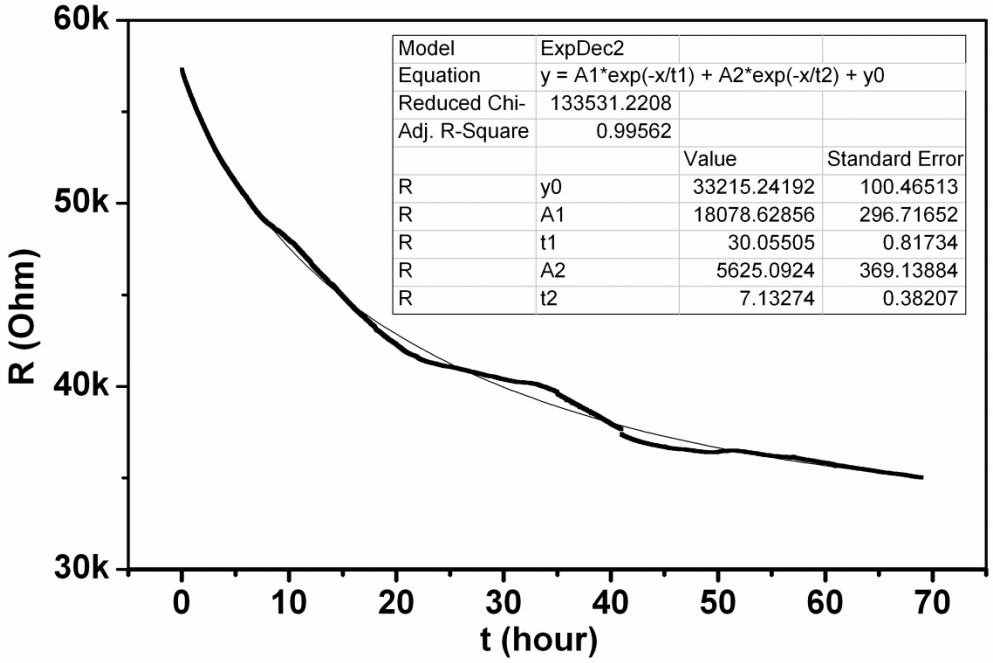

Figure 4.12. Fitting for Figure 4.8 (b) with 2-term exponential function.

The goodness of fit is usually measured by R-Square and Adjusted R-Square (Adj.R-Square). R-square shows the linear relationship between the independent variables and the dependent variable, which is, by definition, the sum of squared errors divided by the total sum of squares. R-Square can be any value from 0 to 1, and R-Square of 1 means perfect fitting. R-Square will continually rise irrespective of how valuable the variables are added. This means to increase number of variables (more terms in functions) will increase R-Square although the fit may not improve in a practical sense. To avoid this situation, the Adj.R-Square is used to indicate a better fit. The Adj.R-Square is defined based on the residual degree of freedom, and can take any value less than or equal to 1, with a value closer to 1 (when using only one variable in model) indicating a

better fit. R-Square is generally the best indicator of the fit quality when compare two models. It is said that R square increases with the addition of a new term in a model but adjusted R square increases, when the added terms improve the model. As shown in Table 2 and Figures 4.9-4.12, the fitting for the R-t curve under 254 nm exposures makes the biggest difference in Adj.R-Square with 1-term and 2-term exponential functions, the R-t curve after 254 nm exposure makes the second biggest difference in Adj.R-Square, all others make very small difference in Adj.R-Square. The 2-term exponential function required for better fitting may imply that there are two different processes occurring in the change to the resistivity of CVD-grown graphene. The two processes have different time constant.

The increase of resistance vs. time is also observed when the sample is placed in vacuum (1×10^{-5} Torr) and exposed to 254 nm UV light. This implies that the density of water molecules in air is not a significant parameter in the observed phenomenon. Micro-Raman spectroscopy was carried out after the sample was irradiated by 254 nm UV light. No significant enhancement of the D peak in the Raman spectrum was observed. This excludes the possibility of hydrogenation of the graphene sample induced by light exposure (appearance of the D peak is an indicator of hydrogenation of graphene [18]). Furthermore, we did not observe G peak shift as mentioned in the case of graphene defect oxidation

We heated the sample at 600 ºC in vacuum (1×10^{-7} Torr) and kept it at that temperature for 10 minutes to remove residual water molecules from the sample. After cooling the sample down to room temperature, Micro-Raman spectra was also examined (Figure 4.6 (e) blue) and showed that heating did not alter the structure of the sample.

We then repeated the electrical measurement under irradiation of 254 nm UV. No increase of resistance vs. time was observed.

As a reference, the same procedures are carried out on graphene/SiO_2 that is acquired by mechanical exfoliation of HOPG graphite. We did not observe the resistance change with light exposure.

4.3 Theoretical Simulation and Analysis

We notice the following from above experimental observations: First, environmental gases do not influence the light induced resistance jump. Thus, we can neglect the adsorbed molecules on graphene top surface. Second, this effect does not happen to the exfoliated graphene samples on SiO_2 surface. This tells us that the effect is correlated to defects in graphene. Third, heating in high vacuum can effectively eliminate the effect. This implies that there must be an impurity between graphene and substrate, and that impurity dominates the process and can be removed by heating.

There are two significant differences between a CVD-grown graphene transferred from pure water to a SiO_2 surface and an exfoliated graphene transferred to a SiO_2 surface: The CVD- grown graphene sample is full of defects compared to exfoliated graphene sample, and there are interfacial residual H_2O molecules for a CVD-grown sample that are introduced into the graphene/SiO_2 interface during the transfer process.

According to the above analysis, a super-cell model approach was constructed to simulate the CVD-grown graphene sample on SiO_2 surface. We use silicon dioxide (β-cristobalite) as the substrate which contains 16 silicon atoms and 32 oxygen atoms. The top layer of the substrate consists of O atoms; the Si atoms on the bottom layer are

saturated by H atoms to ensure the atomic configuration of the substrate in a chemical stable ground state. As shown in Figure 4.6 (a) and (b), the graphene sample used in the experiment has a relatively large size (in mm scale). This CVD-grown sample consists of various homogeneous graphene grains at several tens of nanometer scale that are usually overlapped to form a large sample with numerous grain boundaries and different kinds of defects. Considering our CVD-grown graphene sample is grown in a hydrogen environment, we assume that all carbon dangling bonds on defect sites are saturated by hydrogen atoms to reduce the associated total energy of the whole system. We model the defected graphene sample as a perfect graphene overlapped on top of a graphene strip. A water molecule near by the graphene strip is interfacially placed between the perfect graphene plane and the SiO_2 substrate, and naturally relaxed to the lowest energy state from a random initial position and orientation. We utilize the Vienna A b-initio Simulation Package (VASP) with the projector augmented wave (PAW) method to perform our first-principle calculations that is based on density functional theory. The relativistic effect is included in calculations, and the exchange-correlation interaction potentials of a multi-electron system in a local density approximation (LDA) [28, 29, 30] is employed. Recent analysis shows that LDA with PAW potentials provide quite reliable predictions for adsorption energy calculations [31-37].

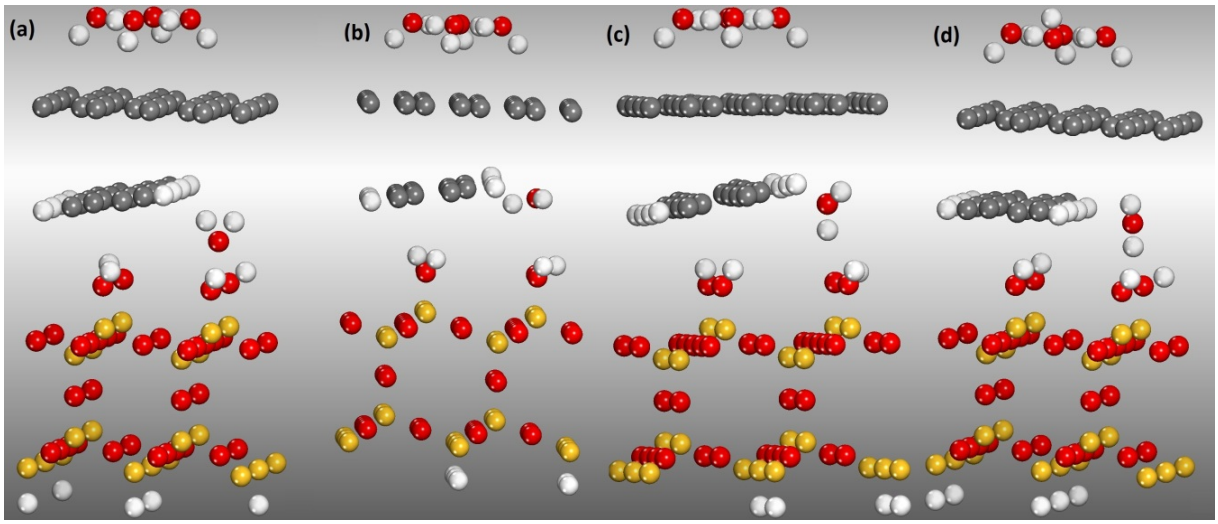

Figure 4.13. Periodic stable atomic configurations in the DFT calculations. (a) 16 silicon atoms (yellow), 32 oxygen atoms (red), 48 carbon atoms (black), 16 hydrogen atoms (white) bonding with Si and C atoms, 4 H_2O on top, and one H_2O between graphene and SiO_2 substrate in a ground state; (b) The system with the H_2O between graphene at another close ground state when the H_2O was moved slightly from the position in (a); (c) The system with the H_2O between graphene at another close ground state when the H_2O was moved slightly from the position in (b); (d) The system with the H_2O between graphene at another close ground state when the H_2O was moved slightly from the position in (c).

The result of relaxation shows that there are four ground states for the model with respect to four orientations of the H_2O molecule. The graphene defect structure ensures that the H_2O molecule and its split products, $H^{+\delta}$ and $OH^{-\delta}$, are all enclosed to mimic the experimental conditions. Two kinds of environments are considered: (1) the top surface of the graphene is clean, and (2) there are polar molecules, such as H_2O molecules,

physi-adsorbed on top of the graphene, to examine the effect of circumference molecules on the photo-electrical property of the graphene. The results show that molecules physi-adsorbed on top of the graphene do not significantly affect the behavior of the interfacial H_2O molecule. The atomic configurations of the samples in the first-principles calculation are shown in Figure 4.13 and Figure 4.14.

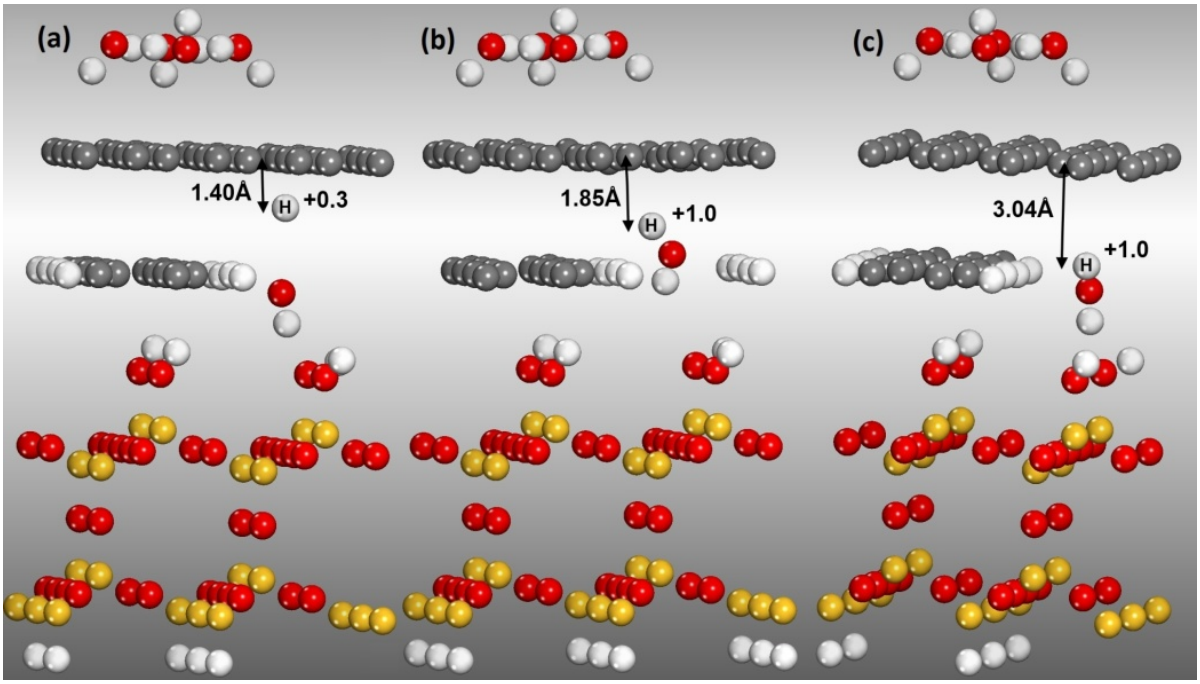

Figure 4.14. (a) The atomic configurations of the excited state; (b) Intermediate meta-stable states; and (c) Stable states.

The super cell is periodically extended along the surface of the substrate. Figures 4.13 (a) ~ 4(d) demonstrate four cases of the model at ground state. The differences among the four cases are orientations of the H_2O molecule relative to the graphene and SiO_2 substrate with negligible total energy fluctuation. In all cases, all the dangling bonds of the C atoms at the defect are completely saturated by H atoms. In Figure 4.14 (a), the

interfacialH_2O molecule is partially disassociated with the $OH^{-\delta}$ group spontaneously adsorbed on the substrate surface and the $H^{+\delta}$ adsorbed onto the graphene. The calculated disassociation energy from the ground state Figure in Figure 4.14 (c) to the state in Figure 4.14 (a) is 4.6eV. In Figure 4.14 (b) and (c), we find other two meta-stable disassociation states at 2.5 eV and 3.3 eV relative to the ground state, respectively. With respect to different meta-stable disassociation states, both δ value and length of C-$H^{+\delta}$ bond are different, showing that there are different electric effects of $H^{+\delta}$ on the graphene. In addition to the mentioned three meta-stable states, we also find that there are many small sub-stable states between the highest 4.6 eV and the ground state that are not displayed in Figure 4.14.

4.4 Discussion

Based on the above calculations, because of the existence of the defect field of the graphene, incident light can disassociate a H_2O molecule to a partially disassociated state. The higher the energy of the incident photon, the higher the disassociation state can be reached associating with strong electric effects on graphene: (1) producing a strong scattering center to carriers; and (2) resulting in local distortion of the graphene lattice. Both can result in an increase of scattering cross-section of carriers in graphene. While the light is off, due to the existence of a series of meta-stable disassociation states, the $H^{+\delta}$ will undergo many steps associating with a long decay time to recombine $OH^{-\delta}$ to a neutral H_2O molecule, which results in the graphene sample slowly return to its original value of conductivity. Once the light starts again, the same process is repeated. It is the interaction of graphene defects and the water molecules between graphene and substrate, which dominates the light induced change of graphene resistivity. For the case

without defects in graphene, such as an exfoliated sample, or the case without interfacial H_2O impurities, such as a heated CVD grown sample, there is no photo-electronic phenomenon. In our work, we also calculate a configuration in which the carbon atoms at the edge of the defect are not thoroughly saturated by H atoms. In this configuration, a H_2O molecule will be spontaneously partially disassociated into an $H^{+\delta}$ and an $OH^{-\delta}$ because of the very strong local defect field, which implies that the defect field of a carbon dangling bond could be utilized to split H_2O molecules. The work of our study opens a way to tune graphene resistivity by light.

4.5 Acknowledgements

The authors thank Mr. C.L. Chi for taking TEM images of the CVD graphene film, and Dr. T. Cai, J. D. Jones and J. Wahrmund for their useful discussions. The work was funded in part by the US Air Force Office of Scientific Research (Award No. FA9550-09-1-0367), the National Science Foundation (Award No. CBET-0754821), NSF LASIGMA Project (Award No. EPS-1003897, NSF92010-15-RII-SUBR), NASA/LEQSF (2009-2012)-Phase3-03, DOE (Award No.DE-FE0004734 and DE-FE0003693), and the LONI institute.

4.6 References

1. Novoselov, K. S., Geim, A. K., Morozov, S. V., Jiang, D., Zhang, Y., Dubonos, S. V., Grigorieva, I. V., Firsov, A. A.: Electric Field Effect in Atomically Thin Carbon Films. Science 306, 666(2004).

2. Novoselov, K. S., Geim, A. K., Morozov, S. V., Jiang, D., Katsnelson, M. L., Grigorieva, I. V., Dubonos, S.V. & Firsov, A.A.: Two-dimensional gas of massless Dirac fermions in graphene. Nature 438, 197(2005).
3. Novoselov, K. S., Jiang, D., Schedin, F., Booth, T. J., Khotkevich, V. V., Morozov, S. V., and Geim, A. K.: Two-dimensional atomic crystals. Proc. Natl. Acad. Sci. U. S. A. 102, 10451(2005).
4. Morozov, S. V., Novoselov, K. S., Katsnelson, M. I., Schedin,F., Elias, D. C., Jaszczak, J. A., and Geim, A. K.: Giant Intrinsic Carrier Mobilities in Graphene and Its Bilayer. Phys. Rev. Lett. 100, 016602(2008).
5. Schedin, F., Geim, A. K., Morozov, S. V., Hill, E. W., Blake, P., Katsnelson, M. I., and Novoselov, K. S.: Detection of individual gas molecules adsorbed on graphene. Nature Mater. 6, 652(2007).
6. Wehling, T. O., Novoselov, K. S., Morozov, S. V., Vdovin, E. E., Katsnelson, M. I., Geim A. K., and Lichtenstein, A. I.: Molecular Doping of Graphene. Nano Lett. 8, 173(2008).
7. Ang, P. K., Chen, W., Wee, A. T. S., and Loh, K. P..: Solution-Gated Epitaxial Graphene as pH Sensor. J. Am. Chem. Soc. 130, 14392(2008).
8. Romero, H. E., Josh ,P. i., Gupta, A. K., Gutierrez, H. R., Cole, M. W., Tadigadapa, S. A., and Eklund, P. C..: Adsorption of ammonia on graphene. Nanotechnology 20, 245501(2009).
9. Lu, G., Ocola, L. E., and Chen, J.: Reduced graphene oxide for room-temperature gas sensors. Nanotechnology 20, 445502(2009).
10. Leenaerts, O., Partoens, B., and Peeters, F. M.: Adsorption of H2O, NH3, CO, NO2, and NO on graphene: A first-principles study. Phys. Rev. B 77, 125416(2008).

11. Ko, G., Kim, H. Y., Ahn, J., Park, Y. M., Lee, K. Y., and Kim, J.: Graphene-based nitrogen dioxide gas sensors. Current Appl. Phys. 10, 1002(2010).
12. Saffarzadeh, A.: Modeling of gas adsorption on graphene nanoribbons. J. of Appl. Phys. 107, 114309(2010).
13. Leenaerts, O., Partoens, B., and Peeters, F. M.: Water on graphene: Hydrophobicity and dipole moment using density functional theory. Phys. Rev. B 79, 235440(2009).
14. Yavari, F., Kritzinger, C., Gaire, C., Song, L., Gulapalli, H., Tasciuc, T. B., Ajayan, P. M., and Koratkar, N.: Tunable Bandgap in Graphene by the Controlled Adsorption of Water Molecules. Small 6, 2535(2010).
15. Wehling, T.O., Lichtenstein. A.I., and Katsnelson, M.I.: First-principles studies of water adsorption on graphene The role of the substrate. Appl. Phys. Lett. 93, 202110(2008).
16. Elias, D. C., Nair, R. R., Mohiudin, T. M. G., Morozov, S. V., Blake, P., Halsall, M. P., Ferrari, A.C , Boukhvalov, D.W., Katsnelson, M.I, Geim, A.K., Novoselov, K.S.: Control of Graphene's Properties by Reversible Hydrogenation Evidence for Graphane. Science 323, 610(2009).
17. Sofo, J.O., Chaudhari,A.S., and Barber,G. Graphane, D.:A two-dimensional hydrocarbon. Phys. Rev. B 75, 153401(2007).
18. Jones, J. D., Mahajan, K. K., Williams, W. H., Ecton, P. A., Mo Y., and Perez J. M.: Formation of graphane and partially hydrogenated graphene by electron irradiation of adsorbates on graphene. Carbon 48, 2335(2010).

19. Acik, M., Lee, G., Mattevi,C., Chhowalla, M., Cho, K., and Chabal, Y. J.: Unusual infrared-absorption mechanism in thermally reduced graphene oxide. Nature Mater. 9, 840(2010).
20. Mkhoyan, K. A., Stewart, D.A., Eda, G., Mattevi, C., Miller, S., and Chhowalla, M.: Atomic and Electronic Structure of Graphene-Oxide. Nano Lett. 9, 1058(2009).
21. Brar, V.W., Decker, R., Solowan, H-M, Wang, Y., Maserati, L., Chan, K.T., Lee, H., Girit, C.O., Zettl, A., Louie, S.G., Cohen, M.L. and Crommie, M.F.: Gate-controlled ionization and screening of cobalt adatoms on a graphene surface. Nature Physics, Vol 7 (2011) 34
22. Chan, K.T., Lee, H. and Cohen, M.L.: Gated adatoms on graphene studied with first-principles calculations. Phys. Rev. B 83 035405 (2011)
23. Chan, K.T., Lee, H. and Cohen, M.L.: Possibility of transforming the electronic structure of one species of graphene adatoms into that of another by application of gate voltage First-principles calculation. Phys. Rev. B 83 165419 (2011)
24. Lu, Y-H., Lei S., Zhang C. and Feng, Y-P.: Electric-field control of magnetic states, charge transfer, and patterning of adatoms on graphene First-principles density functional theory calculations. Physical Review B 80, 233410 (2009)
25. Chan, K.T., Lee,H., and Cohen,M.L., see the web posting at http://absimage.aps.org/image/MWS_MAR11-2010-006039.pdf 31
26. Ferrari, A. C., Meyer, J. C., Scardaci, V., Casiraghi, C., Lazzeri, M., Mauri, F., Piscanec S., Jiang, D., Novoselov, K. S., Roth, S., Geim, A. K.: Raman Spectrum of Graphene and Graphene Layers. Phys. Rev. Lett. *97*, 187401(2006).

27. Graf, D., Molitor, F., Ensslin, K., Stampfer, C., Jungen, A., Hierold, C., Wirtz, L.: Spatially Resolved Raman Spectroscopy of Single- and Few-Layer Graphene. Nano Lett. Vol. 7, No.2 238-242 (2007).
28. Blöchl, P.E.: Projector augmented-wave method. Phys. Rev. B 50, 17953(1994). 21
29. Kresse, G. and Jouber, D. t.: From ultrasoft pseudopotentials to the projector augmented-wave method. Phys. Rev. B 59, 1758(1999).
30. Alfè, D. and Gillan, M. J., J. Phys.: The energetics of oxide surfaces by quantum Monte Carlo. Cond. Matt. 18, L435 (2006).
31. Yang, S., Zhao, G.L., and Phillips, J. M..: The electronic structures of commensurate Ru(0001)-(3 × 3) -4Kr and Ru(0001)- (5 × 5)-Kr using density functional theory. Surf. Sci. 604, 1102 (2010).
32. Kresse, G. and Hafner, J.: Ab initio molecular dynamics for liquid metals. Phys. Rev. B 47, 558(1993).
33. Kresse, G. and Furthmüller, J.: Efficiency of ab-initio total energy calculations for metals and semiconductors using a plane-wave basis se. Comput. Mater. Sci. 6, 15(1996).
34. Kresse, G. and Furthmüller, J.: Efficient iterative schemes for ab initio total-energy calculations using a plane-wave basis set. Phys. Rev. B 54, 11169(1996).
35. VASP 2010 manual, see: http://cms.mpi.univie.ac.at/vasp/.
36. Sheppard, D., Terrell, R., and Henkelman, G.: Optimization methods for finding minimum energy paths. J. Chem. Phys. 128, 134106 (2008).
37. Jónsson, H., Mills, G., Jacobsen, K. W.: Nudged Elastic Band Method for Finding Minimum Energy Paths of Transitions, in Classical and Quantum Dynamics in

Condensed Phase Simulations. Ed. B. J. Berne, G. Ciccotti and D. F. Coker (World Scientific, 1998), page 385.